Doctoral Dissertation

Synthesis, Structural Characterization, and Thermal Transformation of Methylammonium Isopolyoxometalates, and their Application as Staining Reagent for SARS-CoV-2 Observation

(メチルアンモニウムイソポリオキソメタレートの合成、構造解析、加熱による構造変換、および SARS−CoV−2 観察のための染色試薬としての応用)

Ndaru Candra Sukmana

Department of Applied Chemistry,
Graduate School of Engineering, Hiroshima University
(広島大学大学院工学研究科 学応用化学専攻)

March 2023

Abstract of dissertation

Polyoxometalates are anionic polynuclear metal–oxo molecules of early transition metals, such as W, Mo, V, and Nb, formed between metal oxides (WO_3 or MoO_3) and monometalates ($[WO_4]^{2-}$ or $[MoO_4]^{2-}$). The primary goal of this dissertation was to synthesis of alkylammonium isopolyoxometalates and their crystal transformation by heat treatment. Methylammonium monomolybdate, methylammonium vanadate, and methylammonium paradodecatungstate were prepared by the reaction of methylamine solution with MoO_3, V_2O_5, and WO_3 or H_2WO_4, respectively.

Methylammonium monomolybdate, $(CH_3NH_3)_2MoO_4$ contained monomeric $[MoO_4]^{2-}$ and two methylammonium counter cations, which crystallized in the space group *Pnma*. Solid state heating of the $(CH_3NH_3)_2MoO_4$ in air released water and methylammonium to produce several methylammonium isopolymolybdates such as $(CH_3NH_3)_8[Mo_7O_{24}\text{-}MoO_4]$, $(CH_3NH_3)_6[Mo_7O_{24}]$, $(CH_3NH_3)_8[Mo_{10}O_{34}]$, and $(CH_3NH_3)_4[Mo_8O_{26}]$, and molybdenum oxides such as hexagonal MoO_3 and orthorhombic MoO_3 which were confirmed by single crystal XRD, powder XRD, IR, Raman, and elemental analysis.

The asymmetric unit of methylammonium vanadate, $(CH_3NH_3)[VO_3]$ contained four methylammonium cations and a “snake-like” $([VO_3]_4)^{4-}$ anion chain along the *c*-direction in the $Pna2_1$ space group. The solid-state thermal structure transformation of methylammonium vanadate, $(CH_3NH_3)[VO_3]$, from -150 °C to 350 °C is reported. A reversible structural transformation due to the change in the direction of the methylammonium cations in the crystal packing was observed between −150 and −100 °C, which is also confirmed by the reversible profiles observed in differential scanning calorimetry. The methylammonium vanadate is stable until at ca. 100 °C and further heating releases methylamine and water and V_2O_5 is formed at ca. 275 °C .

Methylammonium paradodecatungstate, $(CH_3NH_3)_{10}[H_2W_{12}O_{42}]\cdot nH_2O$, contained $[H_2W_{12}O_{42}]^{10-}$ anion, ten methylammonium cations, and lattice water. The $[H_2W_{12}O_{42}]^{10-}$ anion consists of two HW_3O_{13} groups containing three edge-

sharing WO_6 octahedra and two W_3O_{14} groups having two edge-sharing connections. Some lattice water was released by drying the produced material at 70 °C, but this did not affect the $[H_2W_{12}O_{42}]^{10-}$ structure, although there was a decrease in the unit cell volume. By adding water, the loss of lattice water and structural changes were reversed. CH_3NH_2 and H_2O were released by heating methylammonium paradodecatungstate at more than 150 °C, and the amorphous phase was observed as an intermediate product and monoclinic WO_3 as the final product.

Negative staining is a valuable technique for viewing the detailed morphology and size of the intact virus. The primary distinction between members of viral families is their morphology, so viral morphology is crucial to the study of virology. In this dissertation, we evaluate the performance of synthesized methylammonium molybdate, tungstate, and vanadate as staining reagents for transmission electron microscopy observation of SARS-CoV-2. The results show that methylammonium polyoxometalates are a potential negative staining agent for observing the spike protein of coronaviruses. Based on the contrast and sharpness of the stained particles, methylammonium heptamolybdate was found to be an excellent staining agent for observing the SARS-CoV-2 delta variant.

CONTENTS

CHAPTER 1
INTRODUCTION

1.1 Polyoxometalates

Polyoxometalates (POMs) are negatively charged polyoxoanions that contain highly symmetrical core assemblies of the metal center surrounded by oxygen atoms. Self-assembly processes form these metal oxide clusters from the highest oxidation state of early transition metals such as vanadium (V), niobium (Nb), tungsten (W), and molybdenum (Mo) with oxo ligands (O^{2-}).[1–3] Polyoxometalates can be thought of as packed arrays of MO_6 octahedral units (Figure 1.1). Numerous shapes can be formed by assembling MoO_6 units. Various compositions and structural variations of polyoxometalates result in a wide variety of physical and chemical characteristics, including negative charges, oxo-enriched surfaces, acid-base properties, and redox potential.[3–5]

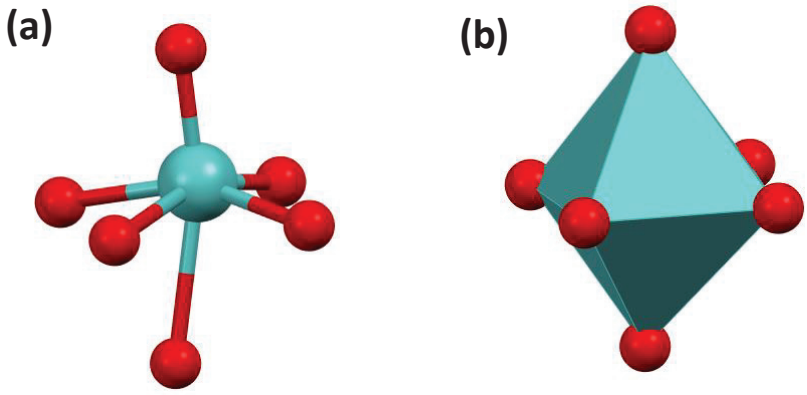

Figure 1.1. (a) Ball-and-stick and (b) polyhedral representation of fundamental MoO_6 unit. Light blue and red represent molybdenum and oxygen, respectively.

Berzelius described the first class of POMs in 1826, he described $[PMo_{12}O_{40}]^{3-}$, the yellow precipitate that is formed when excess ammonium molybdate is added to phosphoric acid.[5] Marignac first discovered and classified heteropolytungstates, two isomeric forms of $[SiW_{12}O_{40}]^{4-}$ in 1862. Subsequently, Keggin determined the structure of the related anion $[PW_{12}O_{40}]^{3-}$ by crystallographic characterization in the early 1930s. Following the development of advanced instrumentation especially

spectroscopic techniques accelerated characterization of polyoxometalates, polyoxometalates researches began to increase and hundreds of various polyoxometalate compounds were reported. Evans reported the structure of $[TeMo_6O_{24}]^{6-}$ in 1948, followed by Anderson who found $[Mo_7O_{24}]^{6-}$ structure. In 1953, Dawson and Lindqvist reported the structure of $[P_2W_{18}O_{62}]^{6-}$ and $[Nb_6O_{19}]^{8-}$, respectively. Dexter and Silverton reported lanthanide containing polyoxometalate, $[CeMo_{12}O_{42}]^{8-}$ in 1968. In 1985, Pope revised the proposed structure of the Preyssler-type phosphotungstate, which is $[P_5W_{30}O_{110}Na(H_2O)]^{14-}$. Keplarate-type molybdate, $[Mo_{132}O_{372}(CH_3COO)_{30}(H_2O)_{72}]^{42-}$ was reported by Muller in 1998.[1,3,6]

The formation of polyoxometalates in solution are affected by a wide range of synthetic condition such as compositions, concentrations, pH, solvents, and oxidation states. The primary parameters affecting the formation of polyoxometalates speciation are the acid (pH) and metal concentrations, ionic strength, buffer type, presence of possible heteroatoms, and counter cation type.[4] The possibility to modify the properties including molecular composition, size, shape, charge density, redox potentials, acidity, and solubility makes polyoxometalates widely used in many fields including medicine,[7] catalysis,[8,9] sensor,[2] and staining reagent.[10,11]

Polyoxometalates are categorized into two groups: isopolyanion and heteropolyanion. Isopolyanions are comprised of only one early transition metal without other cationic species except proton in the molecule.[12] Heteropolyanions are metal oxides that contain more than two cationic elements, early transition metals and other main elements such as Si^{4+}, P^{5+}, and S^{6+}. Heteropolyanions have general formula $[X_xM_mO_y]^{n-}$, where M is a large fraction of transition metal. X is a smaller fraction of other types of atoms such as p or d block elements and often X is called as heteroatom.[2,12]

Polyoxometalates are formed between the mononuclear metalates and the oxide. The formation of polyoxometalates is strongly influenced by the type/concentration of metal oxide, pH, ionic strength, type/concentration of heteroatom, reducing agents, ligands, and experiment conditions such as

temperature. In this thesis, we focused on the formation of isopolyoxoanions especially isopolymolybdate, isopolyvanadate, and isopolytungstate with a counter cation methylammonium ($CH_3NH_3^+$).

1.1.1 Isopolyoxomolybdates

Various polyoxomolybdates have been isolated from aqueous or non-aqueous solutions. $[MoO_4]^{2-}$ is the predominant species in strongly basic molybdate solutions, while in strongly acidic molybdate solutions, the predominant species are $[MoO_2(OH)(H_2O)_3]^+$ or $[Mo_2O_5(OH)(H_2O)_5]^+$.[13] Heptamolybdate, $[Mo_7O_{24}]^{6-}$ is the first major product during the acidification of aqueous $[MoO_4]^{2-}$.[14,15] $[Mo_7O_{24}]^{6-}$ can be protonated by further acidification to form β-$[Mo_8O_{26}]^{4-}$.[15] $[Mo_{36}O_{112}(OH_2)_{16}]^{8-}$ can be formed at a pH lower than 2.8, which is a dimer of $[Mo_{18}O_{56}(H_2O)_8]^{4-}$ with an inversion center (Figure 1.2).[14] Common molybdate species formed in solution and solid state. Low nuclear polyoxomolybdates are unstable in solution and formed infinite two-dimensional chains in hydrothermal and solid-state reactions.[15]

Solid-state heating of $(NH_4)_2[MoO_4]$ is known to produce ammonium isopolymolybdates, such as $(NH_4)_2[Mo_2O_7]$, $(NH_4)_2[Mo_3O_{10}]$, and $(NH_4)_2[Mo_4O_{13}]$ and further heating produces hexagonal-MoO_3 and orthorhombic-MoO_3.[16] The formation of several isopolymolybdates during heat treatment might be caused by condensation reaction as the effect of releasing NH_3 and H_2O (Figure 1.3) which has a similar effect to acidification.

1.1.2 Isopolyoxovanadates

Numerous discrete isopolyoxovanadates have been reported in the solid state from aqueous and non-aqueous solutions, such as $[V_3O_9]^{3-}$, $[HV_4O_{12}]^{3-}$, $[V_5O_{14}]^{3-}$, $[V_{10}O_{28}]^{6-}$, $[V_{12}O_{32}]^{4-}$, $[V_{13}O_{34}]^{3-}$, and $[V_{15}O_{42}]^{9-}$. The formation of isopolyoxovanadates are influenced by concentration, pH, ionic strength, and reaction temperature. One to five V atom oligomers are formed in an aqueous vanadium solution of pH > 6.[15] The numerous structural suggestions of trivanadate and tetravanadate including linear and cyclic forms have been reported.[15] $[V_3O_{10}]^{5-}$ and $[V_4O_{13}]^{6-}$ with linear form were observed in an aqueous solution at

pH <10.[17] Meanwhile, a cyclic form was obtained from non-aqueous media such as $[V_3O_9]^{3-}$, $[HV_4O_{12}]^{3-}$, and $[V_5O_{14}]^{3-}$.[17–19] Since the polymerization of the anion to infinite chains $([VO_4]^{3-})_n$ always occurs simultaneously, attempts to isolate the discrete linear trivanadate and tetravanadate from the aqueous solution have been unsuccessful. Decavanadate, $[V_{10}O_{28}]^{6-}$ is stable at pH 7. Transformation into smaller polyoxovandates like $[VO_4]^{3-}$, $[V_2O_7]^{4-}$, and $[V_4O_{12}]^{4-}$ were occurred when the pH was higher than 7, while in the basic condition, decavanadate will be transformed to $H_x[VO_4]^{(3-x)-}$ (Figure 1.4).[15]

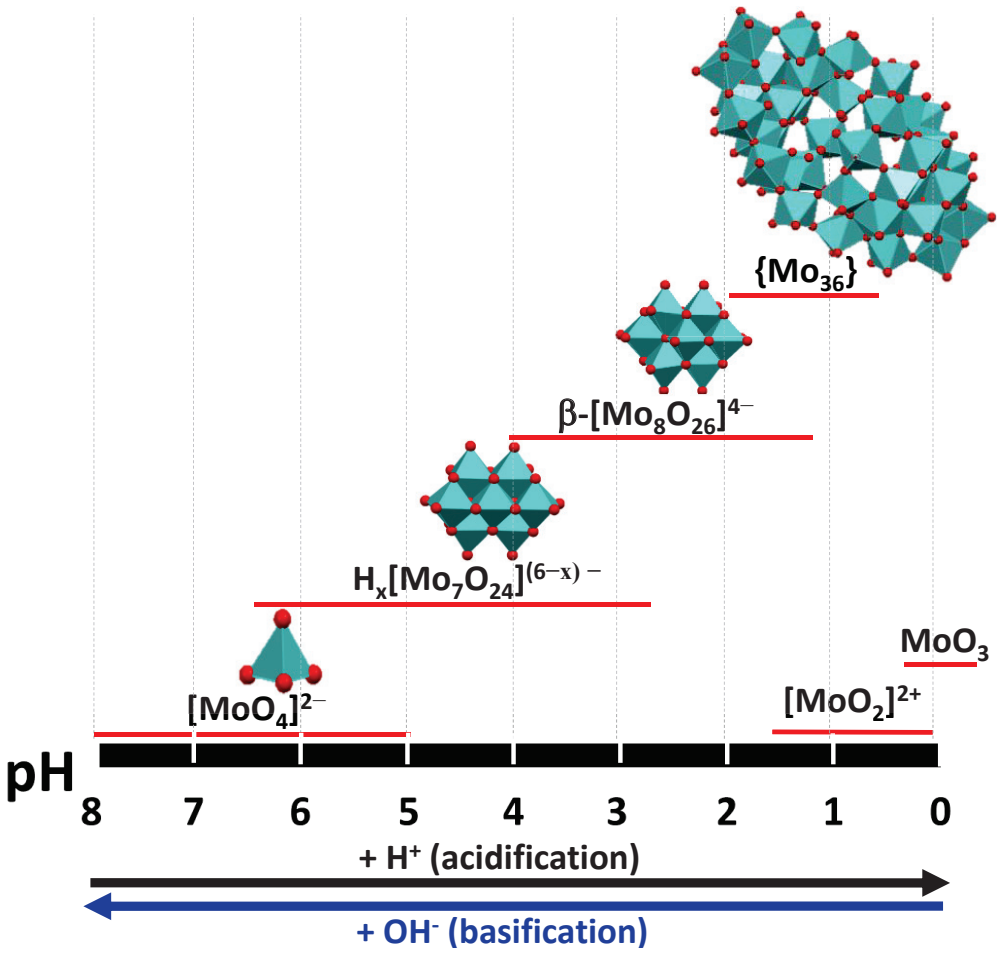

Figure 1.2. Speciation of isopolyoxomolybdates in aqueous solution.

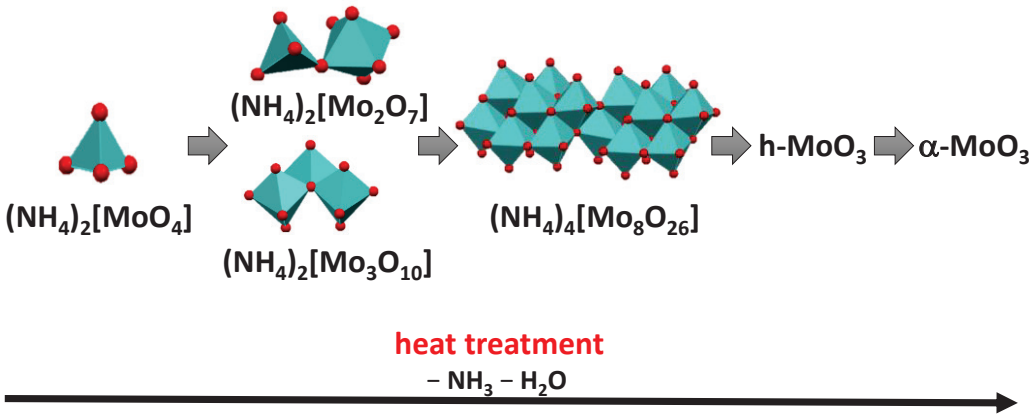

Figure 1.3. Solid-state thermal transformation of ammonium monomolybdate.

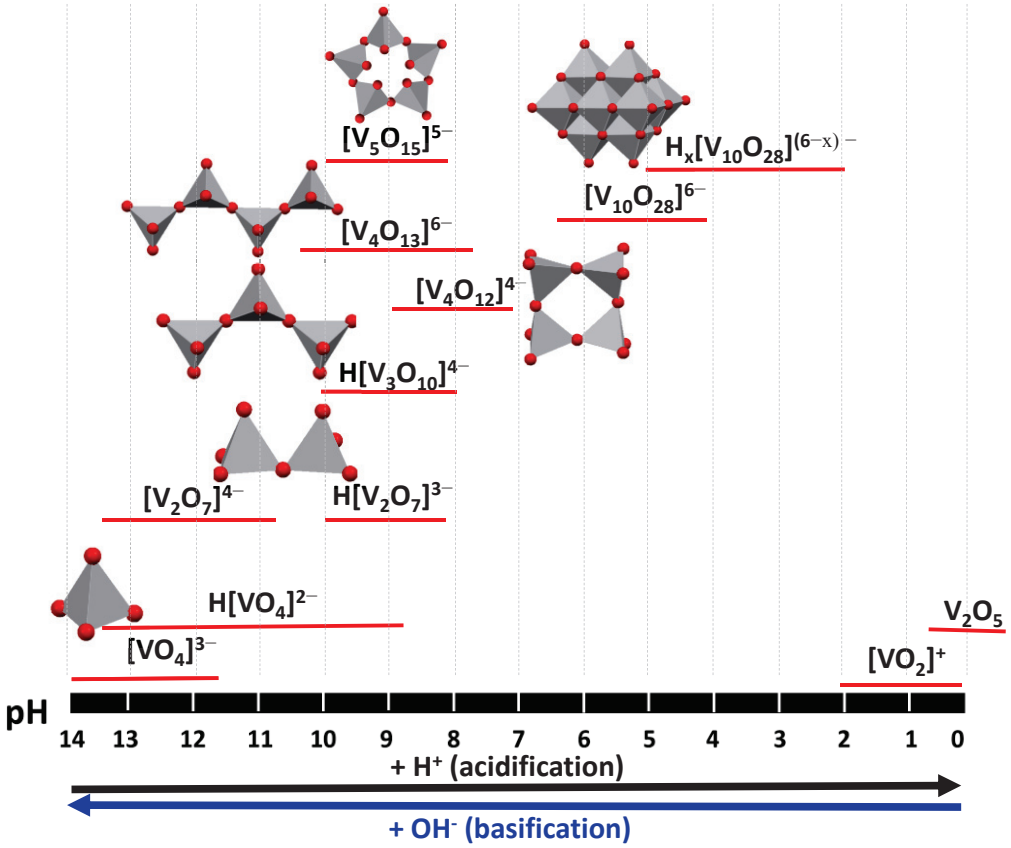

Figure 1.4. Speciation of isopolyoxovanadates in aqueous solution.[15]

Heat treatment of ammonium vanadate produces a similar effect to acidification. NH_3 and H_2O were released from the compound during solid-state heating which might cause dehydrative condensation. It has been reported that

solid-state heating of $(NH_4)[VO_3]$ produced $(NH_4)_2[V_6O_{16}]$ as an intermediate product and further heating produced V_2O_5 (Figure 1.5).[20]

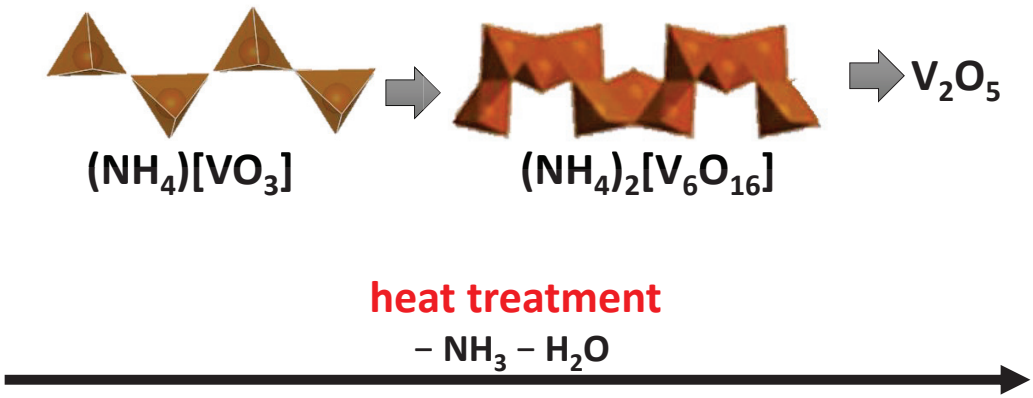

Figure 1.5. Solid-state thermal transformation of ammonium metavanadate

1.1.3 Isopolyoxotungstates

There are several reported polyoxotungstate that formed in aqueous solution of $[WO_4]^{2-}$. Acidification of aqueous solution of monotungstate, $[WO_4]^{2-}$ formed in basic solution leads to the formation of isopolyoxotungstate via dehydrative condensation reactions, such as $[W_7O_{24}]^{6-}$, $[W_{12}O_{40}(OH)_2]^{10-}$, $[H_2W_{12}O_{40}]^{6-}$, and $[W_{10}O_{32}]^{4-}$. Heptatungstate, $[W_7O_{24}]^{6-}$ and paratungstate B, $[W_{12}O_{40}(OH)_2]^{10-}$ are major polyoxotungstate species in the aqueous solution at pH above 5.[15] In a solution, heptatungstate is more stable, while paratunsgatate B is more likely to be crystallized from the solution. Heptatungstate is the main species in fresh solutions under neutral conditions, paratungstate B, $[W_{12}O_{40}(OH)_2]^{10-}$ crystallizes in the aging heptatungstate solution an hour after preparation. The reverse transformation can also occur, paratungstate B anions partly transform to heptatungstate during heating of $[W_{12}O_{40}(OH)_2]^{10-}$ solution.[15] Isopolyoxotungstate anions are metastable at pH values lower than 5, except metatungstate anion, α-$[H_2W_{12}O_{40}]^{6-}$.[15,21] When a paratungstate is acidified, pseudometatungstates, $[H_7W_{11}O_{40}]^{7-}$ were formed.[21,22] $[W_{10}O_{32}]^{4-}$ was formed in soution about pH of 1-2 (Figure 1.6).[3,15] The challenge in isolating polyoxotungstates is the low yield and long crystallization time due to the slow equilibrium reaction of the tungstate solution.[15]

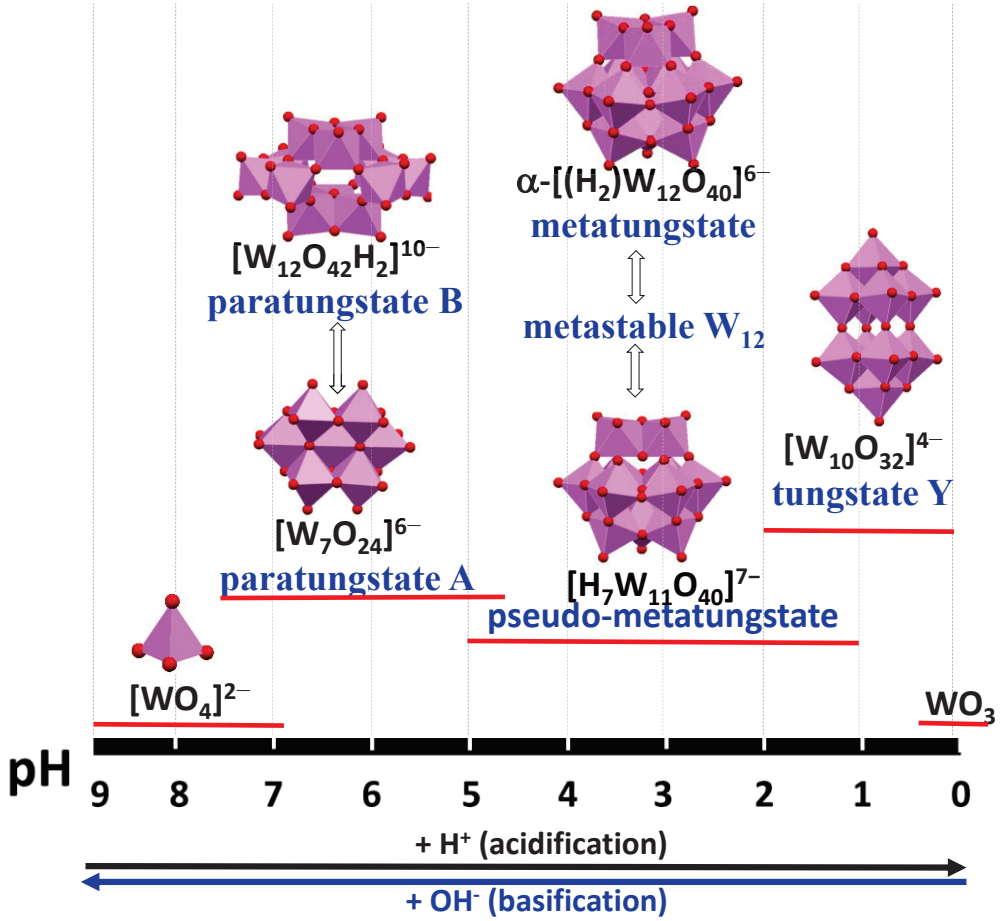

Figure 1.6. Condensation reaction of polyoxotungstate in aqueous solution.

Heat treatment of ammonium tungstate has a comparable effect to acidification because heating removes volatile NH_3 and H_2O. When ammonium paratungstate is heated, structural rearrangement occurs, which causes the destruction of polyoxotungstate ion and formed tungsten oxide (Figure 1.7).[23]

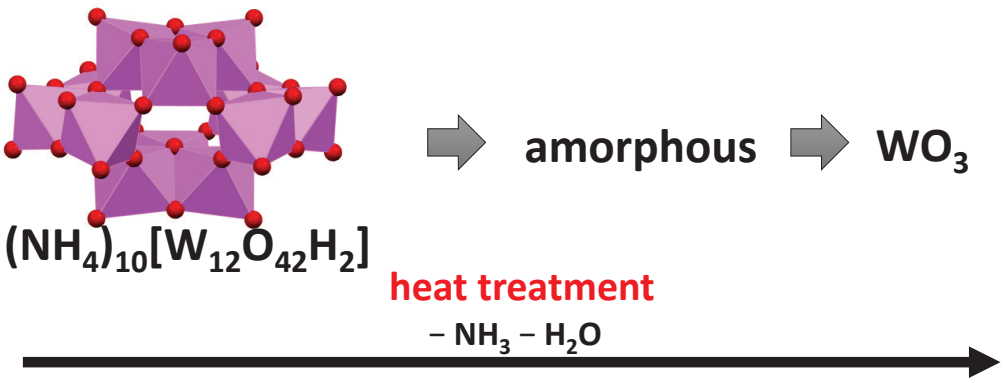

Figure 1.7. Solid-state thermal transformation of ammonium paratungstate.

1.2 Potential applications of polyoxometalates

In this part, I provide a brief overview of certain example of POM application.

1.2.1 Catalyst

Polyoxometalates are useful catalysts due to their various active sites, which include metals, protons, and oxygen atoms. Metals of polyoxometalate catalysts are an important part because they are active sites in acid-base reactions and oxidative reactions. Heteropolyacids are one of the most successful catalysts that are widely used in large-scale industries, their protons can act as Brønsted acids to facilitate acid-catalyzed reactions.[24–27] $H_3PW_{12}O_{40}$ is an effective oxidizing agent and has very strong Brønsted acidity approaching the superacid region,[24,28] and is 200 times more active in homogeneous reactions than H_2SO_4.[29] Guisnet et al. reported that $H_3PW_{12}O_{40}$ is a good catalyst for n-hexane and n-butane isomerizations.[30] $H_3PW_{12}O_{40}$ has advantages as a catalyst such as being non-toxic, reusable, and commercially available.[31]

In other hand, polyoxometalate catalysts that are used in Lewis acid-catalyzed reactions are generally those substituted by metals with high Lewis acidity.[29] Kikukawa et al. reported that $TBA_3H[\gamma\text{-}SiW_{10}O_{36}\{Al(OH_2)\}_2(\mu\text{-}OH)_2]\cdot 4H_2O$ which has two Lewis acid and one Brønsted acid sites is a good catalyst for the intramolecular cyclization of citronellal derivatives. The cyclization is mainly promoted by the aluminum centers as Lewis acid sites. The nature of aluminum is essential for increasing Lewis acidity.[32] The other active sites of polyoxometalates are the surface oxygens, which can act as active sites in base-catalyzed reactions. High negatively charged oxygen atoms on the surface of polyoxometalates are sufficiently basic to react with protons as well as to abstract active protons of organic substances.[29] Some polyoxometalates have been reported as basic catalysts since they are proton-depleted and put in an organic solvent. The basicity of the lacunary polyoxometalates as basic catalysts can be modified by introducing more lacunary sites. Sugahara et al. reported that highly negatively charged polyoxometalate $[\gamma\text{-}H_2GeW_{10}O_{36}]^{6-}$ exhibits good catalytic performance for Knoevenagel reactions.[33]

Heteropolyacids with a Keggin structure are good catalysts that showed high selectivity in the oxidation reaction of isobutane to methacrylic acid and methacrolein due to their acidity (strong and flexible) and redox properties.[34] Mizuno et al. reported that the substitution of large counter-cation such as Cs^+ in $H_3PMo_{12}O_{40}$ affects the surface area due to the formation of micropores and mesopores.[34] This increase in the surface area increased the performance of the catalyst. Jing et al. also synthesized a series of $Cs_x(NH_4)_{3-x}HPMo_{11}VO_{40}$ catalysts with different ammonia/cesium ratios. The results showed that increasing the ammonia/cesium ratio increases the number of acid sites but decreases the specific surface area. Isobutane conversion of 9.6% and a total selectivity to methacrylic acid and methacrolein of 57.1% were obtained over $Cs_{1.7}(NH_4)_{1.3}HPMo_{11}VO_{40}$.[35]

1.2.2 Medicine

Polyoxometalates have been the subject of much research for medical applications. Antiviral and anticancer properties of polyoxometalates have dominated the medicinal chemistry of these compounds.[7,36,37] The advantage of polyoxometalates is that their acidity, polarity, surface charge distribution, redox potentials, and shape that influence the recognition and reactivity of polyoxometalates with target biological macromolecules are modifiable.[36] Samart et al. reported that decavanadate inhibits the growth of Mycobacterium smegmatis and Mycobacterium tuberculosis.[38] It is also reported that decavanadate is effective against bacteria, such as Staphylococcus epidermis, Staphylococcus aureus, and Streptococcus pneumoniae.[39] Galani et al. also reported that decavanadate-carnitine complex exhibits anti-tumor activity against various human cancer cells.[40]

1.2.3 Sensor

Polyoxometalates are widely desirable compounds for sensor-sensitive layers because of the possibility to develop them to have properties that are appropriate for specific sensing applications.[2] Applications of polyoxometalates as electrochemical, optical, and piezoelectric sensors have been reported. Miao et al reported the use of Keggin $[H_3PMo_{12}O_{40}]^-$ polypyrrole nanocomposite as a resistive

humidity sensor.[41] Sensor for detection of toxic gases (NO_x) based on polyoxometalate hybrid compound, $K_4(Py)_2[P_2Mo_{18}O_{62}]$ was reported by Amman et al.[42] An acoustic wave sensor coated with a Keggin-type, $H_5[PV_2Mo_{10}O_{40}]\cdot 11H_2O$ for the detection of 5-hydroxymethylfurfural in honey was reported by Veríssimo et al.[43]

1.2.4 Staining agents

Negative staining is a valuable technique for viewing the detailed morphology and size of the intact virus. The contrast between viruses and the background in electron images results from differences in the electron density of the structures being observed.[44] Negative staining allows for the specific identification of viruses by allowing for the clear distinction of the viral particle from the carbon film background and the provision of precise morphological information such as the size and shape of viruses, but it obscures surface regularities and conceals internal structures.[11,45] One of the most used negative staining agents is uranyl acetate and uranyl formate, these stains provide high-resolution images. Despite their effectiveness, the uranyl salts are both toxic and radioactive, which is require special storage, handling, dan disposal requirements.[46] Polyoxometalates are alternative staining reagent that has been used in observing viruses.[11,47–49] Polyoxometalate solution which is dropped onto the samples concentrates around the virus and inside of components of the viral capsid or envelope. Viral structures that have stained appear as various shades of black, while areas lacking stain show white. It has been reported that Preyssler-type phosphotungstates can be used as effective negative staining reagents for virus observations by transmission electron microscopy.[11] Polyoxometalates fulfill the conditions that are thought to make ideal virus staining agents, notably neutral, stable, and water-soluble since viruses are frequently observed in neutral conditions.

1.3 Objectives and organization of this study

The objectives of this dissertation research were synthesis, characterization, and solid-state thermal transformation of methylammonium polyoxometalates which

are synthesized by reacting methylamine solution with metal oxide (WO_3, V_2O_5, and MoO_3). Afterward, evaluate the performance of synthesized methylammonium molybdate, tungstate, and vanadate as staining reagents for transmission electron microscopy observation of viruses. This thesis consists of 6 chapters, as follows:

Chapter 1 is the **"Introduction"**, which summarizes the research background and the purpose of this study.

Chapter 2 is **"Structure and Thermal Transformations of Methylammonium Molybdate".** Methylammonium monomolybdate, $(CH_3NH_3)_2[MoO_4]$, was synthesized by dissolving MoO_3 in aqueous methylamine solution with a CH_3NH_2/Mo ratio of 4 and then adding N,N-dimethylformamide. The compound crystallized with the space group *Pnma* and comprised monomeric $[MoO_4]^{2-}$and two methylammonium counter cations. Solid state heating of $(CH_3NH_3)_2[MoO_4]$ in air released water and methylammonium to generate various methylammonium isopolymolybdates including $(CH_3NH_3)_8[Mo_7O_{24}\text{-}MoO_4]$, $(CH_3NH_3)_6[Mo_7O_{24}]$, $(CH_3NH_3)_8[Mo_{10}O_{34}]$, and $(CH_3NH_3)_4[Mo_8O_{26}]$, and also molybdenum oxides including hexagonal MoO_3 and orthorhombic MoO_3, which were confirmed by single crystal XRD, powder XRD, IR, Raman, and elemental analysis.

Chapter 3 is **"Structure and Thermal Transformation of Methylammonium Vanadate".** Methylammonium vanadate, $(CH_3NH_3)[VO_3]$, was produced by reacting V_2O_5 with methylamine in aqueous solution, then drying the solution. At around −110 °C, methylammonium vanadate, $(CH_3NH_3)[VO_3]$, exhibited reversible solid-state structural changes. Variable-temperature X-ray single-crystal structure investigatiosn at 23, 0, −50, −100, and −150 °C have revealed that $(CH_3NH_3)[VO_3]$, is composed of methylammonium cations and "snake-like" $([VO_3])_n$ anion chains that propagate along the c-direction in the $Pna2_1$ space group. Reversible structural transformation between −150 and −100 °C due to the reorientation of the methylammonium cations in the crystal packing, which was confirmed by the reversible profiles observed in differential scanning calorimetry. Methylamine and water are released when methylammonium vanadate is heated to 275 °C and V_2O_5 was formed.

Chapter 4 is **"Structure and Thermal Transformations of Methylammonium Tungstate".** The reaction of WO_3 or H_2WO_4 in aqueous methylamine, followed by drying, produced methylammonium paradodecatungstate, $(CH_3NH_3)_{10}[H_2W_{12}O_{42}]\cdot nH_2O$. Two HW_3O_{13} groups with three edge-sharing WO_6 octahedra and two W_3O_{14} groups with two edge-sharing connections made up the $[H_2W_{12}O_{42}]^{10-}$ anion. Although some lattice water was released during the drying process of the obtained material at 70 °C, this had no impact on the $[H_2W_{12}O_{42}]^{10-}$ structure. However, the volume of the unit cell did decrease. The structural changes and lattice water loss were reversed by adding water. Single-crystal and powder X-ray diffraction, Fourier transform infrared, Raman, ^{183}W nuclear magnetic resonance, and ultraviolet-visible spectroscopy were used to prove the existence of paradodecatungstate anions. Amorphous WO_3 was seen as an intermediate result and monoclinic WO_3 as the final product when the methylammonium paradodecatungstate was heated to a temperature of more than 150 °C.

Chapter 5 is **"Application of Methylammonium Polyoxometalates as a Negative Staining Reagent for Transmission Electron Microscopy Observation of Viruses"**. The staining abilities of methylammonium monomolybdate, heptamolybdate-monomolybdate, heptamolybdate, paradodecatungstate, and vanadate were tested. Our results suggest that methylammonium polyoxometalates are a potential negative staining agent for SARS-CoV-2 observation. Methylammonium heptamolybdate staining enabled the contrast and clarity of the stained particles to be clearly observed.

Chapter 6 is **"Conclusions and recommendations"**, provided summary of all chapters and the recommendations are provided for further study.

References

[1] M. T. Pope, A. Müller, *Angew. Chem. Int. Ed.* **1991**, *30*, 34–48.

[2] M. I. S. Veríssimo, D. V. Evtuguin, M. T. S. R. Gomes, *Front. Chem.* **2022**, *10*, 840657.

[3] M. T. Pope, *Heteropoly and Isopoly Oxometalates*, Springer-Verlag,

Berlin, **1983**.

[4] C. L. Hill (Ed.), *Chem. Rev.* **1998**, *98*, 1–390.

[5] L. Cronin (Ed.), *Chem. Soc. Rev.* **2012**, *41*, 7325–7648.

[6] M. T. Pope, M. Sadakane, U. Kortz, *Eur. J. Inorg. Chem.* **2019**, *2019*, 340–342.

[7] A. Bijelic, M. Aureliano, A. Rompel, *Angew. Chem. Int. Ed.* **2019**, *58*, 2980–2999.

[8] M. Ahmadian, M. Anbia, *Energy Fuels* **2021**, *35*, 10347–10373.

[9] S.-S. Wang, G.-Y. Yang, *Chem. Rev.* **2015**, *115*, 4893–4962.

[10] C. A. Scarff, M. J. G. Fuller, R. F. Thompson, M. G. Iadanza, *J. Vis. Exp.* **2018**, *132*, e57199.

[11] K. Sahiro, Y. Kawato, K. Koike, T. Sano, T. Nakai, M. Sadakane, *Sci. Rep.* **2022**, *12*, 7554.

[12] D. L. Long, R. Tsunashima, L. Cronin, *Angew. Chem. Int. Ed.* **2010**, *49*, 1736–1758.

[13] R. I. Maksimovskaya, G. M. Maksimov, *Inorg. Chem.* **2007**, *46*, 3688–3695.

[14] O. W. Howarth, P. Kelly, L. Petterson, *J. Chem. Soc. Dalton Trans* **1990**, 81–84.

[15] N. I. Gumerova, A. Rompel, *Chem. Soc. Rev.* **2020**, *49*, 7568–7601.

[16] T. N. Kovács, D. Hunyadi, A. L. A. de Lucena, I. M. Szilágyi, *J. Therm. Anal. Calorim.* **2016**, *124*, 1013–1021.

[17] J. Fuchs, S. Mahjour, J. Pickardt, *Angew. Chem. lnt. Ed. Engl.* **1976**, *15*, 374–375.

[18] E. E. Hamilton, P. E. Fanwick, J. J. Wilker, *J. Am. Chem. Soc.* **2002**, *124*, 78–82.

[19] V. W. Day, W. G. Klemperer, O. M. Yaghi, *J. Am. Chem. Soc.* **1989**, *111*, 4518–4519.

[20] K.-J. Range, R. Zintl, A. M. Heyns, *Z. Naturforsch. B* **1988**, *43*, 309–317.

[21] J. J. Hastings, O. W. Howarth, *J. Chem. Soc., Dalton Trans.* **1992**, *2*, 209–215.

[22] T. Lehmann, J. Fuchs, *Zeitschrift für Naturforsch. B* **1988**, *43*, 89–93.

[23] D. Hunyadi, I. Sajó, I. M. Szilágyi, *J. Therm. Anal. Calorim.* **2014**, *116*, 329–337.

[24] T. Okuhara, A. Kasai, N. Hayakawa, M. Misono, Y. Yoneda, *Chem. Lett.* **1981**, *10*, 391–394.

[25] I. V. Kozhevnikov, *J. Mol. Catal. A Chem.* **2007**, *262*, 86–92.

[26] I. V. Kozhevnikov, *Chem. Rev.* **1998**, *98*, 171–198.

[27] M. N. Timofeeva, *Appl. Catal. A Gen.* **2003**, *256*, 19–35.

[28] J. Yang, M. J. Janik, D. Ma, A. Zheng, M. Zhang, M. Neurock, R. J. Davis, C. Ye, F. Deng, *J. Am. Chem. Soc.* **2005**, *127*, 18274–18280.

[29] S. Wang, G. Yang, *Chem. Rev.* **2015**, *115*, 4893–4962.

[30] M. Guisnet, P. Bichon, N. S. Gnep, N. Essayem, *Top. Catal.* **2000**, *11*, 247–254.

[31] I. Mohammadpoor-Baltork, M. Moghadam, S. Tangestaninejad, V. Mirkhani, Z. Eskandari, *Z. Naturforsch. B* **2010**, *65*, 461–469.

[32] Y. Kikukawa, S. Yamaguchi, Y. Nakagawa, K. Uehara, S. Uchida, K. Yamaguchi, N. Mizuno, *J. Am. Chem. Soc.* **2008**, *130*, 15872–15878.

[33] K. Sugahara, T. Kimura, K. Kamata, K. Yamaguchi, N. Mizuno, *Chem. Commun.* **2012**, *48*, 8422–8424.

[34] L. Zhang, S. Paul, F. Dumeignil, B. Katrynion, *Catalysts* **2021**, *11*, 87–94.

[35] F. Jing, B. Katryniok, F. Dumeignil, E. Bordes-Richard, S. Paul, *Catal. Sci. Technol.* **2014**, *4*, 2938–2945.

[36] J. T. Rhule, C. L. Hill, D. A. Judd, R. F. Schinazi, *Chem. Rev.* **1998**, *98*, 327–357.

[37] M. Aureliano, N. I. Gumerova, G. Sciortino, E. Garribba, A. Rompel, D. C. Crans, *Coord. Chem. Rev.* **2021**, *447*, 214143.

[38] N. Samart, Z. Arhouma, S. Kumar, H. A. Murakami, D. C. Crick, D. C. Crans, *Front. Chem.* **2018**, *6*, 1–16.

[39] A. Bijelic, M. Aureliano, A. Rompel, *Chem. Commun.* **2018**, *54*, 1153–1169.

[40] A. Galani, V. Tsitsias, D. Stellas, V. Psycharis, C. P. Raptopoulou, A.

Karaliota, *J. Inorg. Biochem.* **2015**, *142*, 109–117.

[41] J. Miao, Y. Chen, Y. Li, J. Cheng, Q. Wu, K. W. Ng, X. Cheng, R. Chen, C. Cheng, Z. Tang, *ACS Appl. Nano Mater.* **2018**, *1*, 564–571.

[42] M. Ammam, E. B. Easton, *J. Mater. Chem.* **2011**, *21*, 7886–7891.

[43] M. I. S. Veríssimo, J. A. F. Gamelas, D. V. Evtuguin, M. T. S. R. Gomes, *Food Chem.* **2017**, *220*, 420–426.

[44] W. Baschong, U. Aebi, *Negative Staining. Cell Biology: A Laboratory Handbook, 3rd Ed, Vol. 3*, Academic Press, Cambridge, Massachusetts, **2006**.

[45] S. Brenner, R. W. Horne, *Biochim. Biophys. Acta* **1959**, *34*, 103–110.

[46] United States Nuclear Regulatory Commission. General Licence Uses of Nuclear Materials. https://www.nrc.gov/mater ials/ miau/general-use.html (2020). Accessed 31 Dec 2022.

[47] C. A. Scarff, M. J. G. Fuller, R. F. Thompson, M. G. Iadaza, *J. Vis. Exp.* **2018**, *132*, e57199.

[48] B. Franzetti, G. Schoehn, J.-F. Hernandez, M. Jaquinod, R. W. H. Ruigrok, G. Zaccai, *EMBO J.* **2002**, *21*, 2132–2138.

[49] N. C. Sukmana, J. Shinogi, A. Yamamoto, A. Higashiura, T. Sakaguchi, M. Sadakane, *Eur. J. Inorg. Chem.* **2022**, e202200322.

CHAPTER 2

Structure and Thermal Transformation of Methylammonium Monomolybdate

2.1 Introduction

Polyoxomolybdates are one of important polyoxometalates. Isopolyoxomolybdates have been developed as corrosion inhibitors,[1,2] supercapacitors,[3] anticancer agents,[4] and Mo sources for Mo-based oxide materials.[5,6] The formation of isopolyoxomolybdates in an aqueous solution is affected by acidity of the solution. Monomolybdate, $[MoO_4]^{2-}$, present in basic to neutral solution, dehydrately condenses by addition of proton and addition of more proton produces more condensed polyoxomolybdates such as $[Mo_7O_{24}]^{6-}$, $[Mo_8O_{26}]^{4-}$, and $[Mo_{36}O_{112}(H_2O)_{16}]^{8-}$ (Scheme 2.1).[7–9] The dehydrative condensation degrees increase when more acids are added until they are fully transformed to MoO_3.

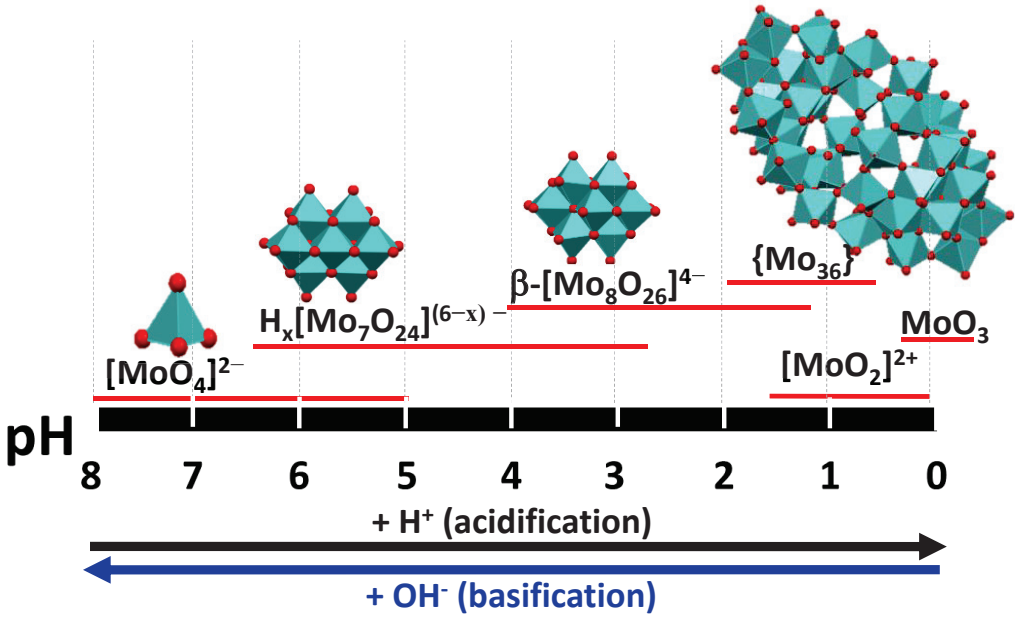

Scheme 2.1. Effect of acidity on the formation of isopolymolybdates in aqueous solutions.

When heat is applied to the ammonium molybdate which releases volatile base, NH_3 and H_2O, it has the same effect as when acid is added. $(NH_4)_2[MoO_4]$ is produced by dissolving MoO_3 in an ammonia solution. By heating, the volatile NH_3 and water formed from NH_4^+ and oxygen atoms in metalates are diminished, and solid-state condensation is encouraged. It has been reported that solid-state heating of $(NH_4)_2[MoO_4]$ formed various ammonium isomolybdates, including $(NH_4)_2[Mo_2O_7]$, $(NH_4)_2[Mo_3O_{10}]$, and $(NH_4)_2[Mo_4O_{13}]$ (same to $(NH_4)_4[Mo_8O_{26}]$) and that further heating produced hexagonal-MoO_3 and orthorhombic-MoO_3 (Scheme 2.2).[10] In contrast, solid state heating of $(NH_4)_6[Mo_7O_{24}]$ produced $(NH_4)_8[Mo_{10}O_{34}]$ and $(NH_4)_2[Mo_4O_{13}]$ (same to $(NH_4)_4[Mo_8O_{26}]$), and additional heating generated hexagonal-MoO_3 and orthorhombic MoO_3 (Scheme 2.3).[10,11]

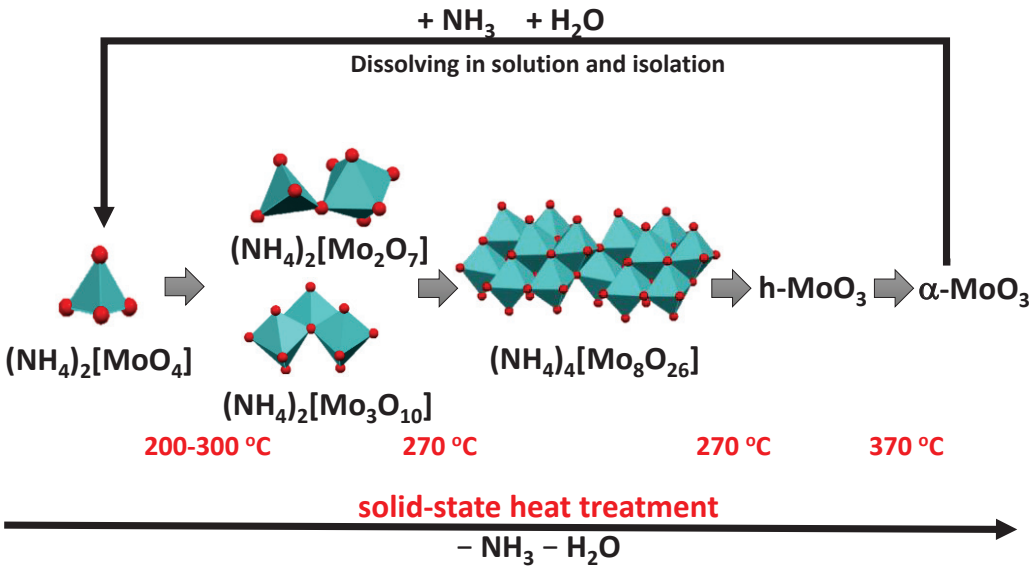

Scheme 2.2. Formation of ammonium monomolybdate via the reaction of MoO_3, H_2O, and NH_3, and its solid-state thermal transformation.

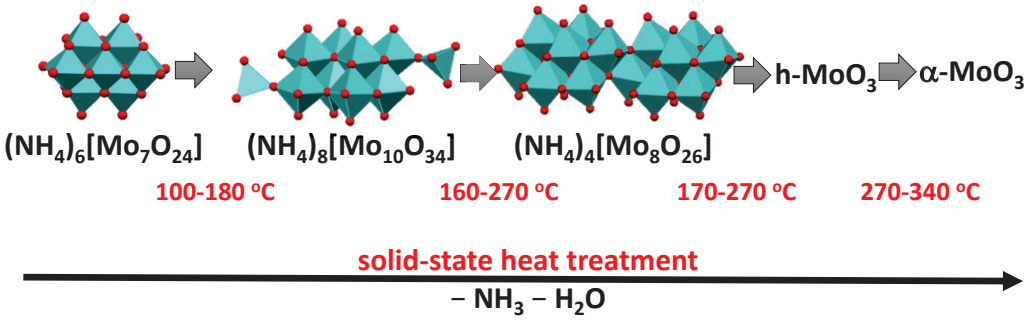

Scheme 2.3. Solid-state thermal transformation of ammonium heptamolybdate.

We are interested in polyoxometates formed by reactions between a metal oxide and methylamine, and we reported that the reaction of V_2O_5 or WO_3 with methylamine and subsequent drying formed methylammonium vanadate, $(CH_3NH_3)[VO_3]$ (chapter 3)[12] and methylammonium paradodecatungstate, $(CH_3NH_3)_{10}[H_2W_{12}O_{42}]$ (chapter 4),[13] respectively. It has been reported that the reaction of MoO_3 in aqueous methylamine solution and subsequent drying produced methylammonium heptamolybdate, $(CH_3NH_3)_6[Mo_7O_{24}]$. Methylammonium heptamolybdate is a good Mo source for the synthesis of orthorhombic Mo-V mixed oxide, a potential oxidation catalyst.[14] In addition, it has been reported that $(CH_3NH_3)_6[Mo_7O_{24}]$ is an effective Mo source for the production of orthorhombic Mo-V-Cu oxide.[15] However, $(CH_3NH_3)_6[Mo_7O_{24}]$ was only identified by Raman spectroscopy and elemental analysis, and a single crystal structure investigation has not yet provided proof of the structure. Consequently, it is necessary to understand the precise structure and the influence of heating temperature on the structure of methylammonium molybdate.

In this work, we synthesize methylammonium monomolybdate, $(CH_3NH_3)_2[MoO_4]$, by dissolving MoO_3 in an aqueous methylamine solution, along with the subsequent solid state thermal structure transformation to $(CH_3NH_3)_8[Mo_7O_{24}\text{-}MoO_4]$, $(CH_3NH_3)_6[Mo_7O_{24}]$, $(CH_3NH_3)_8[Mo_{10}O_{34}]$, $(CH_3NH_3)_4[Mo_8O_{26}]$, hexagonal-MoO_3, and orthorhombic-MoO_3 (Scheme 2.4) which was different from the thermal behavior of ammonium polyoxomolybdates.

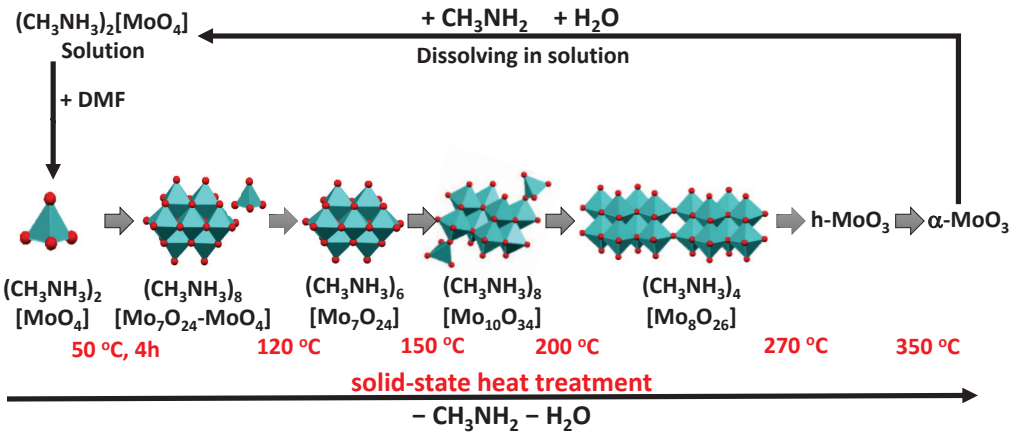

Scheme 2.4. Formation of methylammonium monomolybdate via the reaction of MoO_3, H_2O, and CH_3NH_2, and its solid-state thermal transformation.

2.2 Experimental section

Materials. All chemicals were reagent-grade. 40% methylamine and vanadyl sulfate were purchased from Kanto Chemical CO., Inc., and molybdenum trioxide, oxalic acid, sulfuric acid, and N,N-dimethylformamide (DMF) were purchased from Wako Pure Chemical Industries, Ltd., Homemade deionized water (Millipore, Elix, USA, MA) was used throughout this study.

Preparation of $(CH_3NH_3)_2[MoO_4]$. MoO_3 (2.1 g, Mo: 15 mmol) was stirred with 5 mL 40% methylamine solution in a glass beaker for 30 min at room temperature to produce clear colorless solution. An excess of DMF (15 mL) was added to the solution, and formed white solid (2.28 g) was filtered. IR, $\tilde{\nu}/cm^{-1}$(KBr): 3070(s), 2863(m), 2730(m), 2159(m), 1627(m), 1540(m), 1473(m), 1409(w), 1261(w), 958(m, sh), 898(vs), 879(vs), 836(vs), 676921(s, sh), 892(vs), 840 (s), 784(s, sh), 676(s) cm^{-1}. Elemental analysis calcd. for $(CH_3NH_3)_2[MoO_4]$: C 9.92, H 5.84, N 11.57; found, C 10.09, H 5.36, N 11.6.

Crystallization of $(CH_3NH_3)_2[MoO_4]$. MoO_3 (0.7 g, Mo: 5 mmol) was stirred with 40% methylamine solution (1.7 ml) in a glass container for 30 min at room temperature which produced clear colorless solution. DMF (1.7 mL) was added to the solution, and colorless crystals were formed.

Calcination of $(CH_3NH_3)_2[MoO_4]$. $(CH_3NH_3)_2[MoO_4]$ (1 g) was calcined under air to 50 °C at a heating rate of 10 °C/min and the temperature was maintained for 4 h. In the case of calcination at 100, 120, 150, 200, 250, 270, and 600 °C, the temperature was raised at a heating rate of 10 °C/min and the final temperature was maintained for 1 h under air. $(CH_3NH_3)_8[Mo_7O_{24}\text{-}MoO_4]\cdot 4H_2O$, $(CH_3NH_3)_6[Mo_7O_{24}]$, $(CH_3NH_3)_8[Mo_{10}O_{34}]\cdot 2H_2O$, $(CH_3NH_3)_4[Mo_8O_{26}]$, hexagonal MoO_3 and orthorhombic MoO_3 were formed at temperature 50, 120, 150, 200, 270, and 600 °C, respectively.

$(CH_3NH_3)_8[Mo_7O_{24}\text{-}MoO_4]\cdot 4H_2O$, $\tilde{\nu}/cm^{-1}$(KBr): 3430(m), 1631(m), 1496(m), 1469(m), 1425(w), 1265(w), 921(s, sh), 892(vs), 840 (s), 673(vs) cm^{-1}. Elemental analysis calcd. for $(CH_3NH_3)_8[Mo_7O_{24}\text{-}MoO_4]\cdot 4H_2O$: C 6.22, H 3.66, N 7.26; found, C 6.21, H 3.83, N 7.13.

$(CH_3NH_3)_6[Mo_7O_{24}]$, $\tilde{\nu}$/cm^{-1}(KBr): 3438(m), 1629(m), 1496(m), 1471(m), 1423(w), 1263(w), 921(s, sh), 892(vs), 840 (s), 676(vs) cm^{-1}. Elemental analysis calcd. for $(CH_3NH_3)_6[Mo_7O_{24}]$: C 5.77, H 2.91, N 6.74; found, C 5.45, H 2.77, N 6.11.

$(CH_3NH_3)_8[Mo_{10}O_{34}]\cdot 2H_2O$, $\tilde{\nu}$/cm^{-1}(KBr): 3455(m), 1602(m), 1483(m), 1425(w), 1263(w), 912 (s), 873(vs), 840(s), 684(vs) cm^{-1}. Elemental analysis calcd. for $(CH_3NH_3)_8[Mo_{10}O_{34}]\cdot 2H_2O$: C 5.35, H 2.92, N 6.24; found, C 5.15, H 2.62, N 5.85.

$(CH_3NH_3)_4[Mo_8O_{26}]$, $\tilde{\nu}$/cm^{-1}(KBr): 3444(m), 1589(m), 1477(m), 1425(w), 1263(w), 954 (s), 931 (s, sh), 896 (s), 869(vs), 806(s), 715 (s, sh), 667(vs) cm^{-1}. Elemental analysis calcd. for $(CH_3NH_3)_4[Mo_8O_{26}]$: C 3.66, H 1.84, N 4.27; found, C 3.69, H 1.69, N 4.15.

Recrystallization of $(CH_3NH_3)_8[Mo_7O_{24}\text{-}MoO_4]\cdot 4H_2O$. A 10 g of $(CH_3NH_3)_8[Mo_7O_{24}\text{-}MoO_4]\cdot 4H_2O$ was heated at 60 °C with 3 mL of water in a glass vessel until all solids were completely dissolved. The temperature was slowly decreased to room temperature and the colorless crystal was obtained which is suitable for single-crystal X-ray structure analysis.

Recrystallization of $(CH_3NH_3)_6[Mo_7O_{24}]$. A 0.1 g of $(CH_3NH_3)_6[Mo_7O_{24}]$ was dissolved in 0.2 mL water, 0.2 mL of DMF was added into the solution, and placed in a closed 10 mL glass vessel. After one day, the colorless crystal suitable for single-crystal X-ray structure analysis was obtained.

Recrystallization of $(CH_3NH_3)_8[Mo_{10}O_{34}]\cdot 2H_2O$. A 0.2 g of heated solid at 120 °C was dissolved in 0.3 mL water and heated at 60 °C until all solids were completely dissolved. The temperature was slowly decreased to room temperature and the colorless crystal was obtained which is suitable for single-crystal X-ray structure analysis.

Recrystallization of $(CH_3NH_3)_4[Mo_8O_{26}]$. A 56 mg of $(CH_3NH_3)_2[MoO_4]$ was dissolved in 1 mL water and the pH of the solution was adjusted to 4 by adding 1M H_2SO_4. After one month, the colorless crystal suitable for single-crystal X-ray structure analysis was obtained.

Analytical techniques. Powder X-ray diffraction patterns were measured on a Bruker D2 PHASER 2nd Gen using Cu-K_α radiation. The samples were ground and

placed on a sample holder, and the XRD profiles were recorded at 2θ = 3–80°. FT-IR spectra were obtained using a NICOLET 6700 FT-IR spectrometer (Thermo Fischer Scientific) in the range of 650–4000 cm^{-1} in KBr pellets. TG-DTA was carried out using a TG-DTA7300 instrument (SII, Japan) with an air and nitrogen flow of 200 mL s^{-1}. Temperature programmed desorption (TPD) was carried out using a BELCAT II – BELMASS system (MicrotracBEL Corp.) instrument under helium flow. The rate of temperature increase was 10 °C min^{-1} and the maximum temperature was 600 °C. Ultraviolet–visible spectra were obtained using an Agilent 8453 UV-visible spectrometer in the range 190–1100 nm with a cell length of 1 cm. Raman spectra were collected using a JASCO RMP-510 with a 532.0 nm laser and each spectrum was collected for 1 s and accumulated three times. N_2 adsorption isotherms were measured using a BELSORP-max (Bel Japan) system, and the solids were outgassed under vacuum conditions at 300 °C for 2 h before measurement. The particle morphologies were observed using Scanning Electron Microscopy (Hitachi S4800). CHN analyses were performed at Division of Instrumental Analysis, Okayama University.

X-ray crystallography. Single-crystal X-ray diffraction data of $(CH_3NH_3)_2[MoO_4]$, $(CH_3NH_3)_8[Mo_7O_{24}\text{-}MoO_4]\cdot 4H_2O$, and $(CH_3NH_3)_6[Mo_7O_{24}]$ were collected on Bruker APEX-II CCD at 100 K using monochromatic Mo-K_α radiation (α=0.71073 Å). Data reduction and space group determination were performed using the Bruker APEX 3 suite.[16] Absorption correction was applied using a multi-scan technique (SADABS).[16] The structure was solved by direct methods using SHELXT[17] and refined using SHELXL[18] using the SHELXle[19] interface. The carbon and nitrogen atoms of the methylammonium cations were located in the electron density map, where the cations are hydrogen bonded to the anionic cluster. The crystal data of methylammonium isopolymolybdate are summarized in Table 2.1. CCDC 2222172, 2125533, 2222173, 2222175, and 2222174 contain crystallographic data for methylammonium monomolybdate, methylammonium heptamolybdate-monomolybdate, methylammonium heptamolybdate, methylammonium decamolybdate, and methylammonium

octamolybdate, respectively, which can be obtained free of charge from the Cambridge Crystallographic Data Centre (CCDC).

Table 2.1. Crystal data for methylammonium isopolyoxomolybdates

Empirical formula	$(CH_3NH_3)_2$ $[MoO_4]$	$(CH_3NH_3)_8$ $[Mo_7O_{24}$-$MoO_4]\cdot 4H_2O$	$(CH_3NH_3)_6$ $[Mo_7O_{24}]$	$(CH_3NH_3)_8$ $[Mo_{10}O_{34}]\cdot 2H_2O$	$(CH_3NH_3)_8$ $[Mo_{10}O_{34}]\cdot 2H_2O$	$(CH_3NH_3)_4$ $[Mo_8O_{26}]$
M.W. (g/mol)	224.08	1552.06	1247.99	1795.9	1795.9	655.90
Temp. (K)	90	100	90	295	100	123
Crystal system	Orthorhombic	Triclinic	Triclinic	Monoclinic	Monoclinic	Triclinic
Space group	*Pnma*	$P\bar{1}$	$P\bar{1}$	$P2_1/n$	$P2_1/n$	$P\bar{1}$
a (Å)	9.3684(18)	12.0872(9)	10.4409(7)	12.596(2)	10.5245(8)	8.135(2)
b (Å)	6.8961(13)	13.2298(10)	10.8297(8)	17.175(2)	17.1868(13)	8.825(3)
c (Å)	11.911(2)	15.1650(11)	16.0303(11)	10.653(2)	12.5003(9)	10.774(3)
α (°)	90	108.0420(10)	100.611(1)	90	90	91.009(3)
β (°)	90	105.2980(10)	90.909(1)	91.04(2)	91.1630(10)	105.986(3)
γ (°)	90	100.3430(10)	118.343(1)	90	90	111.124(3)
V (Å^3)	769.5(3)	2132.0(3)	1556.79	2304.25	2260.6(3)	687.7(3)
Z	4	2	2	2	2	1
$D_{calcd.}$ (g/cm^{-3})	1.934	2.418	2.662	2.588	2.683	3.167
μ (mm^{-1})	1.663	2.378	2.825		2,783	3.633
Radiation	Mo Kα (λ =0.71073 Å)					
F(000)	448.0	1504.0	1200.0		1728	620.0
Index ranges	$-8 \le h \le 12$ $-8 \le k \le 9$ $-15 \le l \le 14$	$-16 \le h \le 15$ $-17 \le k \le 17$ $-20 \le l \le 19$	$-13 \le h \le 13$ $-14 \le k \le 14$ $-20 \le l \le 21$		$-13 \le h \le 13$ $-22 \le k \le 22$ $-16 \le l \le 16$	$-10 \le h \le 10$ $-11 \le k \le 11$ $-14 \le l \le 13$
G.O.F.	1.048	1.037	1.045		1.017	1.011
R indexes [$I > 2\sigma(I)$]	$R_1 = 0.0206$; $wR_2 = 0.0480$	$R_1 = 0.0171$; $wR_2 = 0.0436$	$R_1 = 0.0169$; $wR_2 = 0.0395$	$R_1 = 0.041$; $wR_2 = 0.041$	$R_1 = 0.0227$; $wR_2 = 0.0474$	$R_1 = 0.0261$; $wR_2 = 0.0537$
R indexes [all data]	$R_1 = 0.0290$; $wR_2 = 0.0520$ *This work*	$R_1 = 0.0185$; $wR_2 = 0.0442$ *This work*	$R_1 = 0.0192$; $wR_2 = 0.0403$ *This work*	*reported by Yamase*[20]	$R_1 = 0.0301$; $wR_2 = 0.0227$ *This work*	$R_1 = 0.0349$; $wR_2 = 0.0567$ *This work*

2.3 Result and discussion

2.3.1 Synthesis, crystal structure, and characterization of methylammonium monomolybdate

Methylammonium monomolybdate, $(CH_3NH_3)_2[MoO_4]$, was produced by dissolving MoO_3 in a 40% methylamine solution with a methylamine/Mo ratio of 4, followed by the addition of N,N-dimethylformamide (DMF).

Single-crystal X-ray structural analysis indicated that monomolybdate, $[MoO_4]^{2-}$, formed with two methylammonium ($CH_3NH_3^+$) counter cations in the space group *Pnma* (Table 2.1). Four oxygen atoms surround the molybdenum

cation tetrahedrally (Figure 2.1) at angles between 108.98° and 109.95° (O-Mo-O) (Table 2.2). Comparable to the average tetrahedral Mo-O lengths observed in $K[MoO_4]$ (1.76 Å)[21] and $(NH_4)[MoO_4]$ (1.76 Å)[22], the Mo-O distances are nearly identical between 1.75 and 1.78. (Table 2.3). The $[MoO_4]^{2-}$ ion hydrogen-bonded to methylammonium through N–H···O interactions with distances between 2.73 and 2.80 Å (Figure 2.1). O1 atoms engaged in two hydrogen bonds, whereas O2 and O3 atoms each engaged in one hydrogen bond.

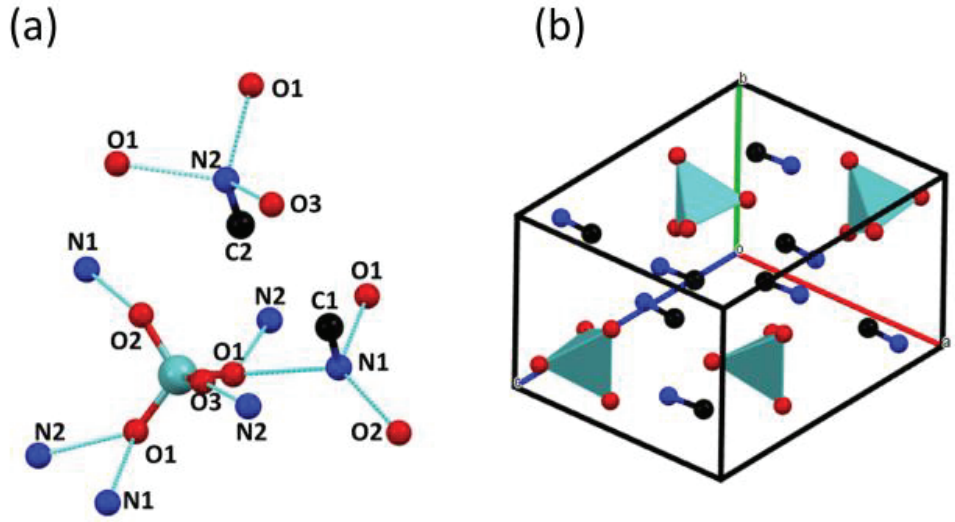

Figure 2.1. (a) Ball-and-stick representation and atom labeling for methylammonium monomolybdate, and (b) packing of molecules in a unit cell. Hydrogen atoms are not shown for clarity. Light blue, red, black, and blue balls represent molybdenum, oxygen, carbon, and nitrogen atoms, respectively. Light blue lines represent the hydrogen bonds between N and O atoms, which are shorter than 3.0 Å.

Table 2.2. Selected O–Mo–O angles (°) of $[MoO_4]^{2-}$.

Bonds	Angle (°)
O2-Mo1-O3	109.95(10)
O2-Mo1-O1	109.95(6)
O3-Mo1-O1	108.98(6)
O2-Mo1-O1	109.95(6)
O3-Mo1-O1	108.98(6)
O1-Mo1-O1	109.00(10)

Table 2.3. Selected bond distances (Å) of $[MoO_4]^{2-}$.

Bonds	Length (Å)

Mo1-O2	1.748(2)
Mo1-O3	1.755(2)
Mo1-O1	1.7800(15)
Mo1-O1	1.7801(15)

The powder XRD pattern simulated from a single-crystal structure matched well with experimental XRD patterns (Figure 2.2), suggesting that the resulting solid has the same crystal structure and the phase purity of the bulk powders is satisfactory. The difference between the simulated and experimental peak intensities might be due to the preferred orientation of the powder sample.

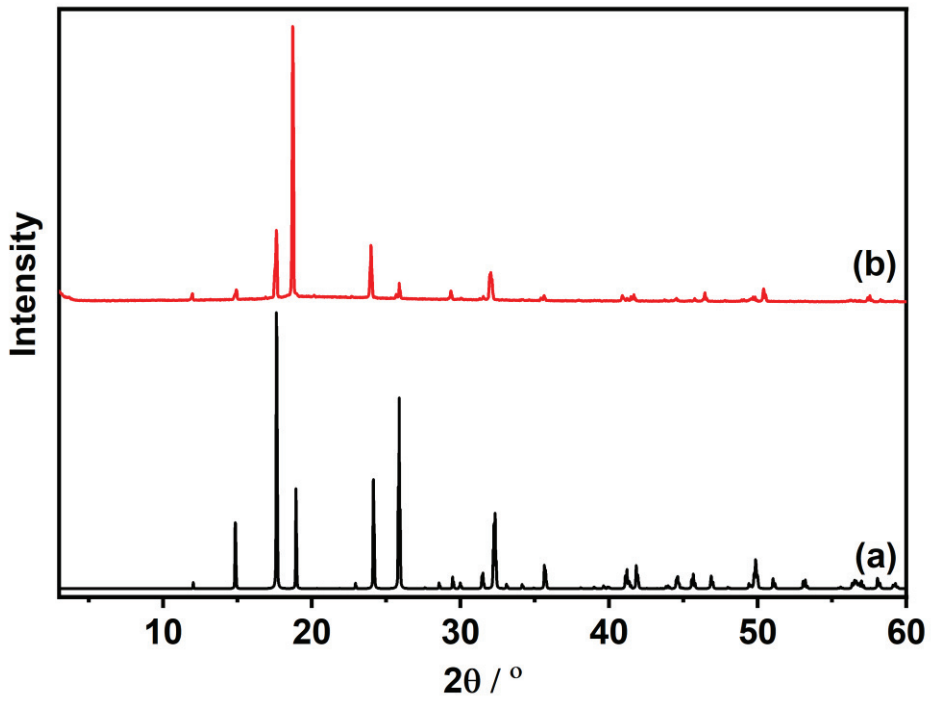

Figure 2.2. XRD patterns of methylammonium monomolybdate, $(CH_3NH_3)_2[MoO_4]$: (a) simulated pattern obtained from single crystal X-ray structure analysis data and (b) observed pattern.

The FT-IR spectrum (Figure 2.3) exhibits bands at 1467 and 1261 cm^{-1} that correspond to NH_3^+ bending and CH_3-NH_3^+ rocking, respectively. In addition, the IR band at 956 cm^{-1} corresponds to the symmetric stretching vibration of $[MoO_4]^{2-}$, whereas the IR bands at 833, 879, and 898 cm^{-1} correspond to the asymmetric stretching vibration of $[MoO_4]^{2-}$.[23]

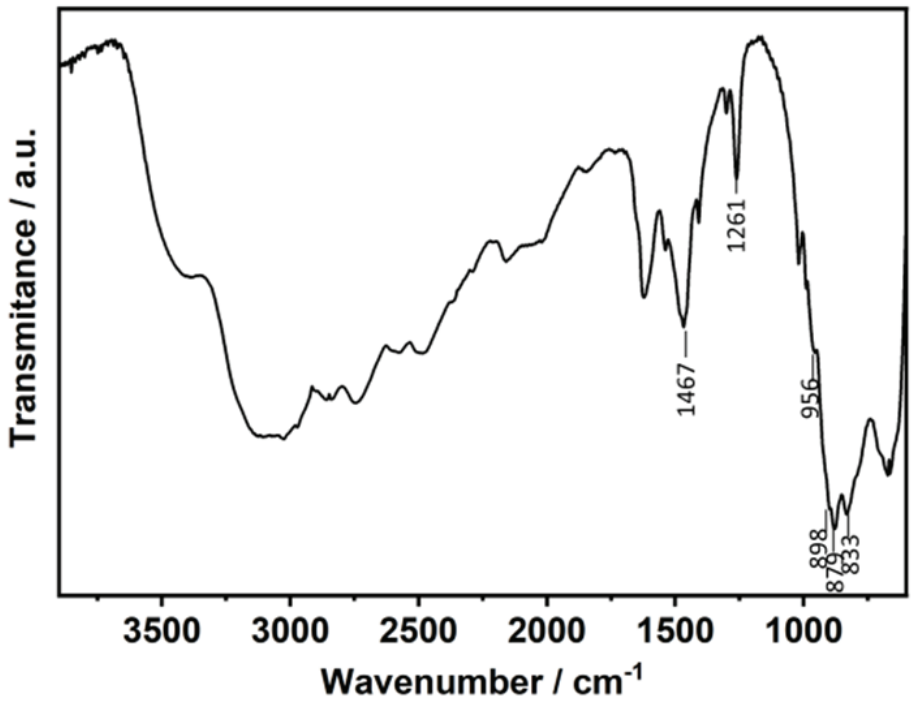

Figure 2.3. FT-IR spectrum of methylammonium monomolybdate, $(CH_3NH_3)_2[MoO_4]$.

Figure 2.4 shows the Raman spectra of sodium monomolybdate, methylamine hydrochloride, and methylammonium monomolybdate in solid and solution. The presence of methylammonium as a counter-cation is indicated by a Raman band of about 1001 cm^{-1} in the methylammonium monomolybdate spectrum, which is attributed to C-N stretching vibration. Strong Raman bands at 898 and 315 cm^{-1} in methylammonium monomolybdate can be attributed to the vibration of symmetric stretching and bending of $[MoO_4]^{2-}$, respectively. Additionally, the asymmetric stretching of MoO_4 units can be attributed to the Raman band at 838 cm^{-1}.[24]

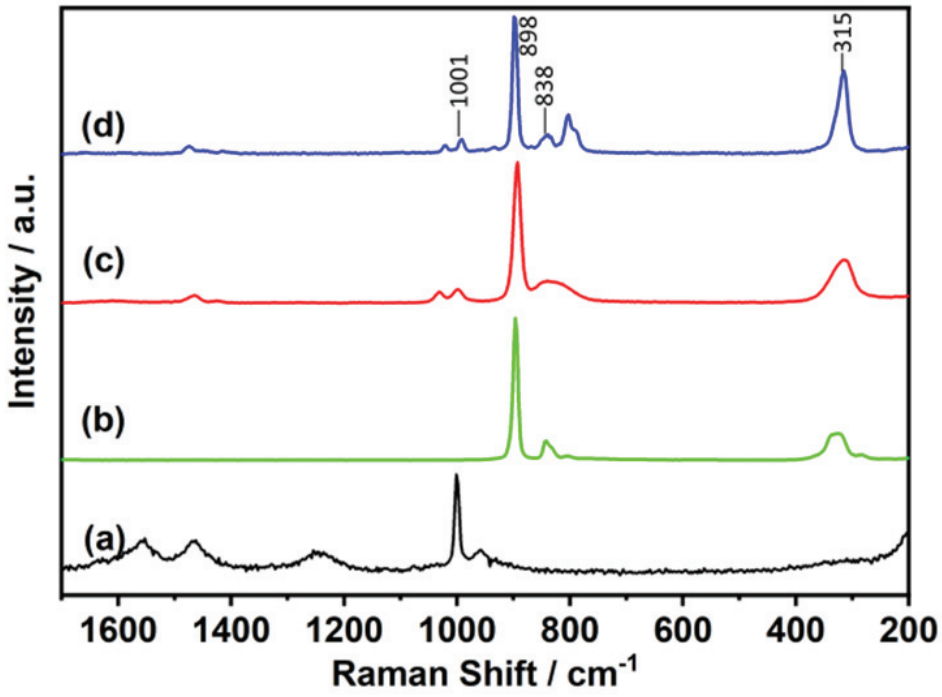

Figure 2.4. Raman spectra of (a) methylamine hydrochloride, $CH_3NH_3^+Cl^-$, (b) sodium monomolybdate, $Na_2[MoO_4]$, and (c) methylammonium monomolybdate, $(CH_3NH_3)_2[MoO_4]$ prepared in the synthesis solution, and (d) isolated $(CH_3NH_3)_2[MoO_4]$ solid.

Raman and UV-vis spectra were used to confirm the presence of $[MoO_4]^{2-}$ in the reaction mixture of methylamine and MoO_3 (Figures 2.4(c) and 2.5). The solution Raman spectrum and the solid state spectrum were comparable. The UV-vis spectrum of reaction mixture has a peak at 207 nm and a shoulder near 230 nm that match those in the literature spectrum of $[MoO_4]^{2-}$.[25]

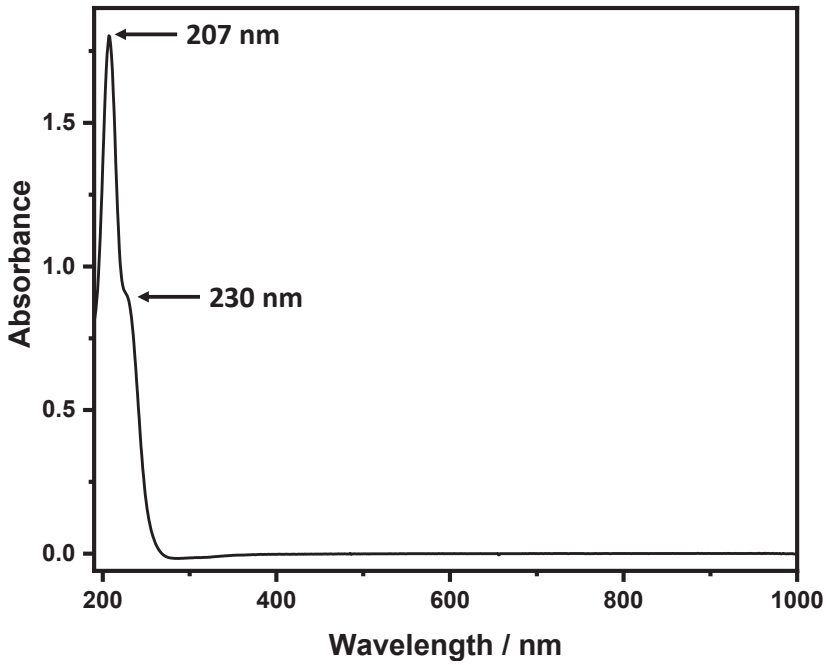

Figure 2.5. UV–vis spectrum of solution the reaction of MoO_3 and methylamine (solution concentration: 5 μL/50 mL H_2O).

2.3.2 Solid-state thermal transformation of methylammonium monomolybdate

2.3.2.1 TG, DTA, and TPD analysis of $(CH_3NH_3)_2[MoO_4]$

A weight loss of about 36% was shown by the thermogravimetry-differential thermal analysis (TG-DTA) diagram of methylammonium monomolybdate in air flow (Figure 2.6). This weight loss is due to the formation of MoO_3 (36%) by releasing 2 mol of methylamine and 1 mol of water from $(CH_3NH_3)_2[MoO_4]$ (Table 2.4).

Table 2.4. Formula of methylammonium isopolymolybdate estimated of TG and CHN elemental analysis.

Formula	Weight Loss (wt%)[a] Calc.(obs.)	C (wt%) Calc.(obs.)	H (wt%) Calc.(obs.)	N (wt%) Calc.(obs.)
$(CH_3NH_3)_2[MoO_4]$	35.8(36.1)	9.92(10.09)	5.84(5.36)	11.57(11.60)
$(CH_3NH_3)_8[Mo_7O_{24}\text{-}MoO_4]\cdot 4H_2O$	25.5(24.6)	6.22(6.21)	3.66(3.83)	7.26(7.13)
$(CH_3NH_3)_6[Mo_7O_{24}]$	19.3(19.1)	5.77(5.45)	2.91(2.77)	6.74(6.11)
$(CH_3NH_3)_8[Mo_{10}O_{34}]\cdot 2H_2O$	19.9(20.3)	5.35(5.15)	2.92(2.62)	6.24(5.85)
$(CH_3NH_3)_4[Mo_8O_{26}]$	13.4(12.1)	3.66(3.69)	1.84(1.69)	4.27(4.16)
Hexagonal-$MoO_3(CH_3NH_2)_{0.15}$	2.9(2.4)	1.21(0.99)	0.51(0.28)	1.41(1.56)

[a] estimated by TG-DTA under air flow up to ca. 500 °C.

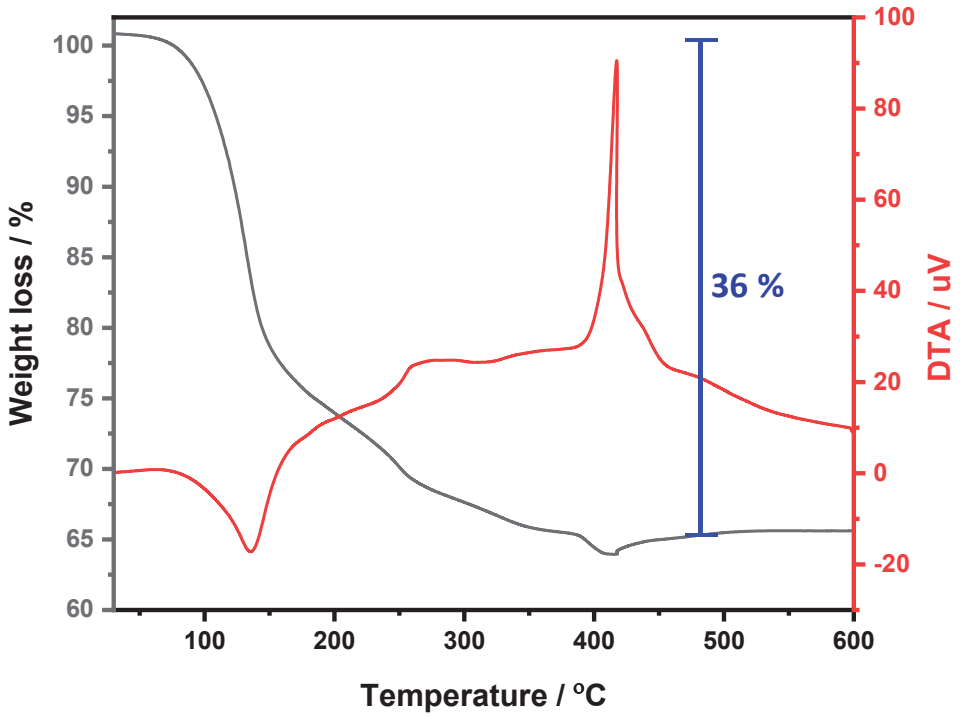

Figure 2.6. TG/DTA curves of methylammonium monomolybdate in air flow.

Temperature-programmed desorption-mass spectrometry (TPD-MS) under helium flow and TG-DTA under nitrogen flow were used to study dehydrated condensation caused by solid state heating (Figure 2.7). Several gasses with m/z values of 44, 31, 30, 28, 18, 17, and 16 were observed (Table 2.5). The decomposition starts when the temperature reaches about 70 °C. These decompositions are in accordance with the IR spectra of heated solid, the intensity of the IR bands associated with the methylammonium and water reduced (Figure 2.8), suggesting that some of these substances were evaporated. In addition to H_2O and CH_3NH_2, the degradation and oxidized compounds of methylammonium such as NH_3, CO, N_2, NO, CO_2, and N_2O can be observed at temperatures over 160 °C, suggesting that a redox reaction between methylammonium and Mo has occurred in the atmosphere of inert gas. Similar degradation and oxidation reactions of methylamine have been reported in methylammonium paradodecatungstate and vanadate.[12,13]

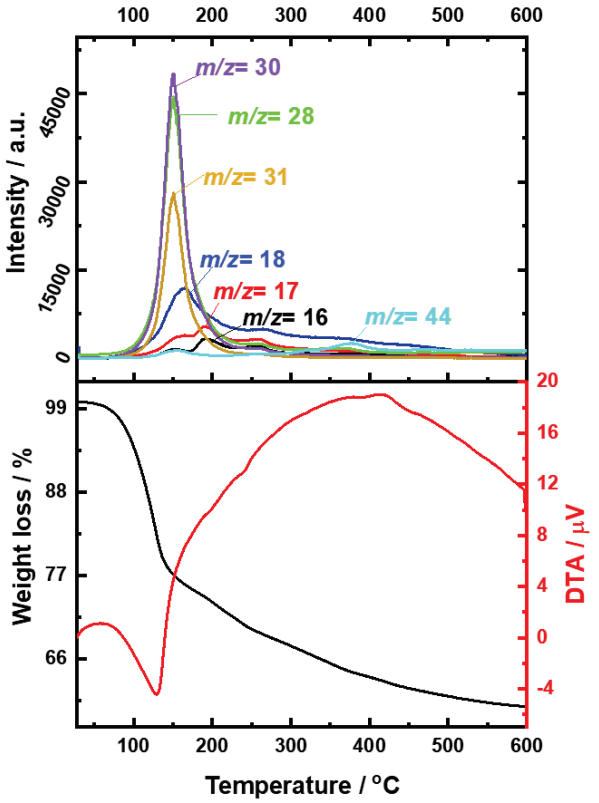

Figure 2.7. TG/DTA curves and TPD-MS profile of methylammonium monomolybdate.

Table 2.5. Mass-to-charge ratio (m/z) and intensity ratio of the gas produced during TPD analysis.

Compound	m/z	Intensity ratio
CH_3NH_2	30, 31, and 28	100/65/54
H_2O	18, 17, and 16	100/21/1
NH_3	17 and 16	100/80
CO_2	44, 28, and 16	100/10/10
CO	28 and 16	100/3
N_2O	44, 30, 28, and 16	100/31/11/5
NO	30 and 16	100/3
N_2	28	100

2.3.2.2 Synthesis and characterization of $(CH_3NH_3)_8[Mo_7O_{24}\text{-}MoO_4]$

By heating the methylammonium monomolybdate in air, we found that the powder XRD patterns were changed (Figure 2.9). By heating methylammonium monomolybdate at 50 °C for four hours, the first transformation was observed. The obtained solid was recrystallized in hot water to produce colorless crystals suitable for X-ray structural analysis.

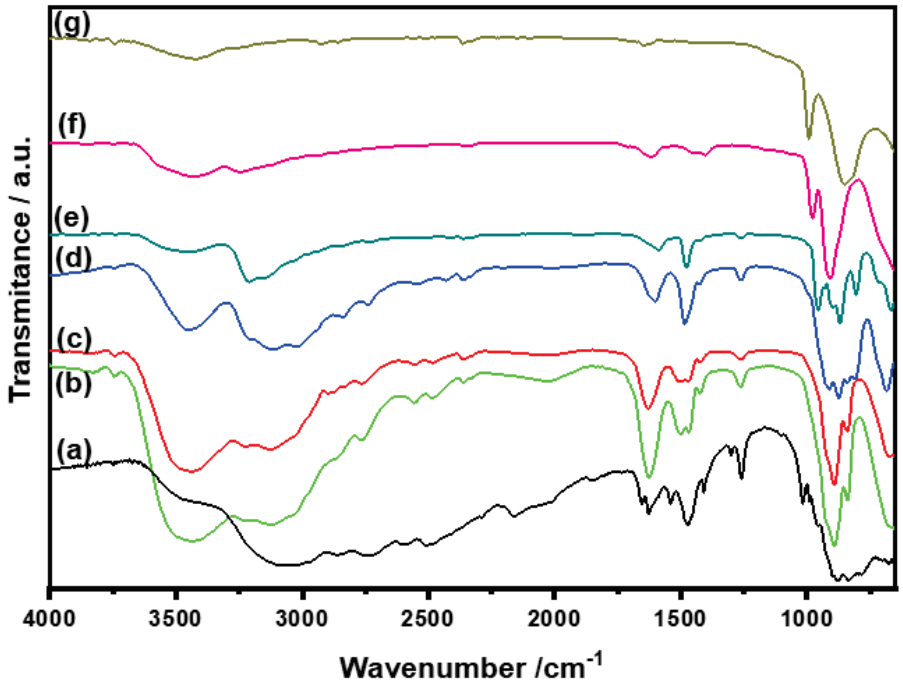

Figure 2.8. FT-IR spectra of (a) methylammonium monomolybdate, calcined at (b) 50, (c) 120, (d) 150, (e) 200, (f) 270, and (g) 350 °C.

Single-crystal X-ray diffraction analysis revealed that crystals comprising $[Mo_7O_{24}]^{6-}$ anion, $[MoO_4]^{2-}$ anion, four water molecules, and eight methylammonium cations to form $(CH_3NH_3)_8[Mo_7O_{24}\text{-}MoO_4]\cdot 4H_2O$ (Table 2.1). The $[Mo_7O_{24}]^{6-}$ anion is composed of seven condensed edge-sharing MoO_6 octahedra similar to reported heptamolybdate anion for ammonium and sodium salt.[26,27] This anion possesses a central Mo_3O_8 core composed of three edge-sharing MoO_6 octahedra; two MoO_6 units from above and two from below share the equatorial O atoms (Figure 2.10). The crystal structure contains co-crystallized monomolybdate $[MoO_4]^{2-}$ anion with tetrahedral geometry. Wutkowski et al. also reported a similar compound comprising $[Mo_7O_{24}]^{6-}$ and $[MoO_4]^{2-}$ with butan-1-ammonium ($BuNH_3$) counter cation.[28] Tables 2.6 and 2.7 list the bond distances and angles of heptamolybdate and monomolybdate anions. The Mo-O distances for heptamolybdate and monomolybdate anions are between 1.71 to 2.52 Å and 1.74 to 1.78 Å, respectively. O-Mo-O bond angles for heptamolybdate and monomolybdate anions range between 70.23 to 177.22° and

106.15 to 111.56°, respectively. The $[Mo_7O_{24}]^{6-}$ and $[MoO_4]^{2-}$ ions form hydrogen bonds with organic cations through N–H···O interactions (Figure 2.10).

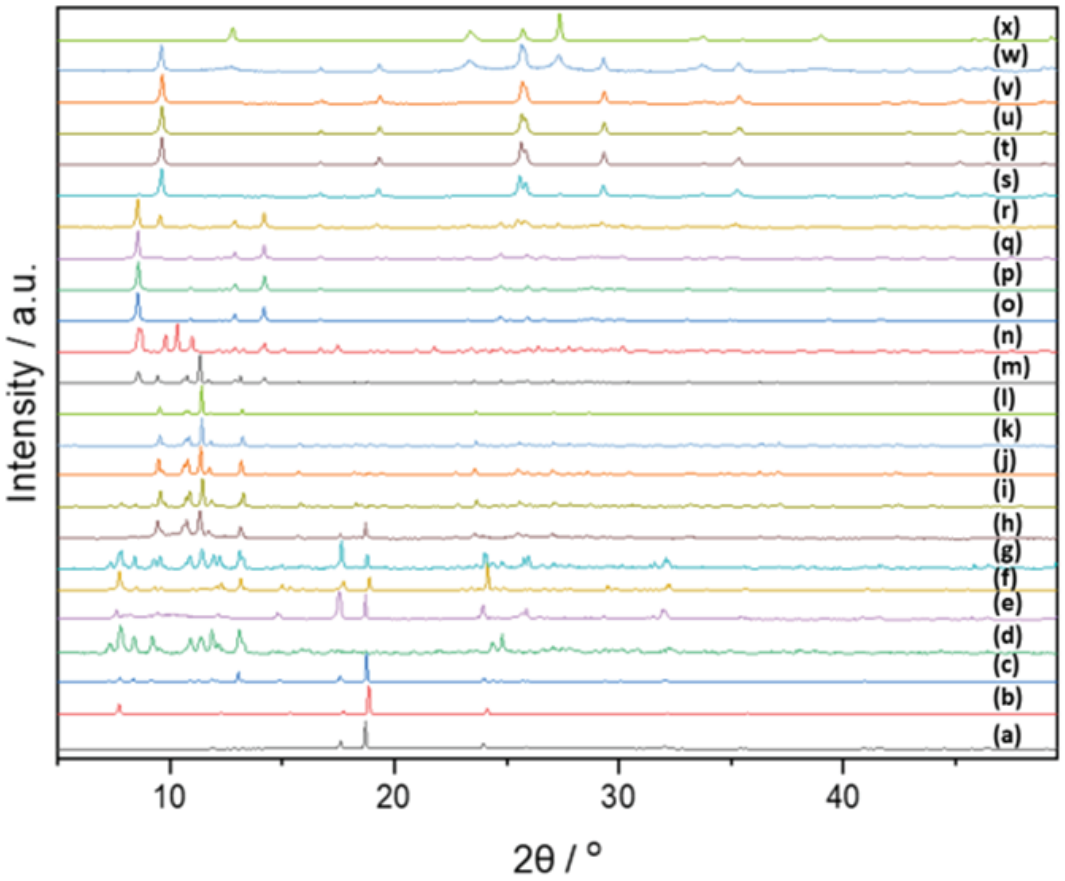

Figure 2.9. XRD patterns of (a) methylammonium monomolybdate, calcined at (b) 50 °C for 1h, (c) 50 °C for 2h, (d) 50 °C for 4h, (e) 60 °C for 1h, (f) 70 °C for 1h, (g) 80 °C for 1h, (h) 90 °C for 1h, (i) 100 °C for 1h,(j) 110 °C for 1h, (k) 120 °C for 1h, (l) 130 °C for 1h, (m) 140 °C for 1h, (n) 150 °C for 1h, (o) 180 °C for 1h, (p) 200 °C for 1h, (q) 240 °C for 1h, (r) 250 °C for 1h, (s) 260 °C for 1h, (t) 270 °C for 1h, (u) 280 °C for 1h, (v) 290 °C for 1h, (w) 300 °C for 1h, and (x) 350 °C for 1h.

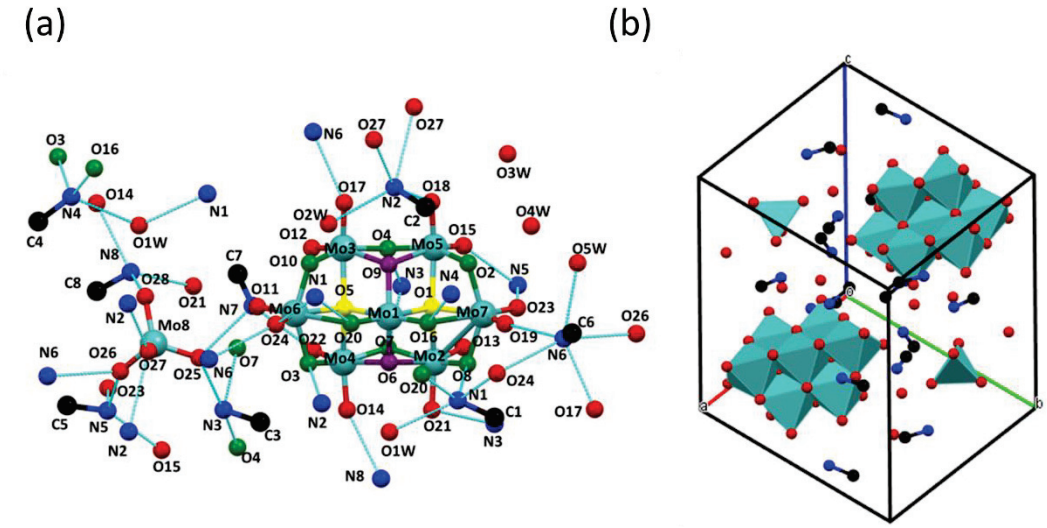

Figure 2.10. (a) Crystal structure and atom labeling for methylammonium heptamolybdate-monomolybdate and (b) packing of molecules in the crystal lattice. Hydrogen atoms are not shown for clarity. Light blue, red, green, purple, yellow, black, and blue balls represent molybdenum, terminal oxygen, twofold-coordinated oxygen, threefold-coordinated oxygen, fourfold-coordinated oxygen, carbon, and nitrogen atoms, respectively. Light blue lines represent hydrogen bonds between N and O atom which is shorter than 3.0 Å.

Table 2.6. Selected bond distance (Å) of methylammonium heptamolybdate-monolybdate

Bonds	Length (Å)	Bonds	Length (Å)
Mo1-O20	1.7424(14)	Mo4-O6	2.2571(14)
Mo1-O16	1.7474(14)	Mo5-O15	1.7197(14)
Mo1-O9	1.8836(13)	Mo5-O18	1.7225(14)
Mo1-O6	1.9054(14)	Mo5-O4	1.9584(14)
Mo1-O1	2.2511(13)	Mo5-O2	1.9687(14)
Mo1-O5	2.2779(14)	Mo5-O1	2.1603(13)
Mo2-O13	1.7154(15)	Mo5-O9	2.2592(13)
Mo2-O21	1.7351(14)	Mo6-O24	1.7291(15)
Mo2-O7	1.9522(14)	Mo6-O11	1.7293(15)
Mo2-O8	1.9538(14)	Mo6-O10	1.8943(14)
Mo2-O1	2.1718(13)	Mo6-O3	1.9445(14)
Mo2-O6	2.2583(14)	Mo6-O5	2.1488(13)
Mo3-O12	1.7160(15)	Mo6-O20	2.4892(14)
Mo3-O17	1.7293(14)	Mo7-O23	1.7111(15)
Mo3-O4	1.9166(14)	Mo7-O19	1.7277(15)
Mo3-O10	2.0070(14)	Mo7-O2	1.9258(14)
Mo3-O5	2.1556(13)	Mo7-O8	1.9322(14)
Mo3-O9	2.2562(14)	Mo7-O1	2.1592(14)

Mo4-O22	1.7159(15)	Mo7-O16	2.5198(14)
Mo4-O14	1.7243(15)	Mo8-O27	1.7370(15)
Mo4-O7	1.9346(14)	Mo8-O26	1.7525(17)
Mo4-O3	1.9957(14)	Mo8-O28	1.7695(16)
Mo4-O5	2.1552(13)	Mo8-O25	1.7854(15)

Table 2.7. Selected O-Mo-O angles (°) of methylammonium heptamolybdate-monomolybdate

Bonds	**Angle (°)**	**Bonds**	**Angle (°)**	**Bonds**	**Angle (°)**
O20-Mo1-O16	104.88(7)	O17-Mo3-O5	158.51(6)	O1-Mo5-O9	71.58(5)
O20-Mo1-O9	101.82(6)	O4-Mo3-O5	89.72(5)	O24-Mo6-O11	105.28(7)
O16-Mo1-O9	101.95(6)	O10-Mo3-O5	72.98(5)	O24-Mo6-O10	102.83(6)
O20-Mo1-O6	100.07(6)	O12-Mo3-O9	162.84(6)	O11-Mo6-O10	98.98(7)
O16-Mo1-O6	100.85(6)	O17-Mo3-O9	91.42(6)	O24-Mo6-O3	98.68(7)
O9-Mo1-O6	142.92(6)	O4-Mo3-O9	74.54(5)	O11-Mo6-O3	98.47(6)
O20-Mo1-O1	170.81(6)	O10-Mo3-O9	83.24(5)	O10-Mo6-O3	147.52(6)
O16-Mo1-O1	84.24(6)	O5-Mo3-O9	72.37(5)	O24-Mo6-O5	147.67(6)
O9-Mo1-O1	76.86(5)	O22-Mo4-O14	104.78(7)	O11-Mo6-O5	106.89(6)
O6-Mo1-O1	76.79(5)	O22-Mo4-O7	95.98(7)	O10-Mo6-O5	75.31(5)
O20-Mo1-O5	82.70(6)	O14-Mo4-O7	99.82(6)	O3-Mo6-O5	73.49(5)
O16-Mo1-O5	172.38(6)	O22-Mo4-O3	100.32(7)	O24-Mo6-O20	77.46(6)
O9-Mo1-O5	76.89(5)	O14-Mo4-O3	93.84(6)	O11-Mo6-O20	177.22(6)
O6-Mo1-O5	76.65(5)	O7-Mo4-O3	155.31(6)	O10-Mo6-O20	80.80(5)
O1-Mo1-O5	88.16(5)	O22-Mo4-O5	96.00(6)	O3-Mo6-O20	80.47(5)
O13-Mo2-O21	104.62(7)	O14-Mo4-O5	156.94(6)	O5-Mo6-O20	70.35(5)
O13-Mo2-O7	96.04(7)	O7-Mo4-O5	87.64(5)	O23-Mo7-O19	106.46(7)
O21-Mo2-O7	99.92(6)	O3-Mo4-O5	72.38(5)	O23-Mo7-O2	99.25(7)
O13-Mo2-O8	101.41(7)	O22-Mo4-O6	164.95(6)	O19-Mo7-O2	101.54(7)
O21-Mo2-O8	94.53(7)	O14-Mo4-O6	88.42(6)	O23-Mo7-O8	99.07(7)
O7-Mo2-O8	153.73(6)	O7-Mo4-O6	74.31(5)	O19-Mo7-O8	99.65(7)
O13-Mo2-O1	92.66(6)	O3-Mo4-O6	85.69(5)	O2-Mo7-O8	146.64(6)
O21-Mo2-O1	160.85(6)	O5-Mo4-O6	72.51(5)	O23-Mo7-O1	104.37(6)
O7-Mo2-O1	86.17(5)	O15-Mo5-O18	104.28(7)	O19-Mo7-O1	149.16(6)
O8-Mo2-O1	73.63(5)	O15-Mo5-O4	96.34(6)	O2-Mo7-O1	74.23(5)
O13-Mo2-O6	161.67(6)	O18-Mo5-O4	98.46(6)	O8-Mo7-O1	74.34(5)
O21-Mo2-O6	92.39(6)	O15-Mo5-O2	100.82(6)	O23-Mo7-O16	174.59(6)
O7-Mo2-O6	73.97(5)	O18-Mo5-O2	94.61(6)	O19-Mo7-O16	78.94(6)
O8-Mo2-O6	83.68(6)	O4-Mo5-O2	155.14(6)	O2-Mo7-O16	79.72(5)
O1-Mo2-O6	71.70(5)	O15-Mo5-O1	94.16(6)	O8-Mo7-O16	79.43(5)
O12-Mo3-O17	105.15(7)	O18-Mo5-O1	159.73(6)	O1-Mo7-O16	70.23(5)
O12-Mo3-O4	97.83(6)	O4-Mo5-O1	87.62(5)	O27-Mo8-O26	106.15(9)
O17-Mo3-O4	99.65(6)	O2-Mo5-O1	73.39(5)	O27-Mo8-O28	110.63(8)
O12-Mo3-O10	100.45(6)	O15-Mo5-O9	162.60(6)	O26-Mo8-O28	108.90(9)
O17-Mo3-O10	91.56(6)	O18-Mo5-O9	91.48(6)	O27-Mo8-O25	109.73(7)
O4-Mo3-O10	155.24(6)	O4-Mo5-O9	73.71(5)	O26-Mo8-O25	109.73(8)
O12-Mo3-O5	92.54(6)	O2-Mo5-O9	84.94(5)	O28-Mo8-O25	111.56(8)

Peak positions of the experimental powder XRD profiles were comparable to the simulated powder XRD pattern (Figure 2.11), showing that the powder had the same crystal structure and that the phase purity of bulk powder was excellent.

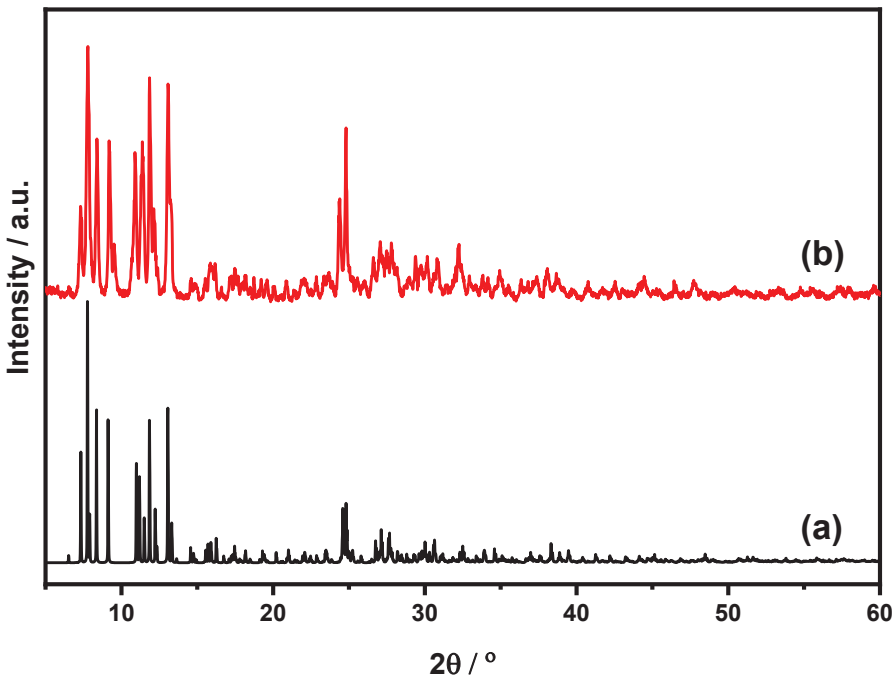

Figure 2.11. XRD patterns of methylammonium heptamolybdate-monomolybdate, $(CH_3NH_3)_8[Mo_7O_{24}\text{-}MoO_4]$, (a) simulated and (b) observed.

Figure 2.8(b) shows the FT-IR spectrum of methylammonium heptamolybdate-monomolybdate. The IR bands at 921, 892, and 840 cm^{-1} correspond to the stretching vibrations of Mo=O from the heptamolybdate anion. These peaks are similar to those characteristics of heptamolybdate anions.[29] Methylammonium heptamolybdate-monomolybdate exhibited strong Raman bands at 936, 909, and 885 cm^{-1}, which can be ascribed to the stretching vibration of Mo=O bond of $[Mo_7O_{24}]^{6-}$. The Raman bands at 863, 361, and 221 cm^{-1} correspond to the asymmetric Mo-O-Mo stretching mode, the Mo=O bending mode, and the Mo-O-Mo deformation mode, respectively (Figure 2.12(b)).[11]

The amount of weight loss estimated by TG-DTA and CHN elemental analysis are summarized in Table 2.4 together with the formula. Theoretical weight loss was comparable to observed weight losses, and CHN results were comparable to calculated CHN analysis data.

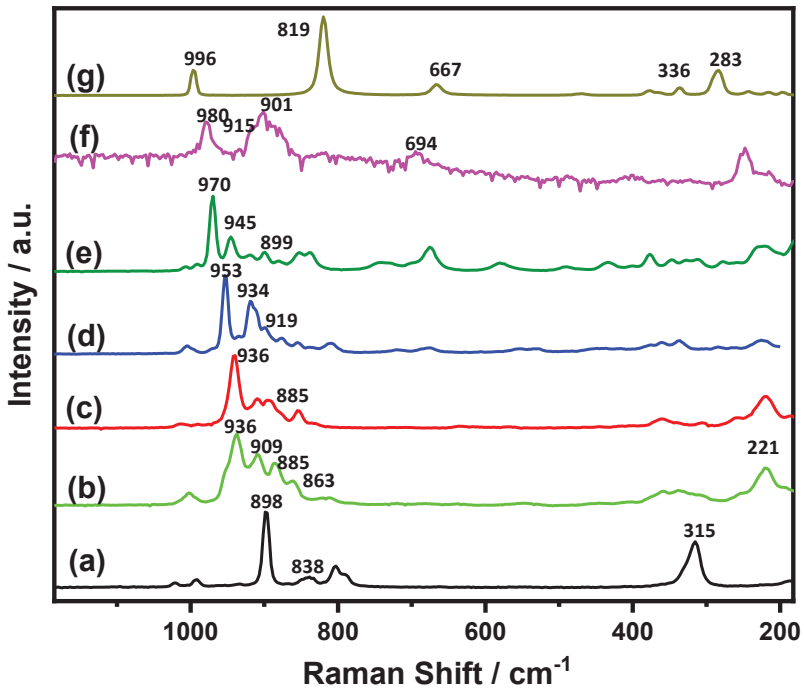

Figure 2.12. Raman spectra of (a) methylammonium monomolybdate, calcined at (b) 50, (c) 120, (d) 150, (e) 200, (f) 270, and (g) 350 °C.

2.3.2.3 Synthesis and characterization of $(CH_3NH_3)_6[Mo_7O_{24}]$

By heating at 120 °C for one hour, the second change was observed. Recrystallization was performed by dissolving the heated solid in water and then adding DMF. A single crystal X-ray structural analysis of the colorless crystal revealed that it contains heptamolybdate anion, $[Mo_7O_{24}]^{6-}$ and six methylammonium cations (Table 2.1). Similar to the heptamolybdate anions of the aforementioned methylammonium heptamolybdate-monomolybdate, the $[Mo_7O_{24}]^{6-}$ anion is composed of seven condensed, edge-sharing MoO_6 octahedra (Figure 2.13). The lengths of the Mo-O bonds and the angles of the O-Mo-O bonds for the $[Mo_7O_{24}]^{6-}$ anion are shown in Tables 2.8 and 2.9. The bond angles O-Mo-O are found to be between 70.11 and 174.81°, while the Mo-O distances are determined to be between 1.71 and 2.64 Å. The $[Mo_7O_{24}]^{6-}$ and $CH_3NH_3^+$ cations interact via hydrogen bonds in the crystal structure (Figure 2.13). Peak positions in the experimental powder XRD profiles matched one of the simulated powder XRD

patterns obtained from single-crystal X-ray data (Figure 2.14), indicating that the powder possessed the same crystal structure and high phase purity as the isolated solid. Furthermore, TG-DTA and CHN elemental analyses also confirmed the formula (Table 2.4).

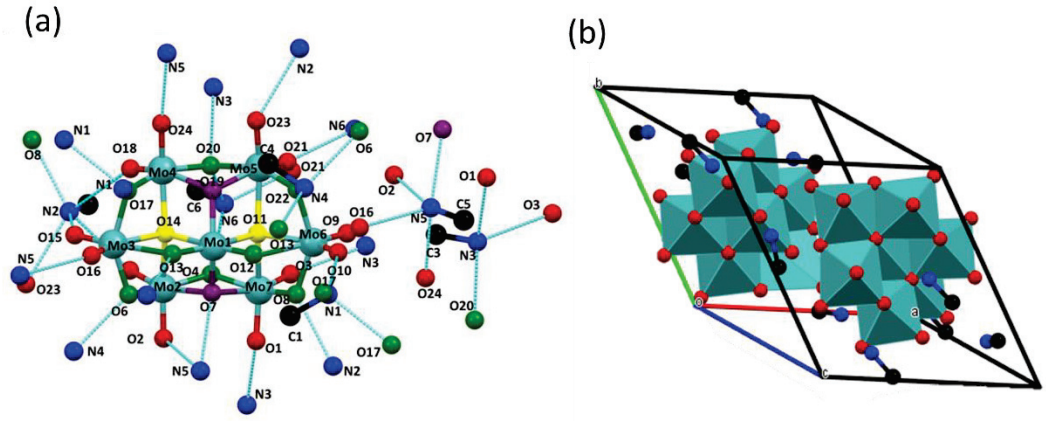

Figure 2.13. (a) Crystal structure and atom labeling for methylammonium heptamolybdate and (b) packing of molecules in the crystal lattice. Hydrogen atoms are not shown for clarity. Light blue, red, green, purple, yellow, black, and blue balls represent molybdenum, terminal oxygen, twofold coordinated oxygen, threefold coordinated oxygen, fourfold coordinated oxygen, carbon, and nitrogen atoms, respectively. Light blue lines represent hydrogen bonds between N and O atom which is shorter than 3.0 Å.

Table 2.8. Selected bond distance (Å) of methylammonium heptamolybdate

Bonds	Length (Å)	Bonds	Length (Å)
Mo1-O12	1.7282(15)	Mo4-O17	1.9995(15)
Mo1-O13	1.7563(15)	Mo4-O14	2.1557(14)
Mo1-O19	1.8993(14)	Mo4-O19	2.2865(15)
Mo1-O7	1.9090(15)	Mo5-O21	1.7163(16)
Mo1-O11	2.2516(14)	Mo5-O23	1.7216(15)
Mo1-O14	2.2723(14)	Mo5-O22	1.9060(15)
Mo2-O5	1.7112(15)	Mo5-O20	2.0094(15)
Mo2-O2	1.7122(15)	Mo5-O19	2.1625(15)
Mo2-O4	1.9410(15)	Mo5-O11	2.2734(14)
Mo2-O6	2.0009(15)	Mo6-O9	1.7125(16)
Mo2-O14	2.1687(14)	Mo6-O10	1.7248(15)
Mo2-O7	2.2925(15)	Mo6-O8	1.9199(15)
Mo3-O15	1.7108(15)	Mo6-O22	1.9454(15)
Mo3-O16	1.7451(15)	Mo6-O11	2.1272(14)
Mo3-O6	1.9015(15)	Mo6-O12	2.6390

Mo3-O17	1.9271(15)	Mo7-O3	1.7162(15)
Mo3-O14	2.1528(14)	Mo7-O1	1.7350(15)
Mo3-O13	2.4856(15)	Mo7-O4	1.9354(15)
Mo4-O18	1.7085(15)	Mo7-O8	1.9744(15)
Mo4-O24	1.7204(15)	Mo7-O11	2.1817(14)
Mo4-O20	1.9335(15)	Mo7-O7	2.2464(15)

Table 2.9. Selected O-Mo-O angles (°) of methylammonium heptamolybdate

Bonds	**Angle (°)**	**Bonds**	**Angle (°)**	**Bonds**	**Angle (°)**
O12-Mo1-O13	104.76(7)	O12-Mo1-O13	104.76(7)	O12-Mo1-O13	104.76(7)
O12-Mo1-O19	101.27(7)	O16-Mo3-O13	78.98(6)	O9-Mo6-O11	104.66(6)
O13-Mo1-O19	100.02(7)	O6-Mo3-O13	81.07(6)	O10-Mo6-O11	148.04(7)
O12-Mo1-O7	102.27(7)	O17-Mo3-O13	79.00(6)	O8-Mo6-O11	75.58(6)
O13-Mo1-O7	101.14(7)	O14-Mo3-O13	70.11(5)	O22-Mo6-O11	75.39(6)
O19-Mo1-O7	142.95(6)	O18-Mo4-O24	105.19(7)	O3-Mo7-O1	106.12(8)
O12-Mo1-O11	84.95(6)	O18-Mo4-O20	97.70(7)	O3-Mo7-O4	96.28(7)
O13-Mo1-O11	170.28(6)	O24-Mo4-O20	98.18(7)	O1-Mo7-O4	100.76(7)
O19-Mo1-O11	77.29(6)	O18-Mo4-O17	101.42(7)	O3-Mo7-O8	99.58(7)
O7-Mo1-O11	76.75(6)	O24-Mo4-O17	91.67(7)	O1-Mo7-O8	92.06(7)
O12-Mo1-O14	172.97(6)	O20-Mo4-O17	155.37(6)	O4-Mo7-O8	155.97(6)
O13-Mo1-O14	82.25(6)	O18-Mo4-O14	91.80(7)	O3-Mo7-O11	94.16(6)
O19-Mo1-O14	76.60(6)	O24-Mo4-O14	159.16(7)	O1-Mo7-O11	156.83(7)
O7-Mo1-O14	76.54(6)	O20-Mo4-O14	91.24(6)	O4-Mo7-O11	87.75(6)
O11-Mo1-O14	88.04(5)	O17-Mo4-O14	72.88(6)	O8-Mo7-O11	73.26(6)
O5-Mo2-O2	106.26(8)	O18-Mo4-O19	160.11(6)	O3-Mo7-O7	163.44(7)
O5-Mo2-O4	98.68(7)	O24-Mo4-O19	93.48(6)	O1-Mo7-O7	89.49(6)
O2-Mo2-O4	99.72(7)	O20-Mo4-O19	72.42(6)	O4-Mo7-O7	74.96(6)
O5-Mo2-O6	101.36(7)	O17-Mo4-O19	84.55(6)	O8-Mo7-O7	85.01(6)
O2-Mo2-O6	90.73(7)	O14-Mo4-O19	71.64(5)	O11-Mo7-O7	71.79(5)
O4-Mo2-O6	153.79(6)	O21-Mo5-O23	105.01(8)	Mo6-O11-Mo7	94.39(6)
O5-Mo2-O14	93.16(7)	O21-Mo5-O22	101.17(7)	Mo6-O11-Mo1	104.07(6)
O2-Mo2-O14	156.72(7)	O23-Mo5-O22	99.21(7)	Mo7-O11-Mo1	100.72(6)
O4-Mo2-O14	89.67(6)	O21-Mo5-O20	89.19(7)	Mo6-O11-Mo5	93.37(5)
O6-Mo2-O14	72.58(6)	O23-Mo5-O20	98.32(7)	Mo7-O11-Mo5	158.49(7)
O5-Mo2-O7	162.54(6)	O22-Mo5-O20	156.52(6)	Mo1-O11-Mo5	96.80(5)
O2-Mo2-O7	90.70(6)	O21-Mo5-O19	156.27(7)	Mo1-O13-Mo3	106.30(7)
O4-Mo2-O7	73.77(6)	O23-Mo5-O19	93.97(7)	Mo3-O14-Mo4	96.54(6)
O6-Mo2-O7	82.19(6)	O22-Mo5-O19	89.46(6)	Mo3-O14-Mo2	95.48(6)
O14-Mo2-O7	71.41(5)	O20-Mo5-O19	73.84(6)	Mo4-O14-Mo2	150.94(7)
O15-Mo3-O16	105.82(7)	O21-Mo5-O11	90.89(7)	Mo3-O14-Mo1	101.29(6)
O15-Mo3-O6	99.57(7)	O23-Mo5-O11	163.44(7)	Mo4-O14-Mo2	101.57(6)
O16-Mo3-O6	102.55(7)	O22-Mo5-O11	72.69(6)	Mo2-O14-Mo2	101.87(6)
O15-Mo3-O17	98.12(7)	O20-Mo5-O11	86.28(6)	Mo3-O17-Mo4	109.93(7)
O16-Mo3-O17	98.54(7)	O19-Mo5-O11	71.93(5)	Mo1-O19-Mo5	112.67(7)
O6-Mo3-O17	147.49(6)	O9-Mo6-O10	107.22(7)	Mo1-O19-Mo4	109.78(7)
O15-Mo3-O14	105.02(7)	O9-Mo6-O8	100.77(7)	Mo5-O19-Mo4	95.95(6)
O16-Mo3-O14	149.04(7)	O10-Mo6-O8	100.44(7)	Mo4-O20-Mo5	113.94(7)
O6-Mo3-O14	74.84(6)	O9-Mo6-O22	102.17(7)	Mo5-O22-Mo6	112.56(7)
O17-Mo3-O14	74.33(6)	O10-Mo6-O22	95.53(7)		

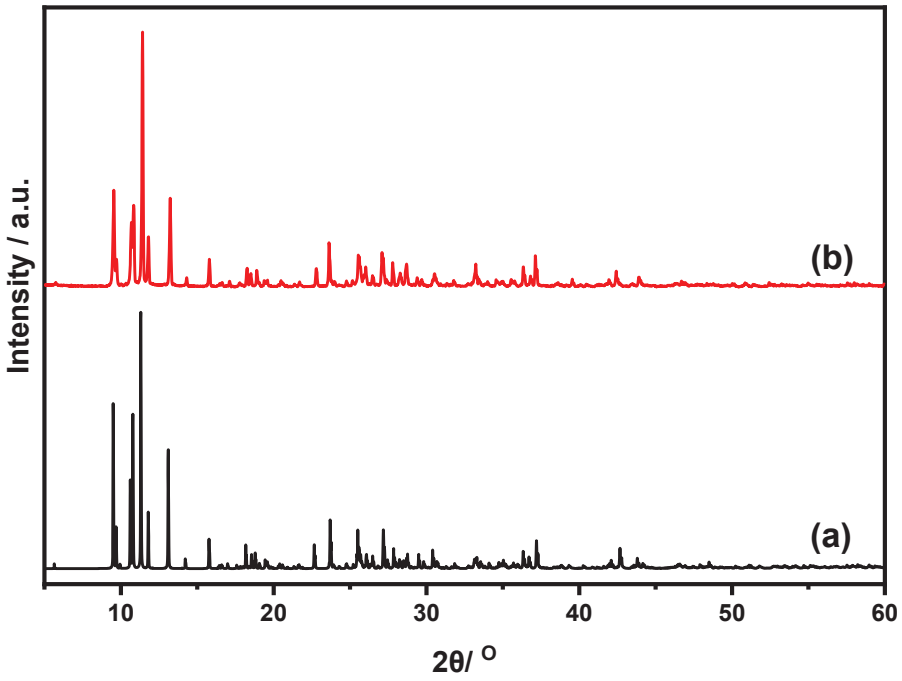

Figure 2.14. XRD patterns of methylammonium heptamolybdate, $(CH_3NH_3)_6[Mo_7O_{24}]$, (a) simulated and (b) observed.

Methylammonium heptamolybdate-monomolybdate and methylammonium heptamolybdate have comparable infrared spectra. The stretching vibrations of Mo=O from the heptamolybdate anion are shown by the IR bands at 921, 892, and 840 cm^{-1} (Figure 2.8(c)). The strong Raman bands at 936 and 885 cm^{-1} can be attributed to the asymmetric stretching vibration of the Mo=O bond in $[Mo_7O_{24}]^{6-}$ (Figure 2.12(c)). These results suggest that the previous paper's prediction about the structure of $(CH_3NH_3)_6[Mo_7O_{24}]$ was correct.[14]

2.3.2.4 Synthesis and characterization of $(CH_3NH_3)_8[Mo_{10}O_{34}]$

Heating at 150 °C for one hour allowed for the observation of the third transition (Figure 2.9(n)). Figure 2.15 shows that the XRD pattern of the heated solid was similar to the XRD simulated using single crystal structure analysis of methylammonium decamolybdate reported by Yamase et al.,[20] suggesting that the isolated solid is pure $(CH_3NH_3)_8[Mo_{10}O_{34}]\cdot 2H_2O$. Methylammonium decamolybdate crystallizes in the $P2_1/n$ space group. Two MoO_4 tetrahedra and the γ-Mo_8O_{26} unit make up the anion. Eight MoO_6 octahedra that were connected by

edge-sharing make up the γ-Mo_8O_{26}, which is then connected to a unit of MoO_4 tetrahedra via corner-sharing (Figure 2.16). In contrast to ammonium decamolybdate produced by heating ammonium heptamolybdate, methylammonium decamolybdate has a different linking mode of MoO_4 tetrahedra to the γ-Mo_8O_{26} unit. The MoO_4 units are found at the sites O13 in ammonium decamolybdate, whereas they are connected to the linking sites O14 in methylammonium decamolybdate (Figure 2.17). The bond angles O-Mo-O are found to be between 69.07 and 164.21°, while the Mo-O distances are found to be between 1.7 and 2.43 Å (Tables 2.10 and 2.11)The $[Mo_{10}O_{34}]^{8-}$ anions and $CH_3NH_3^+$ cations interact via hydrogen bonds in the crystal structure (Figure 2.16). The formula of solid was also confirmed by TG-DTA and CHN analysis (Table 2.4).

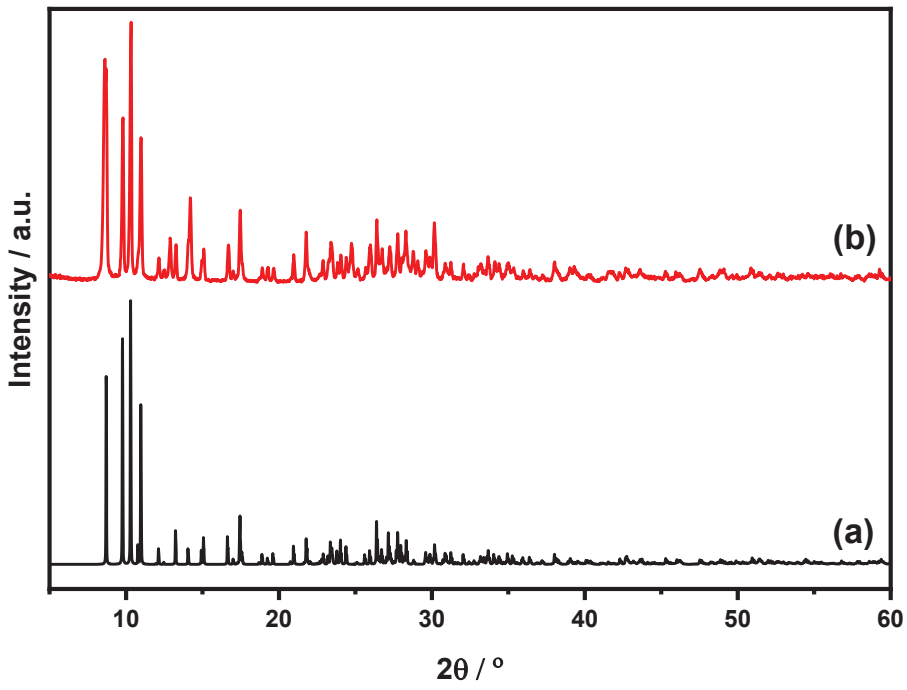

Figure 2.15. XRD patterns of methylammonium decamolybdate, $(CH_3NH_3)_8[Mo_{10}O_{34}]\cdot 2H_2O$, (a) simulated using single crystal structure analysis reported by Yamase et al.[20] and (b) observed.

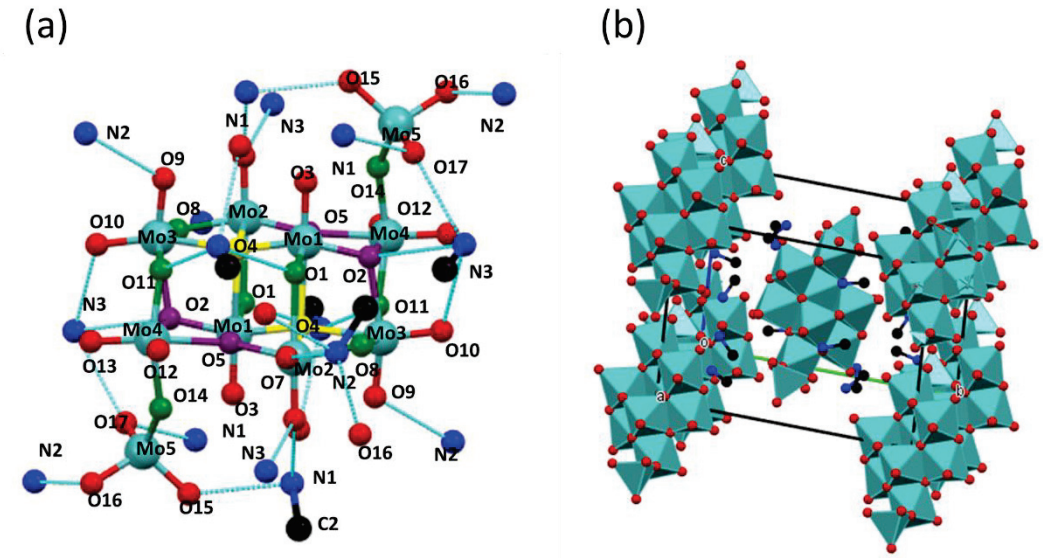

Figure 2.16. (a) Crystal structure and atom labeling for methylammonium decamolybdate and (b) packing of molecules in the crystal lattice. Hydrogen atoms are not shown for clarity. Light blue, red, green, purple, yellow, black, and blue balls represent molybdenum, terminal oxygen, twofold coordinated oxygen, threefold coordinated oxygen, fourfold coordinated oxygen, carbon, and nitrogen atoms, respectively. Light blue lines represent hydrogen bonds between N and O atom which is shorter than 3.0 Å.

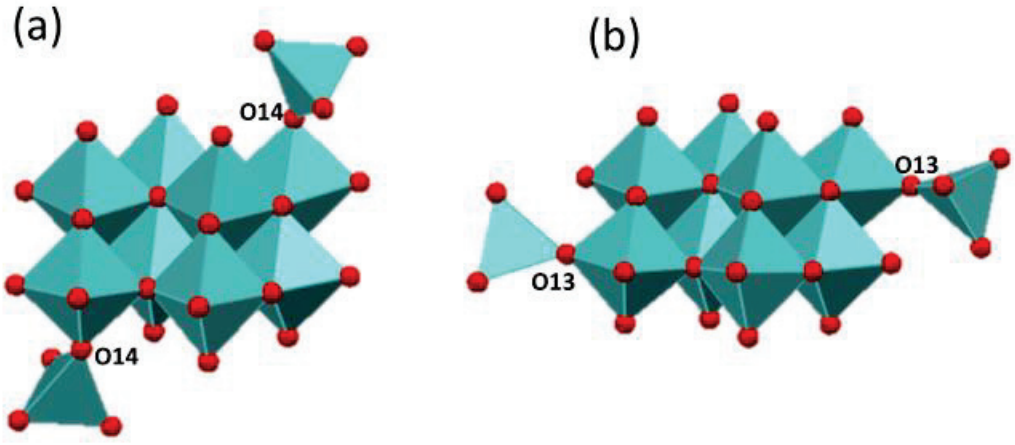

Figure 2.17. Polyhedral representation of $[Mo_{10}O_{34}]^{8-}$ anions of (a) methylammonium decamolybdate and (b) ammonium decamolybdate (ICSD 67325).

Table 10. Selected bond distance (Å) of methylammonium decamolybdate

Bonds	Length (Å)	Bonds	Length (Å)
Mo1-O3	1.699(2)	Mo3-O11	1.929(2)
Mo1-O1	1.765(2)	Mo3-O8	1.949(2)
Mo1-O2	1.864(2)	Mo3-O4	2.224(2)
Mo1-O4	1.955(2)	Mo3-O2	2.281(2)
Mo1-O5	2.137(2)	Mo4-O12	1.702(2)
Mo1-O4	2.426(2)	Mo4-O13	1.713(2)
Mo2-O7	1.721(2)	Mo4-O11	1.916(2)
Mo2-O6	1.724(2)	Mo4-O14	2.022(2)
Mo2-O8	1.903(2)	Mo4-O5	2.163(2)
Mo2-O5	1.908(2)	Mo4-O2	2.270(2)
Mo2-O4	2.230(2)	Mo5-O16	1.745(2)
Mo2-O1	2.340(2)	Mo5-O15	1.747(2)
Mo3-O10	1.714(2)	Mo5-O17	1.756(2)
Mo3-O9	1.723(2)	Mo5-O14	1.813(2)

Table 2.11. Selected O-Mo-O angles (°) of methylammonium decamolybdate

Bonds	Angle (°)	Bonds	Angle (°)	Bonds	Angle (°)
O3-Mo1-O1	104.30(10)	O6-Mo2-O4	100.11(9)	O4-Mo3-O2	73.61(7)
O3-Mo1-O2	103.93(9)	O8-Mo2-O4	73.52(8)	O12-Mo4-O13	105.95(10)
O1-Mo1-O2	100.65(9)	O5-Mo2-O4	72.00(8)	O12-Mo4-O11	99.03(10)
O3-Mo1-O4	102.52(9)	O7-Mo2-O1	85.33(9)	O13-Mo4-O11	99.34(10)
O1-Mo1-O4	97.48(9)	O6-Mo2-O1	171.63(9)	O12-Mo4-O14	97.99(10)
O2-Mo1-O4	142.90(9)	O8-Mo2-O1	79.28(8)	O13-Mo4-O14	90.99(10)
O3-Mo1-O5	98.33(9)	O5-Mo2-O1	79.88(8)	O11-Mo4-O14	156.79(8)
O1-Mo1-O5	156.99(9)	O4-Mo2-O1	71.62(7)	O12-Mo4-O5	93.71(9)
O2-Mo1-O5	77.55(8)	O10-Mo3-O9	105.33(10)	O13-Mo4-O5	158.63(9)
O4-Mo1-O5	73.26(8)	O10-Mo3-O11	99.98(9)	O11-Mo4-O5	85.46(8)
O3-Mo1-O4	177.80(8)	O9-Mo3-O11	97.13(9)	O14-Mo4-O5	77.80(8)
O1-Mo1-O4	77.55(8)	O10-Mo3-O8	94.96(9)	O12-Mo4-O2	161.81(9)
O2-Mo1-O4	76.74(8)	O9-Mo3-O8	101.19(9)	O13-Mo4-O2	91.99(9)
O4-Mo1-O4	75.97(8)	O11-Mo3-O8	152.35(9)	O11-Mo4-O2	74.58(8)
O5-Mo1-O4	79.74(7)	O10-Mo3-O4	159.87(9)	O14-Mo4-O2	84.40(8)
O7-Mo2-O6	102.97(10)	O9-Mo3-O4	92.94(9)	O5-Mo4-O2	69.07(7)
O7-Mo2-O8	104.24(9)	O11-Mo3-O4	85.79(8)	O16-Mo5-O15	107.54(10)
O6-Mo2-O8	97.38(9)	O8-Mo3-O4	72.83(8)	O16-Mo5-O17	106.91(10)
O7-Mo2-O5	103.13(9)	O10-Mo3-O2	89.32(9)	O15-Mo5-O17	110.13(10)
O6-Mo2-O5	99.02(9)	O9-Mo3-O2	164.21(9)	O16-Mo5-O14	108.22(10)
O8-Mo2-O5	143.84(9)	O11-Mo3-O2	74.10(8)	O15-Mo5-O14	111.09(10)
O7-Mo2-O4	156.90(9)	O8-Mo3-O2	83.01(8)	O17-Mo5-O14	112.71(10)

According to Figure 2.12(d), the Raman band at 1005 cm^{-1} can be attributed to the C-N stretching of counter-cation methylammonium. This band supports the IR result that the methylammonium band could still be detected, indicating that heating at 150 °C did not completely remove all methylammonium. The typical Raman bands of decamolybdate anion were found at 953, 934, 919, 899, 876, 854, and 675

cm^{-1}. The Mo=O bond of decamolybdate's stretching vibrations are responsible for the strong band at 953 cm^{-1}.[11]

2.3.2.5 Synthesis and characterization of $(CH_3NH_3)_4[Mo_8O_{26}]$

At 200 °C, the fourth transformation was observed (Figure 2.9(p)). From database searches, we were unable to find any powder XRD that was similar. All of our attempts to create single crystals from the crystallization of heated solid were unsuccessful. According to an elemental analysis (Table 2.4), the material comprises four methylammonium cations and one $[Mo_8O_{26}]^{4-}$ anion. The formation of $[Mo_8O_{26}]^{4-}$ molecules in aqueous solutions with pH values between 2 and 6 has been reported.[7] We used screening to obtain single crystals from aqueous solutions where the pH of the $(CH_3NH_3)_2[MoO_4]$ aqueous solutions was varied between 1 and 6 using 1 M of H_2SO_4. We were lucky to be able to get a single crystal from an aqueous solution with a pH of 4 that was suitable for single crystal structure analysis, and the simulated powder XRD pattern generated from the results of this study matched the actual powder XRD pattern (Figure 2.18).

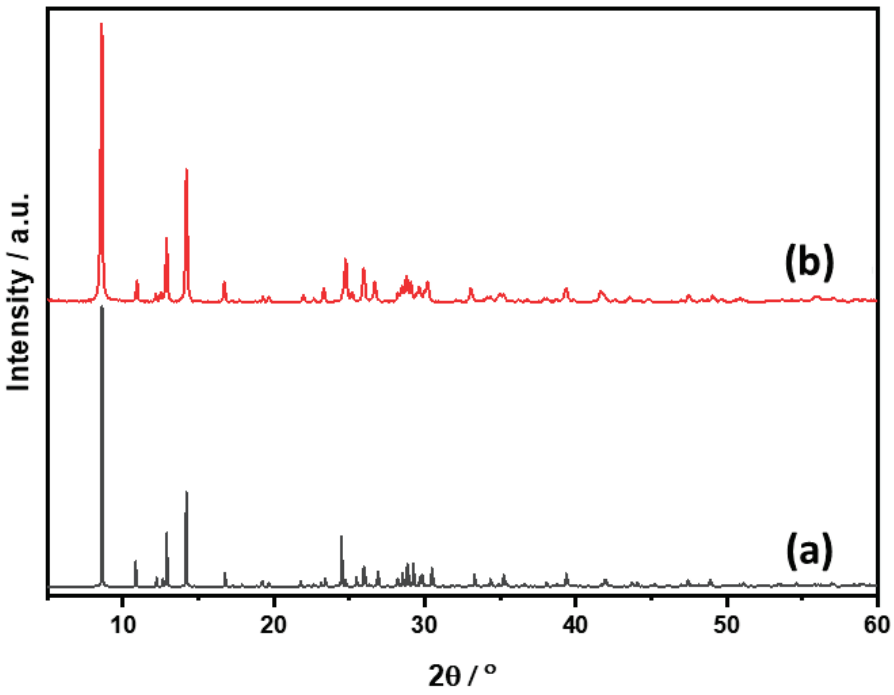

Figure 2.18. XRD patterns of methylammonium octamolybdate, $(CH_3NH_3)_4[Mo_8O_{26}]$, (a) simulated and (b) observed.

A single crystal X-ray structural investigation of the colorless crystal indicated that the crystal comprises gamma-type octamolybdate, $[\gamma\text{-}Mo_8O_{26}]^{4-}$ anion, and four methylammonium cations (Table 2.1). Eight distorted MoO_6 octahedra joined by edge-sharing made up the octamolybdate anion (Figure 2.19). The $[\gamma\text{-}Mo_8O_{26}]^{4-}$ anion created one-dimensional chains by two corner sharing oxygens (O7 in Figure 2.19). A similar one-dimensional structure has been reported for $(C_6H_{18}N_2)_2[\gamma\text{-}Mo_8O_{26}]$.[30] Although heating of ammonium heptamolybdate produced ammonium octamolybdate, the connecting mode was different. In the latter compound, $[\gamma\text{-}Mo_8O_{26}]^{4-}$ are connected through edge-sharing (Figure 2.20). The Mo-O bond lengths and O-Mo-O bond angles of $[Mo_8O_{26}]^{4-}$ anion are shown in Tables 2.12 and 2.13. The bond angles O-Mo-O are found to be between 70.63 and 175.68°, while the Mo-O distances are found to be between 1.68 and 2.36 Å. The $[Mo_8O_{26}]^{4-}$ anions and $CH_3NH_3^+$ cations interact via hydrogen bonds in the crystal structure (Figure 2.19).

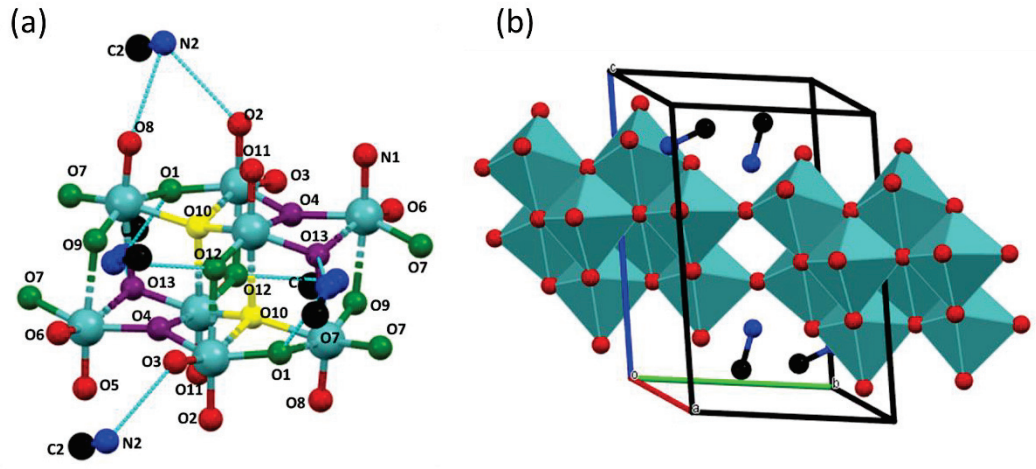

Figure 2.19. (a) Crystal structure and atom labeling for methylammonium octamolybdate and (b) packing of molecules in the crystal lattice. Hydrogen atoms are not shown for clarity. Light blue, red, green, purple, yellow, black, and blue balls represent molybdenum, terminal oxygen, twofold coordinated oxygen, threefold coordinated oxygen, fourfold coordinated oxygen, carbon, and nitrogen atoms, respectively. Light blue lines represent hydrogen bonds between N and O atom which is shorter than 3.0 Å.

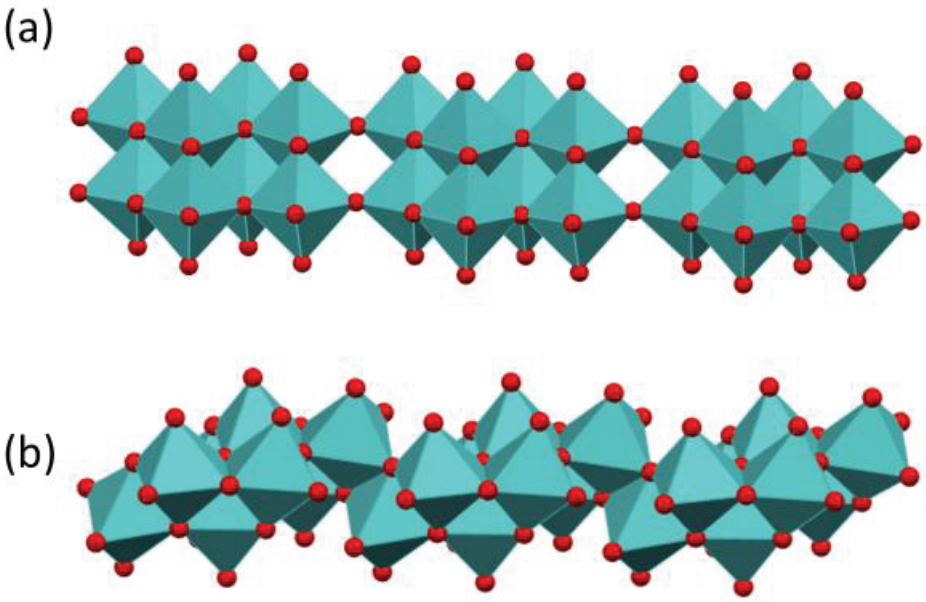

Figure 2.20. Polyhedral representation of octamolybdates chains of (a) methylammonium octamolybdate and (b) ammonium octamolybdate (ICSD 68562). Blue polyhedra represent [MoO_6] octahedra.

Table 2.12. Selected bond distance (Å) of methylammonium octamolybdate

Bonds	Length (Å)	Bonds	Length (Å)
Mo1-O3	1.713(3)	Mo3-O8	1.684(3)
Mo1-O2	1.717(3)	Mo3-O9	1.771(3)
Mo1-O1	1.857(3)	Mo3-O7	1.854(3)
Mo1-O4	1.998(3)	Mo3-O10	2.073(3)
Mo1-O10	2.256(3)	Mo3-O1	2.096(3)
Mo1-O12	2.365(3)	Mo3-O13	2.371(3)
Mo2-O5	1.703(3)	Mo4-O11	1.686(3)
Mo2-O6	1.704(3)	Mo4-O12	1.759(3)
Mo2-O7	1.918(3)	Mo4-O13	1.862(3)
Mo2-O4	1.986(3)	Mo4-O10	1.984(3)
Mo2-O13	2.200(3)	Mo4-O4	2.168(3)
Mo2-O9	2.327(3)	Mo4-O10	2.449(3)

Table 2.13. Selected O-Mo-O angles (°) of Methylammonium octamolybdate

Bonds	Angle (°)	Bonds	Angle (°)
O3-Mo1-O2	105.10(13)	O8-Mo3-O9	104.50(12)
O3-Mo1-O1	107.09(12)	O8-Mo3-O7	103.52(12)
O2-Mo1-O1	100.14(12)	O9-Mo3-O7	101.80(11)
O3-Mo1-O4	101.02(12)	O8-Mo3-O10	95.61(12)
O2-Mo1-O4	95.75(12)	O9-Mo3-O10	92.96(11)
O1-Mo1-O4	142.57(11)	O7-Mo3-O10	151.89(11)
O3-Mo1-O10	155.41(11)	O8-Mo3-O1	97.92(12)

O2-Mo1-O10	98.83(11)	O9-Mo3-O1	154.71(11)
O1-Mo1-O10	73.56(10)	O7-Mo3-O1	83.88(11)
O4-Mo1-O10	70.63(10)	O10-Mo3-O1	73.11(10)
O3-Mo1-O12	84.45(11)	O8-Mo3-O13	169.37(11)
O2-Mo1-O12	169.54(11)	O9-Mo3-O13	77.33(10)
O1-Mo1-O12	80.69(10)	O7-Mo3-O13	86.16(10)
O4-Mo1-O12	77.94(10)	O10-Mo3-O13	73.79(10)
O10-Mo1-O12	71.30(9)	O1-Mo3-O13	78.51(9)
O5-Mo2-O6	104.82(14)	O11-Mo4-O12	106.54(12)
O5-Mo2-O7	99.42(12)	O11-Mo4-O13	103.78(12)
O6-Mo2-O7	100.71(12)	O12-Mo4-O13	102.53(12)
O5-Mo2-O4	96.26(12)	O11-Mo4-O10	103.05(12)
O6-Mo2-O4	97.00(12)	O12-Mo4-O10	97.31(11)
O7-Mo2-O4	154.41(11)	O13-Mo4-O10	140.22(11)
O5-Mo2-O13	99.63(12)	O11-Mo4-O4	97.00(11)
O6-Mo2-O13	154.26(12)	O12-Mo4-O4	156.08(11)
O7-Mo2-O13	82.89(10)	O13-Mo4-O4	75.24(10)
O4-Mo2-O13	72.17(10)	O10-Mo4-O4	72.80(10)
O5-Mo2-O9	170.59(11)	O11-Mo4-O10	175.68(11)
O6-Mo2-O9	84.49(11)	O12-Mo4-O10	77.75(10)
O7-Mo2-O9	79.84(10)	O13-Mo4-O10	75.48(10)
O4-Mo2-O9	81.00(10)	O10-Mo4-O10	75.56(11)
O13-Mo2-O9	70.96(9)	O4-Mo4-O10	78.68(9)

Bands at 970, 945, 918, 899, and 839 cm^{-1} were observed in the Raman spectra (Figure 4,12(e)), and bands at 954, 931, 896, 869, 806, 715, and 667 cm^{-1} were seen in the IR spectrum (Figure 2.8(e)). The Raman and IR bands of C-N stretching from methylammonium are still observed, indicating the presence of methylammonium.

2.3.2.6 Further heating to hexagonal-MoO_3 and orthorhombic-MoO_3

Methylammonium was again released in the fifth transformation at 270 °C. According to Figures 2.9(t) and 2.21, the crystal was determined to be a hexagonal-MoO_3 phase (ICDD 21-0569). In accordance with the stretching mode of the Mo=O bond, the characteristic IR bands of hexagonal MoO_3 were found at 977 and 908 cm^{-1} (Figure 2.8(f)).[31] Low-intensity of IR bands from methylammonium and water were observed. The calcined solid at 270 C exhibited Raman bands at 980, 915, 901, and 880 cm^{-1} due to the Mo=O bond, but the band at 694 cm^{-1} can be attributed to O-Mo-O vibrations (Figure 2.12(f)).[32] These bands indicate the formation of hexagonal MoO_3 at 270 °C.

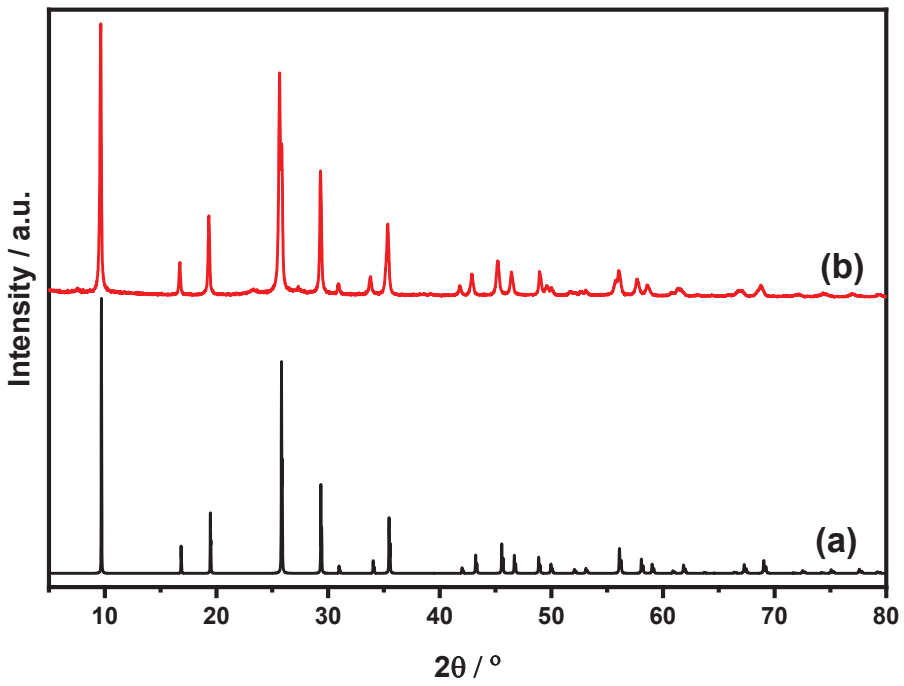

Figure 2.21. XRD patterns of hexagonal MoO_3, (a) simulated of ICDD 21-0569 and (b) observed.

The final transformation, from hexagonal MoO_3 to orthorhombic-MoO_3 (ICDD 12-8070), was observed at 350 °C (Figure 2.9(x) and 2.22). Solid was completely free of water and methylammonium. This is evident in the IR spectrum, which lacks the characteristic bands of either molecule (Figure 2.8(g)). The FT-IR spectrum of a heated solid at 350 °C reveals characteristic bands of orthorhombic MoO_3 at 850 and 993 cm^{-1}, which can be attributed to the stretching modes of Mo-O-Mo and Mo=O terminal oxygen, respectively.[33] Raman spectroscopy also supported the formation of the orthorhombic-MoO_3 phase. Figure 2.12(g) shows the oxygen-molybdenum stretching vibrations of the terminal Mo=O, the doubly linked bridge oxygen Mo-O-Mo, and the three-coordinated edge OMo_3 at 996, 819, and 667 cm^{-1}, respectively. The oxygen-molybdenum bending vibrations of the terminal Mo=O, the doubly linked bridge oxygen Mo-O-Mo, and the three-coordinated edge OMo_3 are responsible for the bands at 283, 219, and 336 cm^{-1}, respectively.[34]

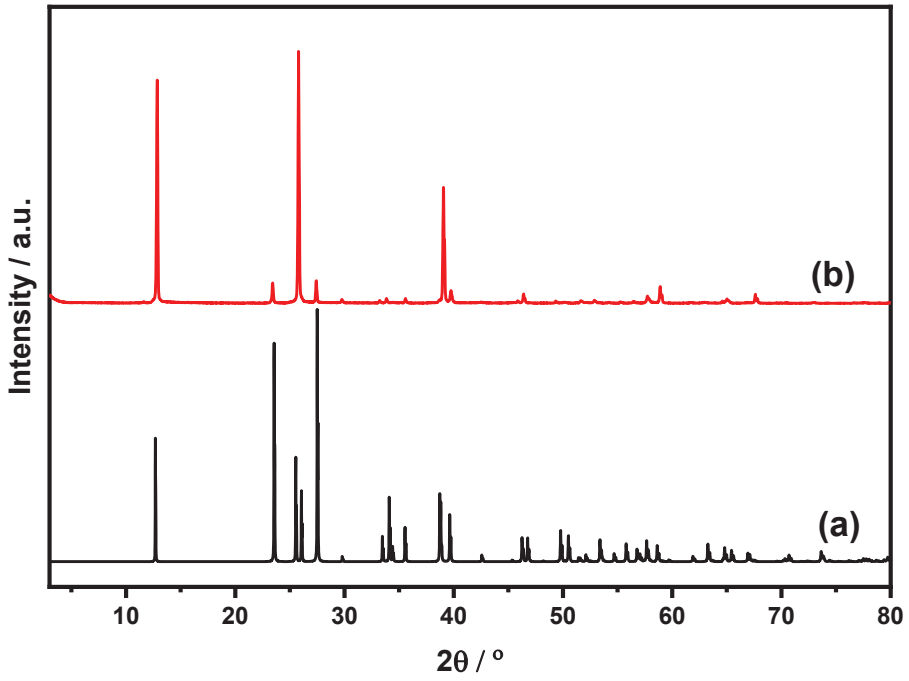

Figure 2.22. XRD patterns of orthorhombic MoO_3, (a) simulated of ICDD 12-8070 and (b) observed.

According to the results, we observed that $(CH_3NH_3)_2[MoO_4]$ transformed into $(CH_3NH_3)_8[Mo_7O_{24}\text{-}MoO_4]$ and $(CH_3NH_3)_6[Mo_7O_{24}]$ at 50 and 120 °C, respectively. In solution, $[MoO_4]^{2-}$ is reported to be converted into either $[Mo_2O_7]^{2-}$ or $[Mo_7O_{24}\text{-}MoO_4]^{8-}$ depending on the type of counter cations and solvents.[35] NH_4^+ preferred the formation of $((NH_4)_2[Mo_3O_{10}]$ and $(NH_4)_2[Mo_2O_7]$, $CH_3NH_3^+$ preferred the formation of $(CH_3NH_3)_8[Mo_7O_{24}\text{-}MoO_4]$ and $(CH_3NH_3)_6[Mo_7O_{24}]$. Szilágyi's group reported that by heating $(NH_4)_2[MoO_4]$ at 205, 230, and 370°C in air, the compound was transformed into a combination of $(NH_4)_2[Mo_3O_{10}]$ and $(NH_4)_2[Mo_2O_7]$, $(NH_4)_2[Mo_4O_{13}]$, and orthorhombic MoO_3, respectively.[10] Ressler's group has reported that the structure of $(NH_4)_2[Mo_4O_{13}]$ is identical to that of $(NH_4)_4[Mo_8O_{26}]$, in which γ-type octamolybdates are linked to one another via edge-sharing.[29]

Heating of $(CH_3NH_3)_6[Mo_7O_{24}]$ at 150 °C led to the formation of $(CH_3NH_3)_8[Mo_{10}O_{34}]$. Similarly with that, $(NH_4)_8[Mo_{10}O_{34}]$ was formed by heating

$(NH_4)_6[Mo_7O_{24}]$ in air between 100 and 200 °C.[10] The decamolybdate anion, $[Mo_{10}O_{34}]^{8-}$, of $(CH_3NH_3)_8[Mo_{10}O_{34}]$ and $(NH_4)_8[Mo_{10}O_{34}]$ has a similar structure in which two $[MoO_4]^{2-}$ tetrahedra were corner-shared with one γ-octamolybdate, $[Mo_8O_{26}]^{4-}$. As previously mentioned, the difference was in the mode of connection between MoO_4 tetrahedra and the octamolybdate unit.

Further heating at 200 °C, $(CH_3NH_3)_8[Mo_{10}O_{34}]$ transformed to $(CH_3NH_3)_4[Mo_8O_{26}]$. The octamolybdates, $[Mo_8O_{26}]^{4-}$ in the $(CH_3NH_3)_4[Mo_8O_{26}]$ were linked by two corner-sharing to create a one-dimensional chain. However, the $(NH_4)_4[Mo_8O_{26}]$ generated by heating $(NH_4)_6[Mo_7O_{24}]$ between 200 and 275 °C is a one-dimensional molecule in which octamolybdates, $[Mo_8O_{26}]^{4-}$ are joined via edge-sharing. Similar to the solid-state transformation of ammonium polyoxomolybdates, further heating formed hexagonal-MoO_3 and orthorhombic MoO_3.

According to some reports, the differences in the solid-state thermal transformation of $(CH_3NH_3)_2[MoO_4]$ and $(NH_4)_2[MoO_4]$ might be affected by type and size of the counter cation.[7,9] The structure of methylammonium isopolyoxomolybdate was changed by the release of methylamine and water molecules during heating. Additionally, differences in basicity (pKb of CH_3NH_2 and NH_3 is 3.34 and 4.75, respectively) and boiling point of base (−6.3 And −33.3 °C for CH_3NH_2 and NH_3, respectively) may have an influence on the formation temperature and polyoxometalates that are produced.

2.4 Conclusions

Methylammonium monomolybdate, $(CH_3NH_3)_2[MoO_4]$, was synthesized by dissolving MoO_3 in an aqueous methylamine solution with a CH_3NH_2/Mo ratio of 4 and then adding N,N-dimethylformamide. The compound was made up of two methylammonium counter-cations and one monomeric $[MoO_4]^{2-}$. It crystallized in the *Pnma* space group. Solid-state heating of $(CH_3NH_3)_2[MoO_4]$ in air released water and methylammonium, which led to the formation of several methylammonium isopolymolybdates, such as $(CH_3NH_3)_8[Mo_7O_{24}\text{-}MoO_4]$, $(CH_3NH_3)_6[Mo_7O_{24}]$, $(CH_3NH_3)_8[Mo_{10}O_{34}]$, and $(CH_3NH_3)_4[Mo_8O_{26}]$, and

molybdenum oxides such as hexagonal MoO_3 and orthorhombic MoO_3 which were confirmed by single crystal XRD, powder XRD, IR, Raman, and elemental analysis. Some of the structures of formed polyoxomolybdates were different from those of the molybdates made from ammonium.

References

1. D. S. Kharitonov, M. Zimowska, J. Ryl, A. Zieliński, M. A. Osipenko, J. Adamiec, A. Wrzesińska, P. M. Claesson, I. I. Kurilo, *Corros. Sci.* **2021**, *190*, 109664.
2. I. A. W. Ma, S. Ammar, S. S. A. Kumar, K. Ramesh, S. Ramesh, *J. Coat. Technol. Res* **2022**, *19*, 241–268.
3. L. Zhang, S. Zheng, L. Wang, H. Tang, H. Xue, G. Wang, *Small* **2017**, *13*, 1700917.
4. H. Yanagie, A. Ogata, S. Mitsui, T. Hisa, T. Yamase, M. Eriguchi, *Biomed. Pharmacother.* **2006**, *60*, 349–352.
5. I. A. De Castro, R. S. Datta, J. Z. Ou, A. Castellanos-gomez, S. Sriram, T. Daeneke, K. Kalantar-zadeh, *Adv. Mater.* **2017**, *29*, 1701619.
6. K. H. Kang, G. T. Kim, S. Park, P. W. Seo, H. Seo, C. W. Lee, *J. Ind. Eng. Chem.* **2019**, *76*, 1–16.
7. N. I. Gumerova, A. Rompel, *Chem. Soc. Rev.* **2020**, *49*, 7568–7601.
8. M. T. Pope, *Heteropoly and Isopoly Oxometalates*, Springer-Verlag, Berlin, **1983**.
9. S. Himeno, H. Niiya, T. Ueda, *Bull. Chem. Soc. Jpn.* **1997**, *70*, 631–637.
10. T. N. Kovács, D. Hunyadi, A. L. A. de Lucena, I. M. Szilágyi, *J. Therm. Anal. Calorim.* **2016**, *124*, 1013–1021.
11. Y. T. Kim, E. D. Park, *Appl.Catal. A Gen.* **2009**, *361*, 26–31.
12. N. C. Sukmana, J. Shinogi, A. Yamamoto, A. Higashiura, T. Sakaguchi, M. Sadakane, *Eur. J. Inorg. Chem.* **2022**, e202200322.
13. N. C. Sukmana, Sugiarto, Z. Zhang, M. Sadakane, *Z. Anorg. Allg. Chem.* **2021**, *647*, 1930–1937.
14. S. Ishikawa, T. Murayama, S. Ohmura, M. Sadakane, W. Ueda, *Chem.*

Mater. **2013**, *25*, 2211–2219.

15. S. Ishikawa, Y. Yamada, C. Qiu, Y. Kawahara, N. Hiyoshi, A. Yoshida, W. Ueda, *Chem. Mater.* **2019**, *31*, 1408–1417.
16. Bruker, *APEX3, SADAB5, SAINT*, **2016**.
17. G. M. Sheldrick, *Acta Crystallogr., Sect. A Found. Crystallogr* **2008**, *64*, 112–122.
18. G. M. Sheldrick, *Acta Crystallogr., Sect. C Struct. Chem.* **2015**, *71*, 3–8.
19. C. B. Hübschle, G. M. Sheldrick, B. Dittrich, *J. Appl. Crystallogr.* **2011**, *44*, 1281–1284.
20. P. K. Bharadwaj, Y. Ohashi, Y. Sasada, Y. Sasaki, T. Yamase, *Acta Crystallogr., Sect. C Struct. Chem.* **1986**, *42*, 545–547.
21. B. M. Gatehouse, P. Laverett, *J. Chem. Soc. A* **1969**, 849–854.
22. M. Dittmann, E. Schweda, *Z. Anorg. Allg. Chem.* **1998**, *624*, 2033–2037.
23. S. Vilminot, G. André, M. Richard-Plouet, F. Bourée-Vigneron, M. Kurmoo, *Inorg. Chem.* **2006**, *45*, 10938–10946.
24. V. P. M. Pillai, T. Pradeep, M. J. Bushiri, R. S. Jayasree, V. U. Nayar, *Spectrochim. Acta A Mol. Biomol. Spectrosc.* **1997**, *53*, 867–876.
25. T. Ozeki, H. Kihara, S. Ikeda, *Anal. Chem.* **1988**, *60*, 2055–2059.
26. K. Sjoböm, B. Hedman, *Acta Chem. Scand.* **1973**, *27*, 3673–3691.
27. E. Shimao, *Nature* **1967**, *214*, 170–171.
28. A. Wutkowski, B. R. Srinivasan, A. R. Naik, C. Schütt, C. Näther, W. Bensch, *Eur. J. Inorg. Chem.* **2011**, 2254–2263.
29. J. Wienold, R. E. Jentoft, T. Ressler, *Eur. J. Inorg. Chem.* **2003**, 1058–1071.
30. D. J. Hubbard, A. R. Johnston, H. S. Casalongue, A. N. Sarjeant, A. J. Norquis, *Inorg. Chem.* **2008**, *47*, 8518–8525.
31. J. Song, X. Ni, L. Gao, H. Zheng, *Mater. Chem. Phys.* **2007**, *102*, 245–248.
32. V. V. Atuchin, T. A. Gavrilova, V. G. Kostrovsky, L. D. Pokrovsky, I. B. Troitskaia, *Inorg. Mater.* **2008**, *44*, 622–627.
33. V. M. Jain, D. V Shah, K. K. Patel, Y. Doshi, *IOP Conf. Ser. Mater. Sci. Eng.* **2021**, *1126*, 012052.

34. B. Chae, Y. M. Jung, X. Wu, S. Bin Kim, *J. Raman Spectrosc.* **2003**, *34*, 451–458.

35. V. W. Day, M. F. Fredrich, W. G. Klemperer, W. Shum, *J. Am. Chem. Soc.* **1977**, *99*, 6146–6148.

CHAPTER 3

Structure and Thermal Transformation of Methylammonium Vanadate

3.1 Introduction

Polyoxovanadates are unique polyoxometalates due to the variable oxidation state of vanadium (+3, +4, and +5) and the coordination spheres of V–O polyhedra (VO_4 tetrahedron, VO_5 square pyramid and trigonal bipyramid, and VO_6 octahedron).[1–4] Polyoxovanadates have been reported with either fully oxidized, reduced, or mixed-valence vanadium species, such as $[V_2O_7]^{4-}$,[5] $[V_3O_9]^{3-}$,[6] $[V_4O_{12}]^{4-}$,[7] $[V_5O_{14}]^{3-}$,[8] $[V_{10}O_{28}]^{6-}$,[9] $[V_{12}O_{32}]^{4-}$,[10] $[V_{13}O_{34}]^{3-}$,[10] $[V_{15}O_{36}]^{5-}$,[11] $[H_4V_{15}O_{42}]^{5-}$,[12] $[V_{16}O_{42}]^{4-}$,[13] $[V_{17}O_{42}]^{4-}$,[14] $[V_{18}O_{42}(PO_4)]^{11-}$,[15] $[V_{19}O_{41}(OH)_9]^{8-}$,[16] $[V_{34}O_{82}]^{10-}$,[17] and polymeric $([VO_3]^-)_\infty$.[18,19] Polyoxovanadates are utilized as medicine,[20] bioinorganic chemistry,[21] homogeneous and heterogeneous catalysis,[22] and as staining reagents.[23]

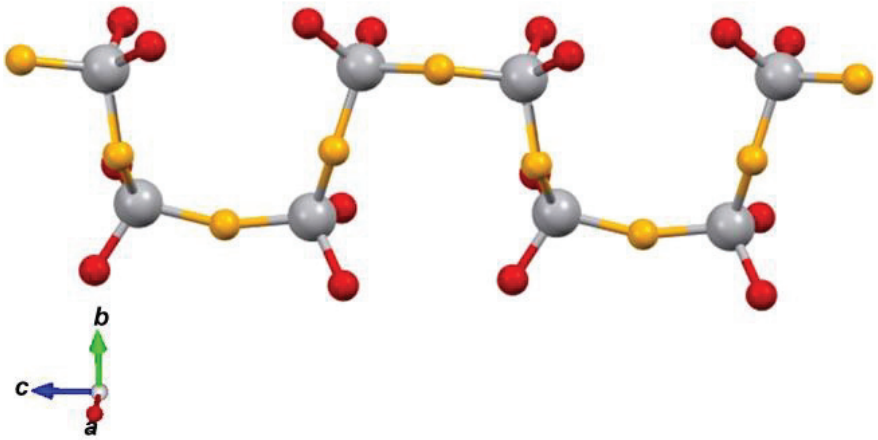

Figure 3.1. "Snake-like" chain structure of a $([VO_3]^-)_n$ anion along the *c*-direction. Grey, red, and yellow balls represent vanadium, terminal oxygen, and bridging oxygen, respectively.

In this chapter, we report the dissolving of V_2O_5 in aqueous methylamine solution and subsequent drying produced methylammonium vanadate, $(CH_3NH_3)[VO_3]$ and reversible structural transformation of methylammonium vanadate, $(CH_3NH_3)[VO_3]$ in the temperature range of −150 to −100 °C. The direction of the methylammonium molecules in the crystal packing was reversibly changed when the temperature exceeded the transformation temperature. However, heating solid at ~ 275 °C causes irreversibly releases methylamine and V_2O_5 is formed. Although, the "snake-like" chain structure of methylammonium vanadate at room temperature (at 23 °C) has been reported,[18] in the my result report about the thermally-induced reversible rearrangement of methylammonium cations in the crystal packing.

3.2 Experimental Section

Materials: All chemicals were of reagent grade and used without further purification. V_2O_5 was purchased from Kojundo Chemical Laboratory Co., Ltd. and 40% methylamine solution was purchased from Kanto Chemical Co., Inc. Homemade deionized water (Millipore, Elix, USA, MA) was used throughout this study.

Preparation of $(CH_3NH_3)[VO_3]$. V_2O_5 (2.05 g, V: 22.5 mmol) was mixed with 5.4 mL of 40% methylamine solution with a methylamine/V ratio of 2.8. The resulting mixture was then stirred for 30 min forming in a colorless solution. The solution was heated at 70 °C under atmospheric pressure to remove the unreacted methylamine and water, and 3.04 g of a white solid was obtained. Thermogravimetric analysis (TGA) revealed a 30.6% weight loss upon heating at 400 °C, which corresponds to the loss of 1 CH_3NH_2 and 0.5 H_2O from $(CH_3NH_3)[VO_3]$ to form V_2O_5 (30.5%). IR, $\tilde{\nu}/cm^{-1}$(KBr): 3000 (m), 1614 (m), 1594 (sh), 1506 (m), 1490 (m), 1473 (w), 1457 (m), 1419(w), 1263 (w), 939 (s, sh), 919 (vs), 894 (s), 831 (vs), 777 (vs), 655 (vs). Elemental analysis calcd. for $(CH_3NH_3)[VO_3]$: H 4.63, C 9.17, N 10.69; found, H 4.53, C 9.03, N 10.39.

Single crystals of $(CH_3NH_3)[VO_3]$. $(CH_3NH_3)[VO_3]$ (0.1 g) was dissolved in 1 mL of water at 60 °C and the temperature was slowly decreased to room temperature.

Colorless crystals suitable for single-crystal X-ray structural analysis were obtained after 24 h.

Calcination of $(CH_3NH_3)[VO_3]$. $(CH_3NH_3)[VO_3]$ was calcined in air at 100, 125, 150, 175, 200, 225, 250, 275, 300, 325, and 350 °C. The temperature was increased to the target temperature at a heating rate of 10 °C/min and the temperature was maintained for 1 h.

Analytical techniques. Powder X-ray diffraction patterns were measured on a Bruker D2 PHASER 2nd Gen using Cu-K_α radiation. The samples were ground, placed on a sample holder, and the XRD profiles were recorded in the 2θ range of 3°–80°. Fourier transform infra-red (FT-IR) spectra were obtained on a NICOLET 6700 FT-IR spectrometer (Thermo Fischer Scientific) in the wavenumber range of 500–4000 cm^{-1} in KBr pellets. Thermogravimetric–differential thermal analysis (TG-DTA) was performed on a TG-DTA7300 instrument (SII) with an air or nitrogen flow of 200 mL s^{-1}. Temperature programmed desorption (TPD) was performed using a BELCAT II – BELMASS system (MicrotracBEL Corp.) under a flow of helium gas. The heating rate was 10 °C min^{-1} and the maximum temperature was 600 °C. ^{51}V NMR spectra were recorded using JEOL JNM-LA400 (V resonance frequency: 105.15 MHz) at 25 °C. The spectra were reference to the external $VOCl_3$ (0 ppm). Ultraviolet-visible spectra were obtained using an Agilent 8453 UV-visible spectrometer in the range of 190–1100 nm with a cell length of 1 cm. Raman spectra were collected using a JASCO RMP-510 with a 532.0 nm laser and each spectrum was collected for 1 s and accumulated three times. Differential scanning calorimetry (DSC) was performed using an EXSTAR DSC7020 instrument (Hitachi High-Tech Corp.) with a nitrogen flow rate of 50 mL s^{-1}. The temperature changing rate was 10 °C min^{-1} and the temperature range was 25 to –147 °C. CHN analyses were performed at Division of Instrumental Analysis, Okayama University.

X-ray crystallography. Single-crystal X-ray diffraction data for $(CH_3NH_3)[VO_3]$ were collected at 23, 0, –50, –100, and –150 °C on a Bruker SMART APEX2 instrument using Mo K_α radiation (λ = 0.71073 Å) monochromated by a layered confocal mirror. Data reduction and space group determination were performed

using the Bruker APEX 3 suite.[24] Absorption correction was applied using a multi-scan technique (SADABS).[24] The structure was solved by direct methods using SHELXT[25] and refined using SHELXL[26] using the SHELXle[27] interface. We assigned N and C in one methylammonium cation ($CH_3NH_3^+$) by checking the distances between these atoms and the oxygen atoms bound to V. The crystal data obtained at 23 and –150 °C are summarized in Table 3.1.

CCDC 2158737 (–150 °C), 2158738 (23 °C), 2169861 (–100 °C), 2169862 (–50 °C), and 2169863 (0 °C) contain supplementary crystallographic data for methylammonium vanadate, which can be obtained free of charge from the Cambridge Crystallographic Data Centre (CCDC).

3.3 Result and Discussion

3.3.1 Synthesis and variable-temperature single-crystal structure analysis

Methylammonium vanadate was synthesized by dissolving V_2O_5 in methylamine solution (40%) with a methylamine/vanadium ratio of 2.8 at room temperature, and then the solution was dried at 70 °C. By recrystallizing the raw solid from water, colorless crystals suitable for single-crystal X-ray structural investigation were obtained.

Single crystal X-ray diffraction analysis at 23 and −150 °C revealed that an asymmetric unit with four methylammonium cations and a "snake-like" $([VO_3]_4)^{4-}$ anion chain along the c-direction in the *Pna*2_1 space group was formed, according to single crystal X-ray diffraction analysis at 23 and −150 °C (Figure 3.1 and 3.2, and Table 3.1). The $CH_3NH_3^+$ cations were located between the parallel chains. The $([VO_3]_4)^{4-}$ anion has distorted tetrahedral $[VO_4]$ geometry for all of its V atoms. Terminal oxygens (O1, O2, O5, O6, O8, O9, O11, and O12) and bridge oxygens between two V atoms (O3, O4, O7, and O10) are two types of oxygen found in the structure. Infinite chains are formed where tetrahedral $[VO_4]$ are connected by corner-sharing bridging atoms.

Table 3.1. Crystal data obtained for methylammonium vanadate

Temperature	23 °C (296 K)	0 °C (273 K)	–50 °C (223 K)	–100 °C (173 K)	–150 °C (123 K)
Empirical formula	CNH_6VO_3	CNH_6VO_3	CNH_6VO_3	CNH_6VO_3	CNH_6VO_3
Formula weight (g/mol)	131	131	131	131	131
Crystal system	Orthorhombic	Orthorhombic	Orthorhombic	Orthorhombic	Orthorhombic
Space group	$Pna2_1$	$Pna2_1$	$Pna2_1$	$Pna2_1$	$Pna2_1$
a (Å)	11.9092(11)	11.9064(17)	11.9052(10)	11.8983(9)	12.5397(8)
b (Å)	18.6442(17)	18.621(3)	18.5660(15)	18.5228(14)	17.4526(11)
c (Å)	8.4751(8)	8.4718(12)	8.4721(7)	8.4701(7)	8.4880(5)
α (°)	90	90	90	90	90
β (°)	90	90	90	90	90
γ (°)	90	90	90	90	90
V (Å^3)	1881.8(3)	1878.3(5)	1872.6(3)	1866.7(3)	1857.6(2)
Z	16	16	16	16	16
$D_{calcd.}$ (g/cm^{-3})	1.850	1.853	1.859	1.865	1.874
μ (mm^{-1})	1.983	1.987	1.993	1.999	2.009
Radiation	Mo Kα (λ =0.71073 Å)				
F(000)	1056.0	1056.0	1056.0	1056.0	1056.0
G.O.F.	1.061	1.053	1.040	1.077	1.037
R indexes [$I > 2\sigma(I)$]	R_1 = 0.0276; wR_2 = 0.0702	R_1 = 0.0306; wR_2 = 0.0690	R_1 = 0.0277; wR_2 = 0.0637	R_1 = 0.0249; wR_2 = 0.0582	R_1 = 0.0222; wR_2 = 0.0529
R indexes [all data]	R_1 = 0.0310; wR_2 = 0.0724	R_1 = 0.0362; wR_2 = 0.0721	R_1 = 0.0316; wR_2 = 0.0657	R_1 = 0.0278; wR_2 = 0.0597	R_1 = 0.0242; wR_2 = 0.0540

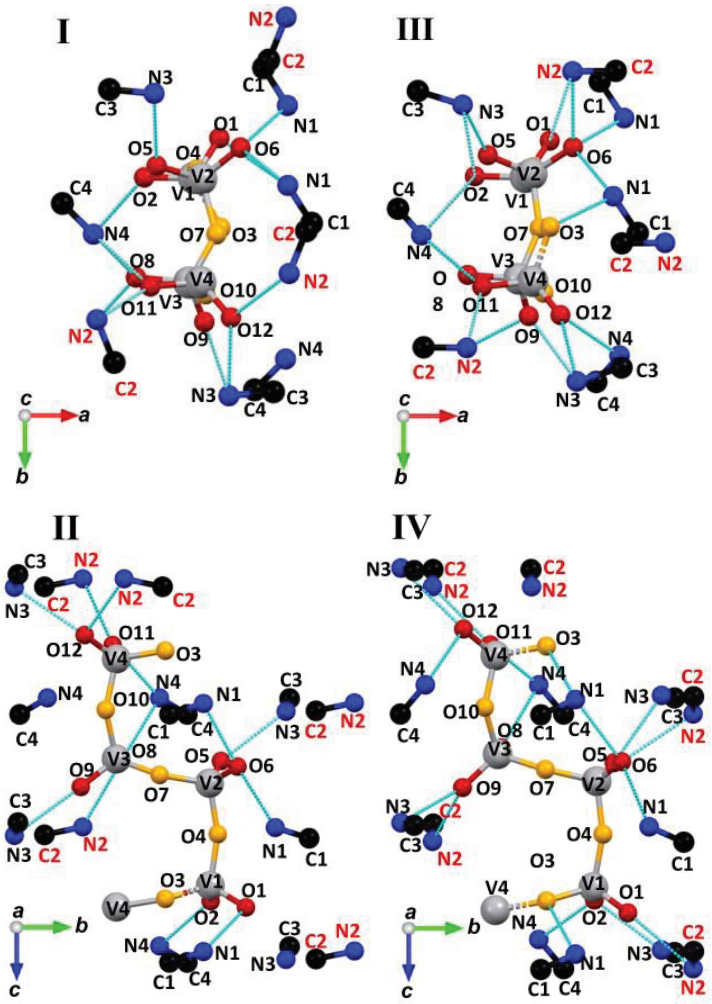

Figure 3.2. Crystal structure and atom labeling for methylammonium vanadate obtained at temperature 23 °C viewed along the *c*-direction (I) and *a*-direction (II), and at −150 °C viewed along the *c*-direction (III) and *a*-direction (IV). Hydrogen atoms were omitted for clarity. Grey, red, yellow, black, and blue balls represent vanadium, terminal oxygen, bridging oxygen, carbon, and nitrogen atoms, respectively. Light blue lines represent the hydrogen bonds formed between the N and O atom, which are shorter than 3.0 Å.

The crystal structure discovered at 23 °C was identical to that which Averbuch-Pouchot and Durif reported,[18] which differs from the reported straight-chain structure of ammonium metavanadate, $(NH_4)VO_3$.[19] The distance between the

vanadium and terminal oxygen atoms has an average value of 1.64 Å, and that between vanadium and the bridging oxygen atoms was 1.79 Å. The O–V–O angle varies from 106.96° to 112.21°. Tables 3.2 and 3.3 show lists of selected bond lengths and angles, respectively. According to the bond valence sum (BVS), vanadium was in the +5 oxidation state (Table 3.4). Elemental analysis indicates that the formula is $(CH_3NH_3)[VO_3]$ and the ^{51}V NMR of the methylammonium vanadate could be measured (see below), confirming that the vanadium was in the 5+ oxidation state.

Table 3.2. Selected bond distances.

Oxygen type	23 °C		–150 °C	
	Bond	**Length (Å)**	**Bond**	**Length (Å)**
Bridging Oxygen	O3-V4	1.810(3)	O3-V4	1.827(2)
	O3-V1	1.808(3)	O3-V1	1.809(2)
	O4-V1	1.778(5)	O4-V1	1.807(3)
	O4-V2	1.768(5)	O4-V2	1.782(3)
	O7-V2	1.797(3)	O7-V2	1.779(2)
	O7-V3	1.798(3)	O7-V3	1.805(2)
	O10-V3	1.793(4)	O10-V3	1.807(2)
	O10-V4	1.783(4)	O10-V4	1.794(2)
Terminal Oxygen	O1-V1	1.636(3)	O1-V1	1.629(2)
	O2-V1	1.630(3)	O2-V1	1.658(2)
	O5-V2	1.626(3)	O5-V2	1.633(2)
	O6-V2	1.646(3)	O6-V2	1.677(2)
	O8-V3	1.657(3)	O8-V3	1.628(2)
	O9-V3	1.617(3)	O9-V3	1.654(2)
	O11-V4	1.625(3)	O11-V4	1.645(2)
	O12-V4	1.657(3)	O12-V4	1.638(2)

Table 3.3. Selected O-V-O angles

23 °C		–150 °C	
Bond	**Angle (°)**	**Bond**	**Angle (°)**
O1-V1-O2	107.50(18)	O1-V1-O2	107.72(11)
O1-V1-O4	108.47(18)	O1-V1-O4	109.13(11)
O2-V1-O4	111.97(18)	O2-V1-O4	112.04(11)
O1-V1-O3	107.89(16)	O1-V1-O3	106.29(11)
O2-V1-O3	110.71(13)	O2-V1-O3	111.37(10)
O4-V1-O3	110.14(14)	O4-V1-O3	110.07(10)
O5-V2-O6	108.93(18)	O5-V2-O6	109.75(11)
O5-V2-O7	112.21(15)	O5-V2-O7	112.30(11)
O6-V2-O7	108.04(15)	O6-V2-O7	107.08(10)
O5-V2-O4	111.01(18)	O5-V2-O4	110.28(11)
O6-V2-O4	107.44(17)	O6-V2-O4	108.16(10)
O7-V2-O4	109.05(15)	O7-V2-O4	109.14(10)
O8-V3-O9	108.92(16)	O8-V3-O9	109.55(11)
O8-V3-O7	111.65(13)	O8-V3-O7	109.61(10)
O9-V3-O7	107.87(19)	O9-V3-O7	111.57(11)
O8-V3-O10	111.65(13)	O8-V3-O10	109.72(11)
O9-V3-O10	108.76(15)	O9-V3-O10	109.01(10)
O7-V3-O10	108.45(15)	O7-V3-O10	107.35(10)
O12-V4-O11	110.49(15)	O12-V4-O11	109.63(11)
O12-V4-O10	106.96(15)	O12-V4-O10	106.43(11)
O11-V4-O10	110.61(15)	O11-V4-O10	111.77(11)
O12-V4-O3	109.77(14)	O12-V4-O3	111.08(10)
O11-V4-O3	110.84(14)	O11-V4-O3	110.66(10)
O10-V4-O3	108.07(14)	O10-V4-O3	107.19(10)

The *a*-axis increased (by about 5%) and the *b*-axis decreased (by about 6%) when the analysis temperature was decreased to -150 °C, but the *c*-axis remained unchanged. At -150 °C, the cell volumes decreased about 1%. The arrangement of the $\{VO_4\}$ tetrahedra is unaffected by this transformation. A "snake-like" chain along the *c*-direction was still observed.

The single-crystal X-ray data of the crystal at -150 °C generated a different simulated diffraction pattern from the crystal at 23 °C (Figure 3.3 (a) and (b)), indicating transformation of a single crystal into another single crystal. The crystal structure observed at –150 °C was comparable to that obtained at 23 °C, which was constructed from four methylammonium cations and one $([VO_3]_4)^{4-}$ anion. The

distance between the vanadium and terminal oxygen atoms has an average value of 1.65 Å and the distance between the vanadium and bridging oxygen atoms was 1.80 Å. The O–V–O angle varies from 106.29° to 112.30°. Selected bond lengths and angles are listed in Tables 3.2 and 3.3, respectively. The BVS results indicated that vanadium was in the 5+ oxidation state (Table 3.5).

Table 3.4. Bond valence sum (BVS) calculations for the V atoms in methylammonium vanadate at 23 °C.

Bond	Bond length (Å)	Bond Valence[a]	BVS[b]
V1-O4	1.778	1.0699	5.2230
V1-O3	1.808	0.9866	
V1-02	1.63	1.5961	
V1-O1	1.636	1.5704	
V2-O6	1.646	1.5286	5.1727
V2-O4	1.768	1.0992	
V2-O7	1.797	1.0163	
V2-O6	1.646	1.5286	
V3-O8	1.657	1.4838	5.1780
V3-O9	1.617	1.6532	
V3-O10	1.793	1.0274	
V3-O7	1.798	1.0136	
V4-O12	1.657	1.4838	5.6409
V4-O11	1.625	1.6178	
V4-O10	1.783	1.0555	
V4-O12	1.657	1.4838	

[a] $S_{ij} = \exp\left(\frac{R_0 - R_{ij}}{B}\right)$

[b] $V_i = \sum S_{ij}$

where V_i is the oxidation state of atom i, S_{ij} is the bond valence, R_0 is the empirically determined V(5+)–O(2-) distance (1.803 Å), R_{ij} is the length of the cation–anion bond, and B is a universal parameter (0.37).

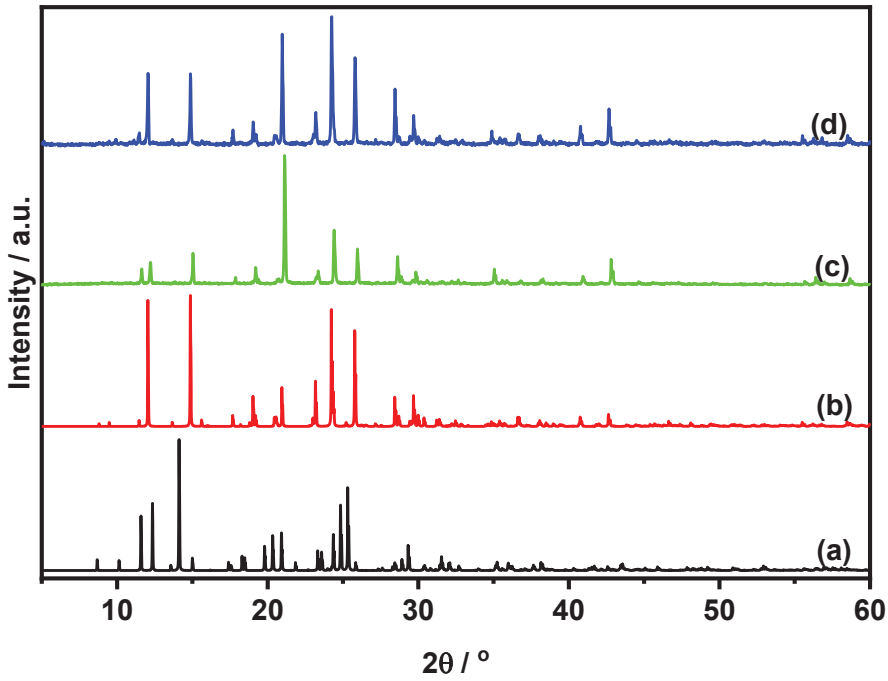

Figure 3.3. Simulated XRD patterns for methylammonium vanadate based on the single-crystal data measured obtained at −150 °C (a) and 23 °C (b), and the XRD patterns observed for methylammonium vanadate after evaporation (c) and being heated at 100 °C (d).

Table 3.5. Bond valence sum (BVS) calculations for the V atoms in methylammonium vanadate at –150 °C.

Bond	Bond length (Å)	Bond valence[a]	BVS[b]
V1-O1	1.629	1.6004	5.0534
V1-O2	1.658	1.4798	
V1-O4	1.807	0.9892	
V1-O3	1.809	0.9839	
V2-O5	1.633	1.5832	5.1143
V2-O6	1.677	1.4095	
V2-O7	1.779	1.0670	
V2-O4	1.782	1.0584	
V3-O8	1.628	1.6048	5.0845
V3-O9	1.654	1.4959	
V3-O7	1.805	0.9946	
V3-O10	1.807	1.0081	
V4-O12	1.638	1.5961	5.0565

V4-O11	1.645	1.5535
V4-O10	1.794	1.0358
V4-O3	1.827	0.9372

[a] $S_{ij} = \exp\left(\frac{R_0 - R_{ij}}{B}\right)$

[b] $V_i = \sum S_{ij}$

where V_i is the oxidation state of atom i, S_{ij} is the bond valence, $R_{0\ is}$ the empirically determined V(5+)–O(2-) distance (1.803 Å), R_{ij} is the length of the cation–anion bond, and B is a universal parameter (0.37).

One major difference between the crystals observed at 23 and –150 °C was the position of one methylamine (C2-N2) (Figure 3.2). In the crystal at -150 °C, the second methylammonium cation ($C2H_3$-$N2H_3^+$) was parallel to the *a*-axis. But in the crystal observed at 23 °C, the same methylammonium cation was parallel to the *b*-axis (Figure 3.2). The orientation of this cation causes different interactions with the vanadate anions. Hydrogen bonds play a crucial role in crystal formation because the terminal and bridging oxygen atoms can act as donors to generate hydrogen bonds with nearby $CH_3NH_3^+$ cations. Figure 3.2 shows the hydrogen bonds between the N and O atoms with a distance of <3 Å and Table S6 shows the hydrogen bond lengths between the N and O atoms.

Figure 3.2 and Figure 3.4 show four methylammonium molecules in the crystal at –150 and 23 °C. The first methylammonium (C1-N1) in the crystal observed at -150 °C was connected to the terminal and bridging oxygen atoms in the same chain (O6, O3) and one terminal oxygen atom of another chain (O6). In contrast, the first methylammonium (C1-N1) interacts with two terminal oxygen atoms in the same chain (O6, O1) and one terminal oxygen atom in another chain (O6) in the crystal observed at 23 °C. The second methylammonium (C2-N2) in the crystal observed at –150 °C was connected to each of the two oxygen terminals of the two chains (O9, O11, O1, O6).). In contrast, the second methylammonium (C2-N2) interacts with two terminal oxygen atoms in the same chain (O8, O11) and one terminal oxygen from another chain (O12) in the crystal observed at 23 °C. The third methylammonium (C3-N3) in the crystal observed at –150 °C was connected to two terminal oxygen atoms of the same chain (O5, O2) and two terminal oxygen from

another chain (O9, O12). In contrast, the third methylammonium (C3-N3) interacts with two terminal oxygen atoms of the same chain (O9, O12) and one terminal oxygen from another chain (O5) in the crystal observed at 23 °C. The last methylammonium (C4-N4) in the crystal at –150 °C was connected to three terminal oxygen atoms of the same chain (O2, O8, O11) and one terminal oxygen from another chain (O12). In contrast, the fourth methylammonium (C4-N4) interacts with three terminal oxygen atoms of the same chain (O2, O8, O11) in the crystal observed at 23 °C. Based on these results, the crystal structure observed at –150 °C contains more hydrogen bonds. These make the structure denser and therefore, the cell volume of the crystal observed at –150 °C (1857.6 $Å^3$) was smaller than at 23 °C (1881.8 $Å^3$).

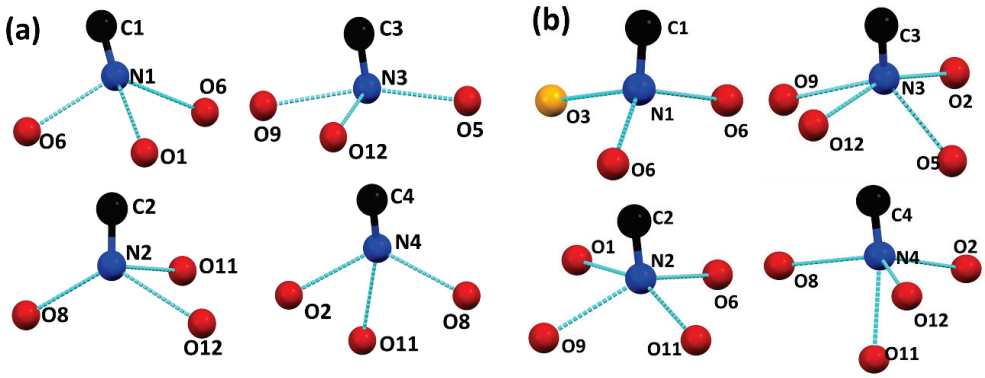

Figure 3.4. Hydrogen bonds (N-H··O) formed between the methylammonium cation and oxygen atom of the vanadate anion at 23 °C (a) and –150 °C (b). The hydrogen atoms were omitted for clarity. The red, yellow, black, and blue balls represent the terminal oxygen, bridging oxygen, carbon, and nitrogen atoms, respectively. The light blue lines represent the hydrogen bonds formed between the N and O atoms, which are shorter than 3.0 Å.

Single-crystal X-ray structural analyses were carried out at different temperatures (Figure 3.5). All of the axis lengths slightly decreased when the temperature was decreased from 23 to 100 °C. The *a*- and *c*-axis lengths suddenly increase when the temperature is decreased to -150 °C, showing that the crystal structure changed between -100 and -150 °C. The lengths of the *a*- and *c*-axes were reversibly

decreased by heating from -150 to -100 °C. When the temperature exceeded the transformation temperature during either cooling or heating, the unit cell parameters changes of the crystals were fully reversible. All of the cell parameters decreased when the temperature was decreased to -100 °C, and the crystal structures observed at 23, 0, -50, and -100 °C were the same to those reported by Averbuch-Pouchot and Durif.[18]

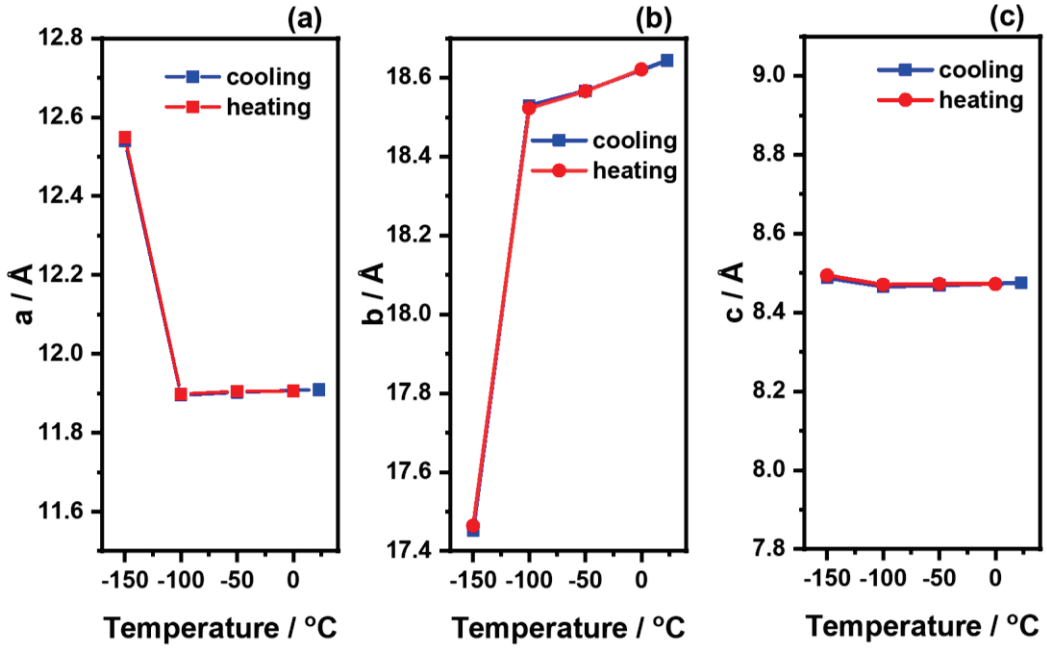

Figure 3.5. Unit cell parameters of methylammonium vanadate upon cooling and heating. *a*-axis (a), *b*-axis (b), and *c*-axis (c).

DSC measurements were carried out in cooling and heating mode (10 °C min^{-1}) in the temperature range of 25 to –147 °C under a flow of nitrogen gas (Figure 3.6). The reversibility of the phase transformation between the two crystals was confirmed by DSC thermogram. An exothermic peak was observed at –119 °C (536 J mol^{-1}) upon cooling and an endothermic peak was observed at –103 °C (677 J mol^{-1}) upon heating with a thermal hysteresis of approximately 16 °C, which is characteristic of single-crystal-to-single-crystal systems.[28,29] This result was consistent with our single-crystal X-ray diffraction investigation results, which showed that the crystal structure exhibited a reversible transformation between –100 and –150 °C.

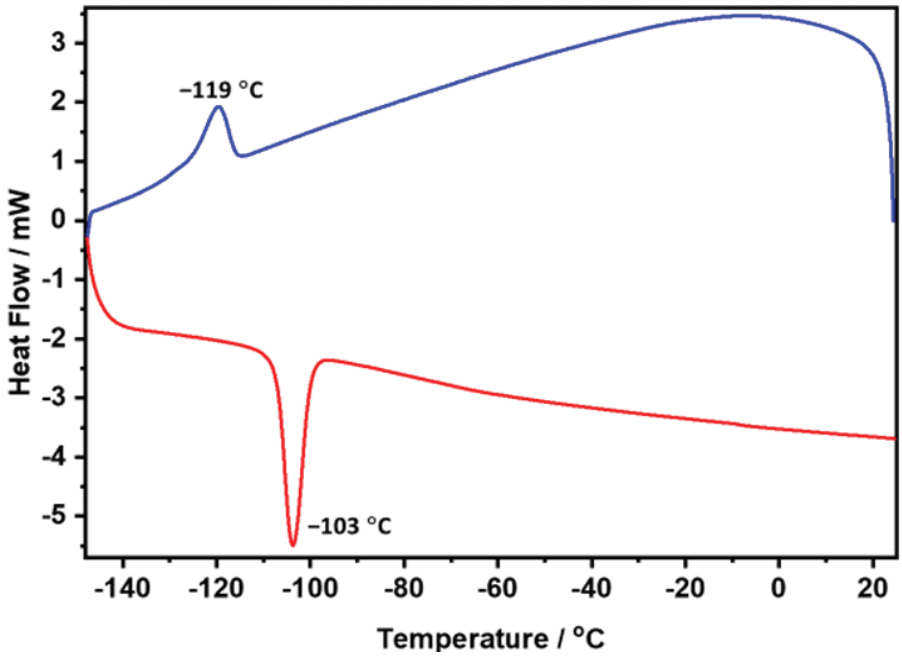

Figure 3.6. DSC curves obtained for methylammonium vanadate (10 °C min^{-1}) in cooling (blue line) and heating (red line) mode.

3.3.2 Characterization of methylammonium vanadate

Figure 3.3 shows the simulated and experimental powder XRD patterns for methylammonium vanadate. Peak positions of the experimental powder XRD profiles obtained heating at 70 and 100 °C were comparable to the simulated powder XRD pattern obtained using the single-crystal X-ray data at 23 °C. This result indicates that the powder had the same crystal structure and the phase purity of the bulk powder was satisfactory.

The solid-state Raman spectra for methylamine hydrochloride and methylammonium vanadate are shown in Figure 3.7. C-N stretching vibration of methylammonium was identified at 1004 cm^{-1}, which confirmed the presence of methylammonium as a counter cation. The symmetric stretching of the di-oxo $V(=O)_2$ unit is the cause of the strong Raman band at 947 cm^{-1}. [30] The Raman spectrum shows both symmetric and asymmetric V-O bridging stretching modes at 480 and 644 cm^{-1}, respectively. The asymmetric and symmetric V-O terminal

stretching vibrations are observed in the Raman spectrum at 896 and 928 cm^{-1} (shoulder), respectively. [31]

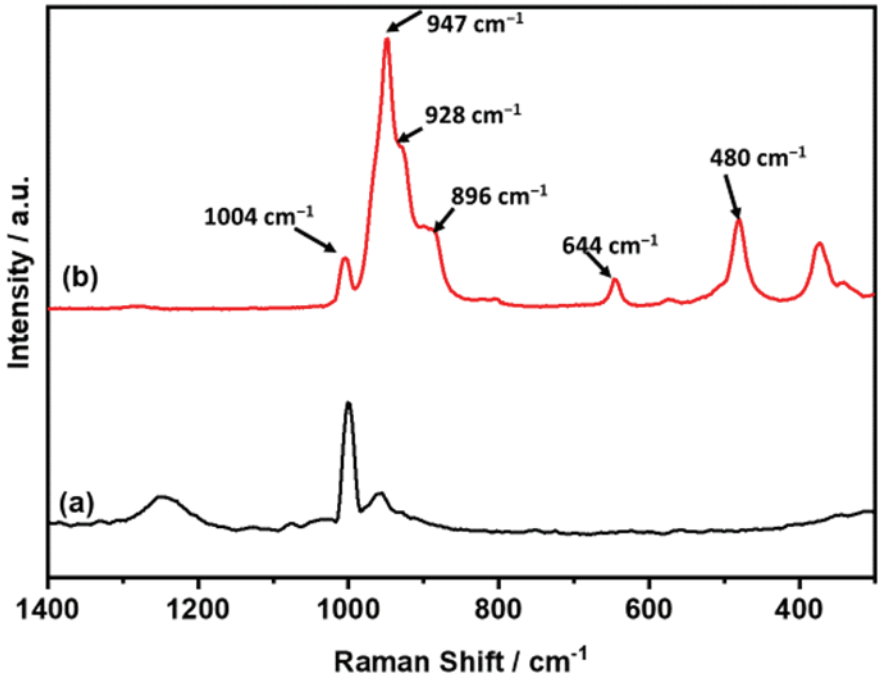

Figure 3.7. Raman spectra obtained for methylamine hydrochloride ($CH_3NH_3^+Cl^-$) (a) and methylammonium vanadate (b).

Figure 3.8 shows the FT-IR spectrum of methylammonium vanadate. The spectrum contains bands corresponding to V=O_t at 939, 919, and 894 cm^{-1}, V-O_b-V at 831, 777, and 655 cm^{-1}, and NH_3^+ and CH_3 bending at 1496, 1469, 1425, and 1265 cm^{-1}.[7,32]

In addition, ^{51}V NMR was used to investigate the structure of methylammonium vanadate in water. Figure 3.9 shows the ^{51}V NMR spectrum of methylammonium vanadate in H_2O. The major vanadate is tetravanadate $[V_4O_{12}]^{4-}$ (-577 ppm) together with pentavanadate $[V_5O_{15}]^{5-}$ (-584 ppm), divanadate $[V_2O_7]^{4-}$ (-572 ppm), and monovandate $[VO_4]^{3-}$ (-560 ppm) which is identical to the case of $NaVO_3$.[33]

Pentavanadate amount increased along with concentration of solution. It is well understood that a several vanadate species may exist equilibrium in solution.[34] According to the $O_t \rightarrow V$ and $O_b \rightarrow V$ charge transfers, the UV-Vis absorption

spectrum of methylammonium vanadate in water (Figure 3.10) shows absorption peaks centered at 207 and 266 nm, respectively.[35]

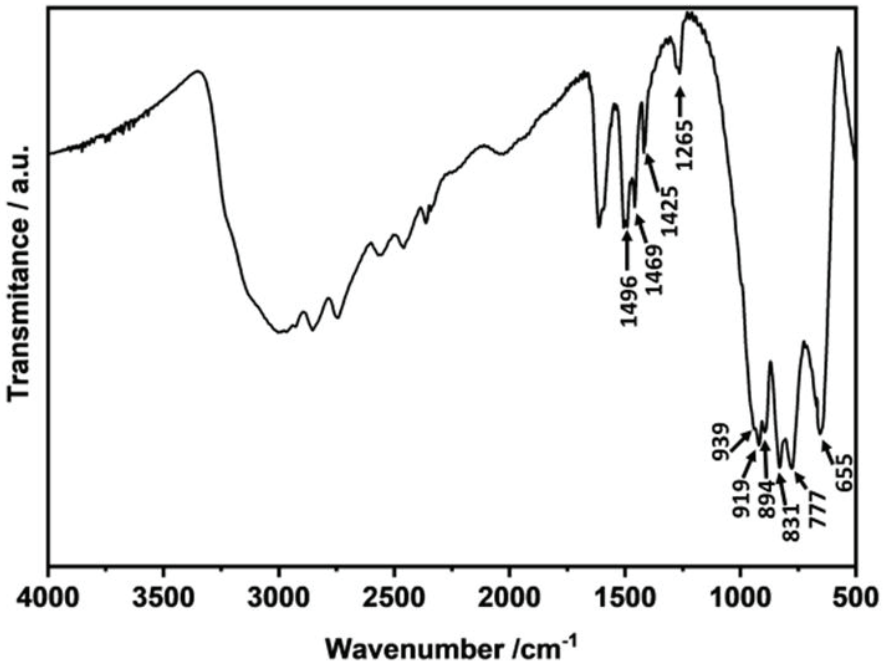

Figure 3.8. FT-IR spectrum obtained for methylammonium vanadate.

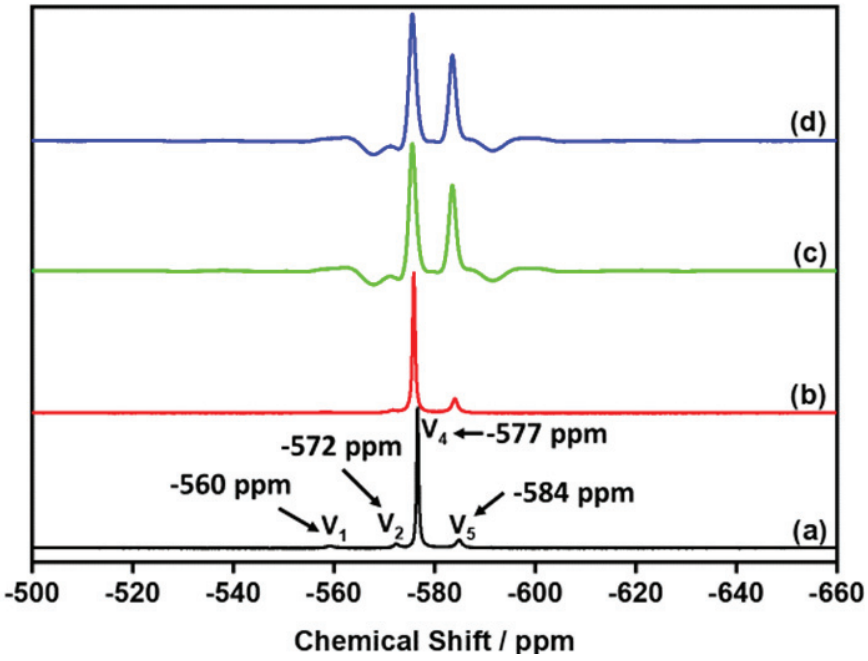

Figure 3.9. ^{51}V NMR spectra of methylammonium vanadate in H_2O at different concentrations 0.03 (a), 0.1 (b), 0.5 (c), and 1 M (d)

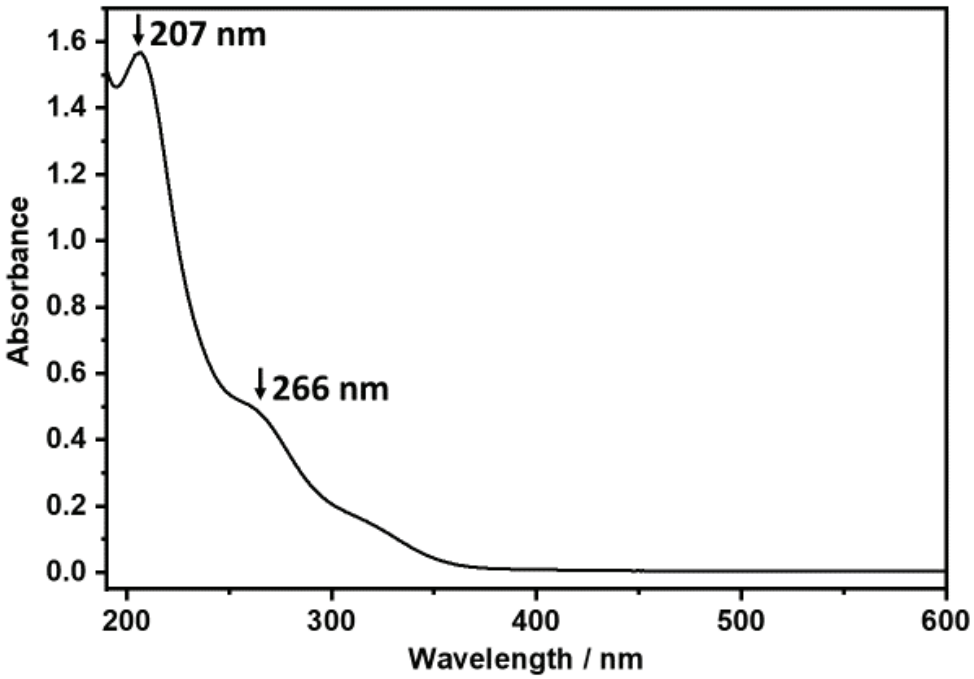

Figure 3.10. UV-Vis spectrum obtained for methylammonium vanadate. Solution concentration: 0.003 wt.% (0.003 g/100 mL H_2O, ca. 0.23 mM).

3.3.3 Structural transformation during heating

The thermogravimetric (TG) and differential thermal analysis (DTA) curves obtained for methylammonium vanadate in air (Figure 3.11) indicate multistep weight loss. The results also indicate that the solid was stable at temperatures below 100 °C. According to the TG curve, weight loss up to 400 °C was 30.6%. This weight loss is equivalent to one methylammonium and 0.5 H_2O from $(CH_3NH_3)[VO_3]$ to form 0.5 V_2O_5 (30.5%). This result was consistent with the amount of crystal water and methylammonium from single-crystal X-ray diffraction analysis.

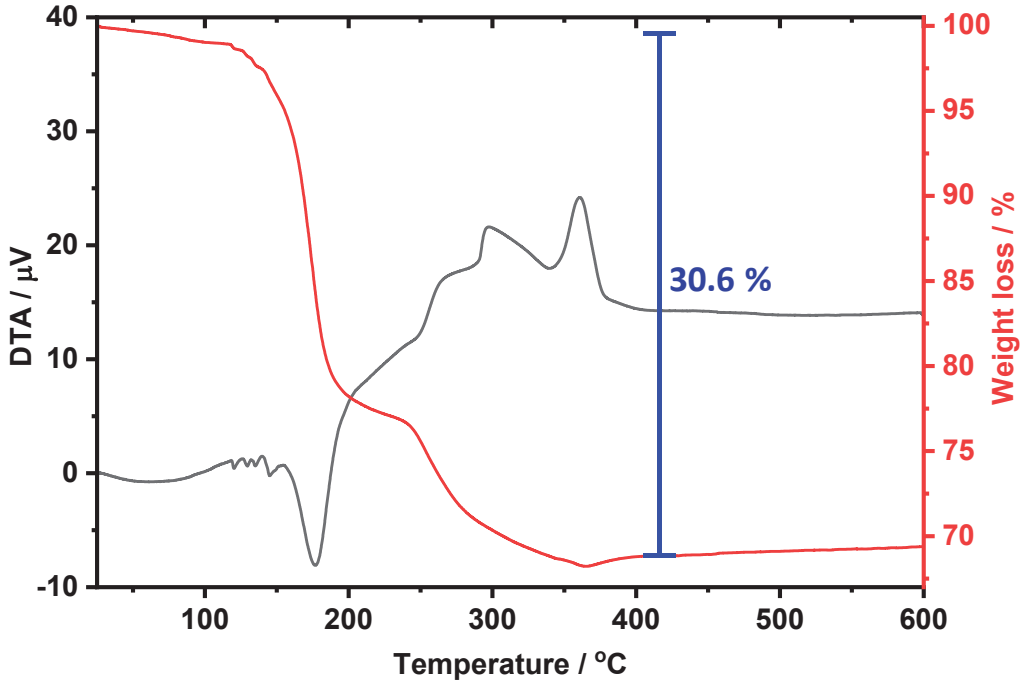

Figure 3.11. TG/DTA curves obtained for methylammonium vanadate under a flow of air.

The evolution of methylammonium during heating was investigated by temperature-programmed desorption-mass spectrometry (TPD-MS) in the condition of a flow of helium gas and TG-DTA in the presence of a flow of nitrogen gas (Figure 3.12). Furthermore, several gases with m/z values of 44, 31, 30, 28, 18, 17, and 16 were observed. Most methylammonium was removed in the first decomposition step under 200 °C. The desorption of H_2O and CH_3NH_2 was accompanied by the formation of oxidation and degradation products of methylammonium, including NH_3, CO, N_2, NO, CO_2, and N_2O. This suggests the occurrence of a redox reaction between methylammonium and V=O. Similar degradation and oxidation reactions of methylamine in methylammonium paradodecatungstate was presented in chapter 2.[36] Further increasing the temperature caused the next step of the decomposition. These decompositions aligned with the IR spectra of heated compound. As the temperature increases, the

intensity of the methylammonium-related IR bands decreases (Figure 3.13), indicating partial decomposition.

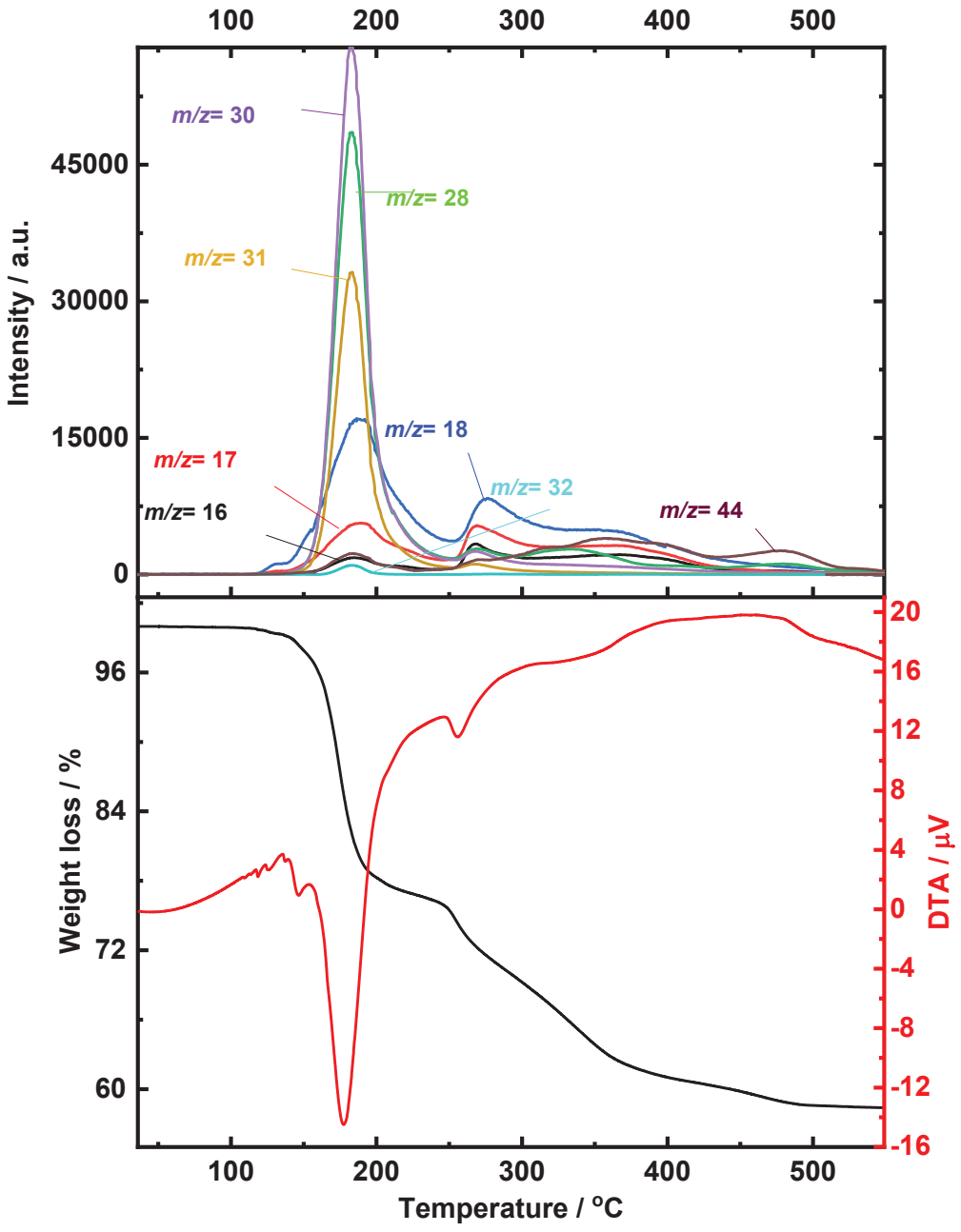

Figure 3.12. TG/DTA curves obtained under a flow of nitrogen gas and TPD-MS profile obtained under a flow of He gas for methylammonium vanadate.

The structural transformation of methylammonium vanadate was then investigated using infrared spectroscopy and X-ray powder diffraction. IR bands of methylammonium were less intense upon heating, which suggested that the counter-cations were gradually released before completely disappearing at <200 °C (Figure 3.13). The powder XRD patterns of the heated methylammonium vanadate sample are shown in Figure 3.14. The crystal structure was only stable up to 100 °C. After heating the solid to a temperature of higher than 125 °C, the main peaks of methylammonium vanadate disappear. An amorphous compound with a broad peak at 10.12° (d-spacing larger than 8.76) was formed when methylammonium and water were released, which might be a polyoxometalate species but the further characterization was not included. The final product, V_2O_5, was formed upon heating to 275 °C.

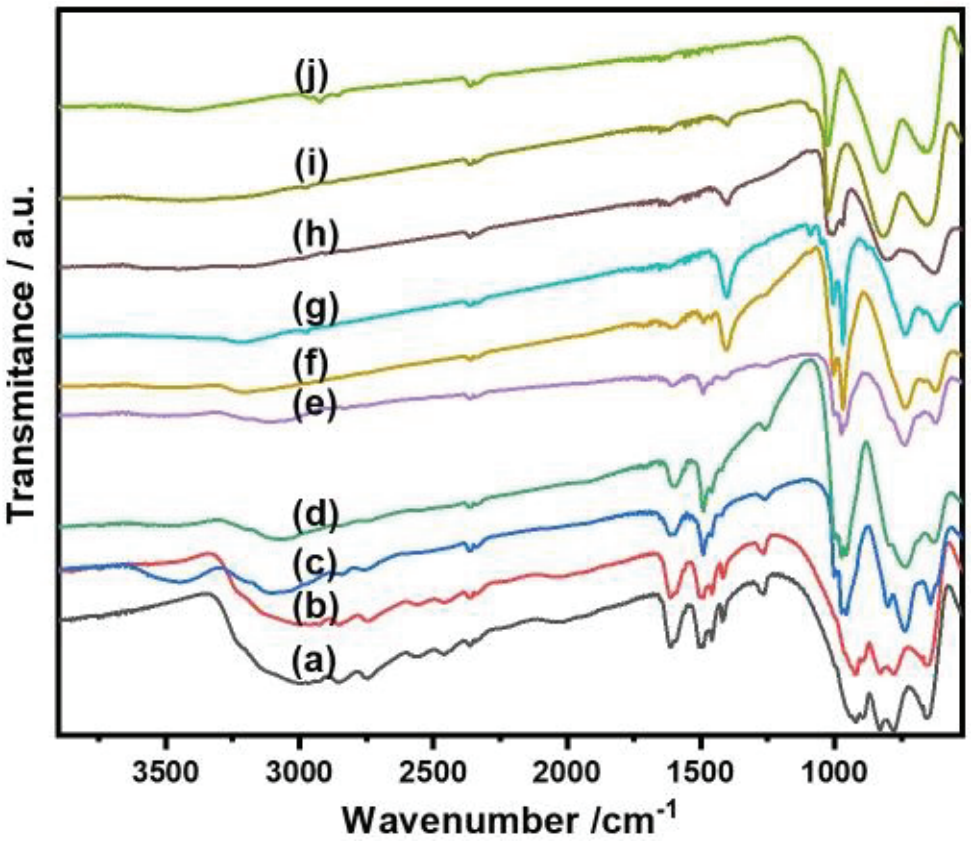

Figure 3.13. FT-IR spectra obtained for fresh methylammonium vanadate (a) and the resulting solids obtained after heating at 100 (b), 125 (c), 150 (d), 175 (e), 200 (f), 225 (g), 250 (h), 275 (i), and 350 °C (j).

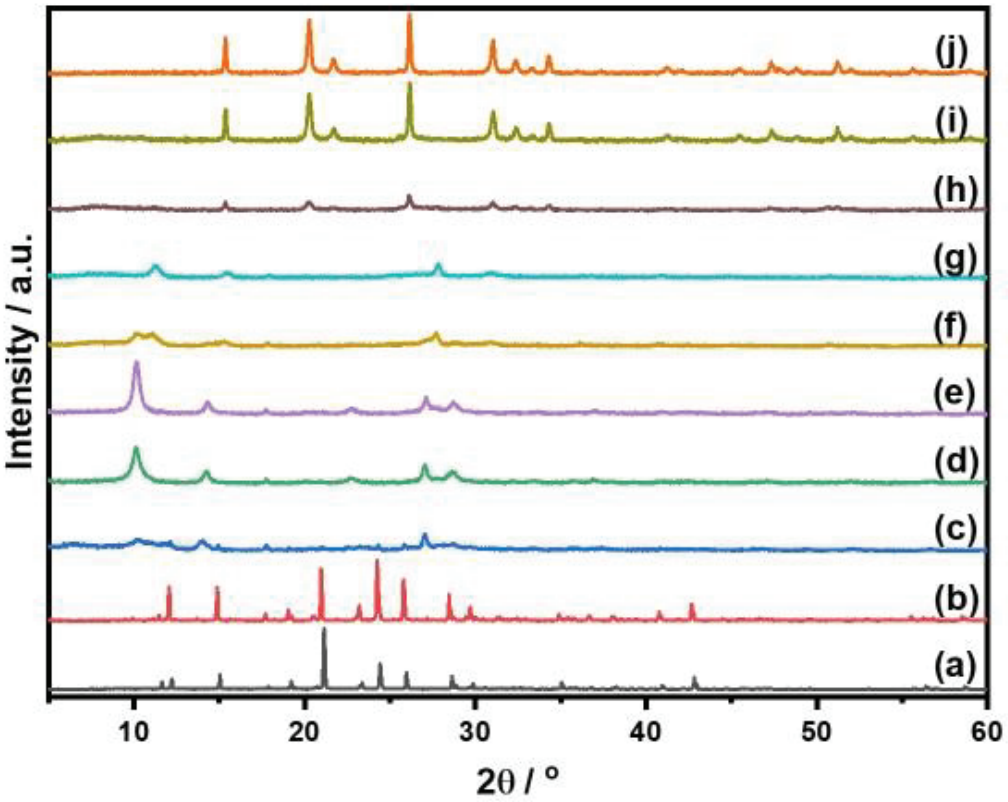

Figure 3.14. XRD patterns obtained for fresh methylammonium vanadate (a) and the resulting solids obtained after heating at 100 (b), 125 (c), 150 (d), 175 (e), 200 (f), 225 (g), 250 (h), 275 (i), and 350 °C (j).

3.4 Conclusions

Methylammonium vanadate, $(CH_3NH_3)[VO_3]$, was prepared by dissolving V_2O_5 in methylamine solution (40%) with a methylamine/vanadium ratio of 2.8 at room temperature and subsequent drying at 70 °C. The compound was made up of methylammonium counter-cations and "snake-like" $([VO_3]^-)_n$ anion chains propagating along the *c*-direction in the $Pna2_1$ space group. The solid-state reversible thermal structural transformation of methylammonium vanadate, $(CH_3NH_3)[VO_3]$, at ca. –110 °C has been observed. Single-crystal X-ray structural analysis at different temperatures indicated that the structural transformation was due to a change in the direction of the methylammonium cation. However, heating causes decomposition to form V_2O_5.

References

[1] K. Y. Monakhov, W. Bensch, P. Kögerler, *Chem. Soc. Rev.* **2015**, *44*, 8443–8483.

[2] J. Zhou, J.-W. Zhao, Q. Wei, J. Zhang, G.-Y. Yang, *J. Am. Chem. Soc.* **2014**, *136*, 5065–5071.

[3] Y. Hayashi, *Coord. Chem. Rev.* **2011**, *255*, 2270–2280.

[4] N. I. Gumerova, A. Rompel, *Chem. Soc. Rev.* **2020**, *49*, 7568–7601.

[5] N. Wang, Z. He, M. Cui, W. Guo, S. Zhang, M. Yang, *Cryst. Growth Des.* **2015**, *15*, 1619–1624.

[6] E. E. Hamilton, P. E. Fanwick, J. J. Wilker, *J. Am. Chem. Soc.* **2002**, *124*, 78–82.

[7] J. Li, C. Wei, D. Guo, C. Wang, Y. Han, G. He, J. Zhang, X. Huang, C. Hu, *Dalton Trans.* **2020**, *49*, 14148–14157.

[8] V. W. Day, W. G. Klemperer, O. M. Yaghi, *J. Am. Chem. Soc.* **1989**, *111*, 4518–4519.

[9] I. Mestiri, I. Nagazi, A. Haddad, *J. Soc. Chim. Tunisie* **2015**, *17*, 128–134.

[10] Y. Kikukawa, K. Ogihara, Y. Hayashi, *Inorganics* **2015**, *3*, 295–308.

[11] A. Müller, E. Krickerneyer, M. Penk, H.-J. Walberg, H. Bögge, *Angew. Chem. Int. Ed.* **1987**, *26*, 1045–1046.

[12] K. Pavani, S. Upreti, A. Ramanan, *J. Chem. Sci.* **2006**, *118*, 159–164.

[13] J. Marrot, K. Barthelet, C. Simonnet, D. Riou, *C. R. Chim.* **2005**, *8*, 971–976.

[14] Y. Hayashi, K. Fukuyama, T. Takatera, A. Uehara, *Chem. Lett.* **2000**, *29*, 770–771.

[15] T. Yamase, M. Suzuki, K. Ohtaka, *J. Chem. Soc., Dalton Trans.* **1997**, 2463–2472.

[16] A. Müller, M. Penk, E. Krickemeyer, H. Bögge, H.-J. Walberg, *Angew. Chem. Int. Ed.* **1988**, *27*, 1719–1721.

[17] A. Müller, R. Rohlfing, J. Döring, M. Penk, *Angew. Chem. Int. Ed.* **1991**, *30*, 588–590.

[18] M. T. Averbuch-Pouchot, A. Durif, *C. R. Acad. Sci. Ser. II* **1994**, *318*, 1067–1072.

[19] A. Pérez-Benítez, S. Bernès, *IUCrData* **2018**, *3*, x181080.

[20] M. Aureliano, N. I. Gumerova, G. Sciortino, E. Garribba, A. Rompel, D. C.

Crans, *Coord. Chem. Rev.* **2021**, *447*, 214143.

[21] D. Rehder, *Angew. Chem. Int. Ed.* **1991**, *30*, 148–167.

[22] D. Liu, Y. Lu, H.-Q. Tan, W.-L. Chen, Z.-M. Zhang, Y.-G. Li, E.-B. Wang, *Chem. Commun.* **2013**, *49*, 3673–3675.

[23] B. Franzetti, G. Schoehn, J.-F. Hernandez, M. Jaquinod, R. W. H. Ruigrok, G. Zaccai, *EMBO J.* **2002**, *21*, 2132–2138.

[24] Bruker, *APEX3, SADAB5, SAINT*, **2016**.

[25] G. M. Sheldrick, *Acta Crystallogr., Sect. A Found. Crystallogr* **2008**, *64*, 112–122.

[26] G. M. Sheldrick, *Acta Crystallogr., Sect. C Struct. Chem.* **2015**, *71*, 3–8.

[27] C. B. Hübschle, G. M. Sheldrick, B. Dittrich, *J. Appl. Crystallogr.* **2011**, *44*, 1281–1284.

[28] A. Takanabe, T. Katsufuji, K. Johmoto, H. Uekusa, M. Shiro, H. Koshima, T. Asahi, *Crystals* **2017**, *7*, 7.

[29] K. Wang, C. Wang, M. K. Mishra, V. G. Young Jr, C. C. Sun, *CrystEngComm* **2021**, *23*, 2648–2653.

[30] E. Tella, A. Trimpalis, A. Tsevis, C. Kordulis, A. Lycourghiotis, S. Boghosian, K. Bourikas, *Catalysts* **2021**, *11*, 322.

[31] A. M. Heyns, M. W. Venter, K.-J. Range, *Z. Naturforsch. B* **1987**, *42*, 843–852.

[32] N. Hu, J. Du, Y.-Y. Ma, W.-J. Cui, B.-R. Yu, Z.-G. Han, Y.-G. Li, *Appl. Surf. Sci.* **2021**, *540*, 148306.

[33] M. Iannuzzi, T. Young, G. S. Frankel, *J. Electrochem. Soc.* **2006**, *153*, B533–B541.

[34] E. Sánchez-Lara, S. Treviño, B. L. Sánchez-Gaytán, E. Sánchez-Mora, M. E. Castro, F. J. Meléndez-Bustamante, M. A. Méndez-Rojas, E. González-Vergara, *Front. Chem.* **2018**, *6*, 402.

[35] H. Ma, X. Meng, J. Sha, H. Pang, L. Wu, *Solid State Sci.* **2011**, *13*, 850–854.

[36] N. C. Sukmana, Sugiarto, Z. Zhang, M. Sadakane, *Z. Anorg. Allg. Chem.* **2021**, *647*, 1930–1937.

CHAPTER 4

Structure and Thermal Transformations of Methylammonium Tungstate

4.1 Introduction

Isopolyoxotungstate is one of the essential and established polyoxometalates.[1] They are used as a building block for polyoxometalate-based compounds, [2–5] a staining reagent,[6] and a precursor for tungsten oxide.[7–9] The synthesis of isopolyoxotungstate is affected by the type and concentration of metal, counter cation, solvent, and pH. Isopolyoxotungstates such as $[W_7O_{24}]^{6-}$, $[H_2W_{12}O_{42}]^{10-}$, $[H_4W_{22}O_{74}]^{12-}$, $[H_{10}W_{34}O_{116}]^{18-}$, $[H_2W_{12}O_{40}]^{6-}$, $[W_{10}O_{32}]^{4-}$, $[W_6O_{19}]^{2-}$, $[H_{12}W_{36}O_{120}]^{12-}$, and $[H_4W_{19}O_{62}]^{6-}$ can be produced via condensation reactions by acidification of $[WO_4]^{2-}$ in an aqueous solution (Scheme 4.1).[4,10–14] The most widely used isopolyoxotungstate compounds are ammonium paratungstate, $(NH_4)_{10}[H_2W_{12}O_{42}]$ and ammonium metatungstate $(NH_4)_6[H_2W_{12}O_{40}]$. Isopolyoxotungstates also can be formed by reacting WO_3 in volatile bases such as NH_3, CH_3NH_2, $(CH_3)_2NH$, and $(CH_3)_3N$ and subsequent drying (Scheme 4.2).[15–19]

Ekeley reported that methylammonium tungstate can be synthesized by dissolving H_2WO_4 in an aqueous methylamine solution and drying at 105 °C, followed by recrystallization.[15] According to that report, the structure of the methylammonium tungstate created by Ekeley's method is heptatungstate. It has been reported that methylammonium tungstate is one of the excellent staining reagents for virus observation.[20–22]

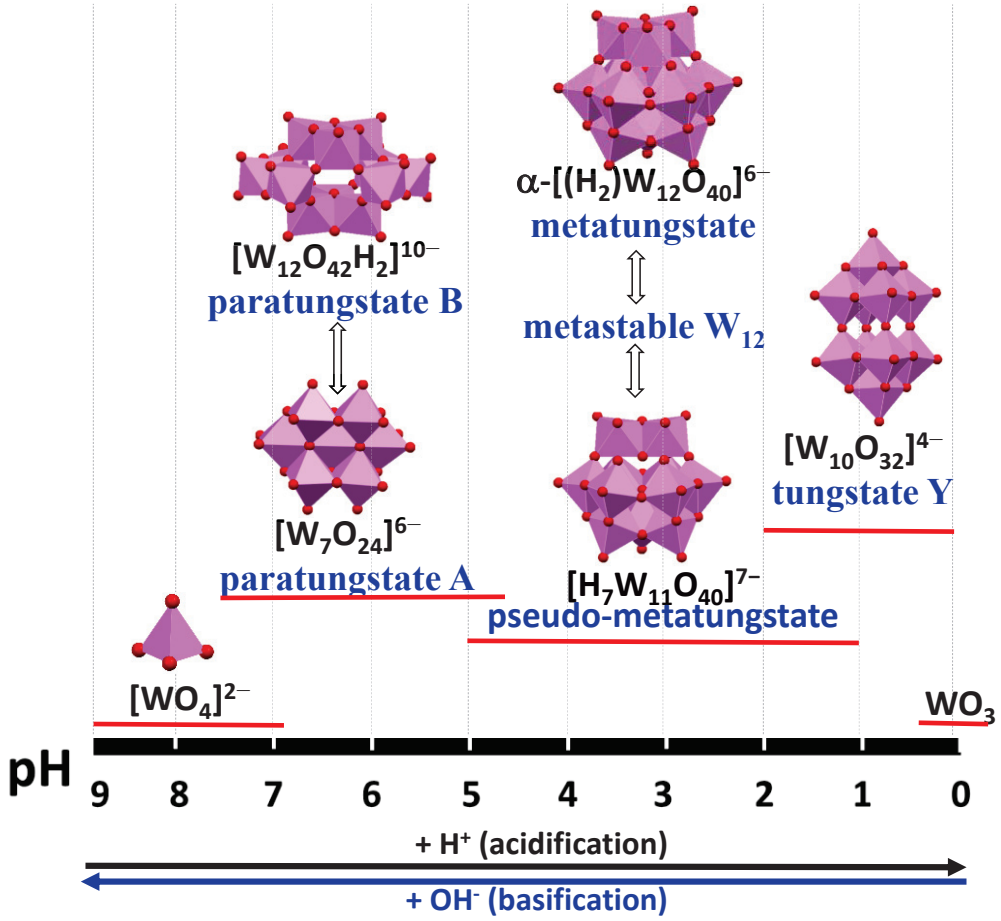

Scheme 4.1. Effect of acidity on the formation of isopolyoxotungstate. Magenta polyhedra are WO_6 octahedra.

Very recently, Morajkar and Srinivasan reported that methylammonium paradodecatungstate, $(CH_3NH_3)_{10}[H_2W_{12}O_{42}]\cdot 12H_2O$ can be produced by slow drying of solution from the reaction mixture of H_2WO_4 with the excess aqueous solution of methylamine at room temperature.[19] These two papers indicate that different molecules $(CH_3NH_3)_6[W_7O_{24}]$ and $(CH_3NH_3)_{10}[H_2W_{12}O_{42}]\cdot 12H_2O$ can be produced by the reaction of WO_3 and CH_3NH_2 with two different isolation methods, one by complete drying at 105 °C and the other by crystallization at room temperature.

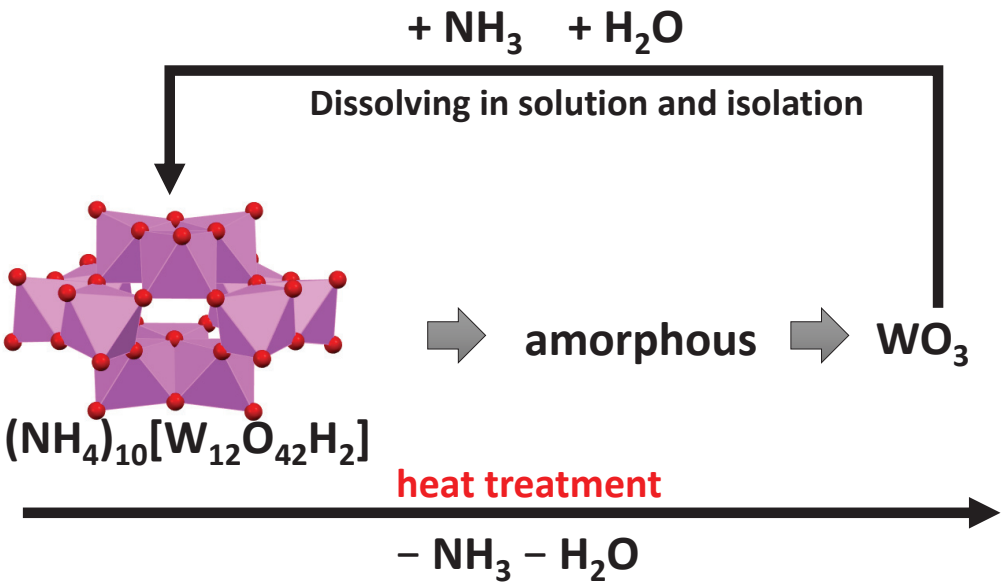

Scheme 4.2. Formation of isopolyoxotungstate by reaction of WO_3 and NH_3 and subsequent heating.

Herein, we present methylammounium paradodecatungstate, $(CH_3NH_3)_{10}[H_2W_{12}O_{42}]\cdot nH_2O$ is produced via drying process of the solution reaction of WO_3 or H_2WO_4 with methylamine solution both at room temperature and up to 150 °C. The crystal packing of methylammonium paradodecatungstate changed as a consequence of drying, the changes are reversible by the addition of water. The second phenomenon we will investigate in this chapter is the structural transformation of methylammonium paradodecatungstate by thermal treatment in the air. The methylammonium paradodecatungstate was stable up to 150 °C, and further heating at 200 °C transformed into an amorphous phase by releasing methylamine and then WO_3 by further heating in air.

4.2 Experimental Section

Materials: All chemicals were of reagent grade and were used without further purification. WO_3 and ethanol were purchased from Wako Pure Chemical Industries, Ltd., and 40% methylamine solution was purchased from Kanto

Chemical Co., Inc. Ammonium metatungstate, ammonium paradodecatungstate, and H_2WO_4 were gifted from Nippon Inorganic Colour & Chemical Co., Ltd.

Preparation of $(CH_3NH_3)_{10}[H_2W_{12}O_{42}]\cdot 3H_2O$. WO_3 (5.2 g, W: 22.5 mmol) or H_2WO_4 (5.63 g, W: 22.5 mmol) was mixed with 5 mL of 40% methylamine solution with a methylamine/W ratio of 2. The mixture was stirred for 30 min and introduced into a 50 mL Teflon-lined stainless-steel autoclave, which was heated at 70 °C for 2 h under static conditions in an electric oven. The resulting mixture was filtered to remove the white solid (3.1 and 1.0 g in the reactions of WO_3 and H_2WO_4, respectively). The solution was heated at 70 °C at atmospheric pressure to remove methylamine and water, and the solid (1.5 and 5.6 g in the reactions of WO_3 and H_2WO_4, respectively) were obtained. The amount of water was detected by TG analysis (weight loss = 3.19%, corresponding to 3 H_2O). Characteristic IR adsorption data, $\tilde{\nu}/cm^{-1}$(KBr): 3400(w), 1596(m), 1505(m), 1470(m), 1416(w), 1296(w), 949(s), 928 (s), 881(s, sh), 852(vs), 817(vs), 761 (s), 736(vs), 702(vs) cm^{-1}. Elemental analysis calcd. for $(CH_3NH_3)_{10}[H_2W_{12}O_{42}]\cdot 3H_2O$: H 2.11, C 3.69, N 4.30; found, H 0.86, C 3.97, N 4.22.

Single crystals of $(CH_3NH_3)_{10}[H_2W_{12}O_{42}]\cdot 12H_2O$. Single crystals of $(CH_3NH_3)_{10}[H_2W_{12}O_{42}]\cdot 3H_2O$ were formed by slow ethanol vapor diffusion. A 0.05 g of solid was dissolved in 0.5 mL of water in a small bottle (2.2 mL) that was then placed in a larger (10 mL) bottle containing 2.5 mL of ethanol. After the large bottle was closed, ethanol slowly diffused into the small bottle. Colorless crystals suitable for single-crystal X-ray structure analysis were obtained after two days.

Calcination of $(CH_3NH_3)_{10}[H_2W_{12}O_{42}]\cdot 3H_2O$. $(CH_3NH_3)_{10}[H_2W_{12}O_{42}]\cdot 3H_2O$ was calcined in air at 100, 150, 200, 250, 300, 350, 400, 450, 500, 550, and 600 °C at a heating rate of 10 °C/min, and the temperature was maintained for 1 h.

Analytical techniques: Powder X-ray diffraction patterns were measured on a Bruker D2 PHASER 2nd Gen using Cu-K_α radiation. The samples were ground and placed on a sample holder, and the XRD profiles were recorded at 2θ = 3–80°. FT-

IR spectra were obtained using a NICOLET 6700 FT-IR spectrometer (Thermo Fischer Scientific) in the range of 650–4000 cm^{-1} in KBr pellets. TG-DTA was carried out using a TG-DTA7300 instrument (SII, Japan) with an air flow of 200 mL s^{-1}. Temperature programmed desorption (TPD) was carried out using a BELCAT II – BELMASS system (MicrotracBEL Corp.) instrument under helium flow. The rate of temperature increase was 10 °C min^{-1} and the maximum temperature was 600 °C. Ultraviolet–visible spectra were obtained using an Agilent 8453 UV-visible spectrometer in the range 190–1100 nm with a cell length of 1 cm. Raman spectra were collected using a Horiba Jovin Yvon T64000 with an Ar^+ 512-nm laser. The power of the laser was adjusted to 40 mW, and each spectrum was collected for 10 s and accumulated three times. The ^{183}W NMR spectrum was recorded on an ECA500 spectrometer (500 MHz, JEOL) at a resonance frequency of 20.839 MHz. The solution for ^{183}W NMR was prepared by dissolving the sample in D_2O. The spectrum was referenced to an external 1 M $Na_2[WO_4]$ (δ = 0 ppm) standard. The powder XRD pattern of the dried solid was indexed using DICVOL06 in Fullprof. After performing Pawley refinement, the most reasonable space group was obtained.

X-ray crystallography. Single-crystal X-ray diffraction data of $(CH_3NH_3)_{10}[H_2W_{12}O_{42}]\cdot 12H_2O$ were collected at 100(2) K on a Bruker SMART APEX2 using Mo K_α radiation (Å = 0.71073 Å) monochromated by a layered confocal mirror. Data reduction and space group determination were carried out using the Bruker APEX 3 suite.[23] Absorption correction was applied using the multi-scan technique (SADABS).[23] The structure was solved by direct methods using SHELXT[24] and was refined using SHELXL[25] using the SHELXle[26] interface. The carbon and nitrogen atoms of the methylammonium cations were located in the electron density map, where the ammonium cations are hydrogen bonded to the anionic cluster. The hydrogen atoms of methylammonium cations were calculated using the riding model, whereas the hydrogen atom on O5 was located in the difference map. One lattice water molecule was disordered over two sites, and the hydrogen atoms were not located. All O–H distances were constrained

to 0.84 Å, and the distance between H atoms in water molecules was fixed at 1.34 Å. All atoms, except hydrogen and a disordered water molecule, were refined anisotropically. CCDC 2082551 contains the supplementary crystallographic data of methylammonium paradodecatungstate, which can be obtained free of charge from the Cambridge Crystallographic Data Centre.

4.3 Results and Discussion

4.3.1 Synthesis

The synthesis reaction procedure was similar to those reported by Ekeley[15] and Srinivasan[19] which reacted WO_3 or H_2WO_4 with aqueous methylamine, (CH_3NH_2) solution at room temperature or 70 °C for 2 h. Details of the synthesis condition were summarized in Table 4.1. WO_3 partially dissolved in excess methylamine at ambient temperature. Therefore, the undissolved solid (solid A) was filtered off. Solid B was then obtained by evaporating the filtrate at 70 °C under atmospheric pressure. By using powder X-ray diffraction (XRD) measurements, a solid (solid A) that did not dissolve in the methylamine solution at room temperature was identified as WO_3 (Figure 4.1(a)). Evaporation of the filtrate (Solid B) gave an XRD pattern indicating the formation of crystalline (Figure 4.1(b)). H_2WO_4 was completely dissolved in the methylamine solution at room temperature with a tungsten/methylamine ratio of 32. When the solution evaporated at 70 °C under air pressure, a white powder was produced (solid C). The powder XRD pattern of solid C is similar to that of solid B (Figure 4.1(c)).

Table 4.1. Reaction conditions and product yield.[a)]

Reaction temp.	WO_3 (g)	H_2WO_4 (g)	Methylamine solution (40%, mL)	Molar ratio (methylamine:W)	Solid obtained after reaction[b)] (g)	Solid obtained after evaporation of the filtrate[c)] (g)
Room temp.	0.07	-	7	209	0.06 (solid A)	0.02 (solid B)
Room temp.	-	0.07	1	32	-	0.10 (solid C)
70 °C	5.22	-	5	2	3.14 (solid D)	1.60 (solid E)
70 °C	-	5.63	5	2	1.04 (solid F)	5.56 (solid G)

a) Reaction performed for 2 h. b) Solid obtained by filtration and subsequent drying at 70 °C. c) Solid obtained by heating to 70 °C.

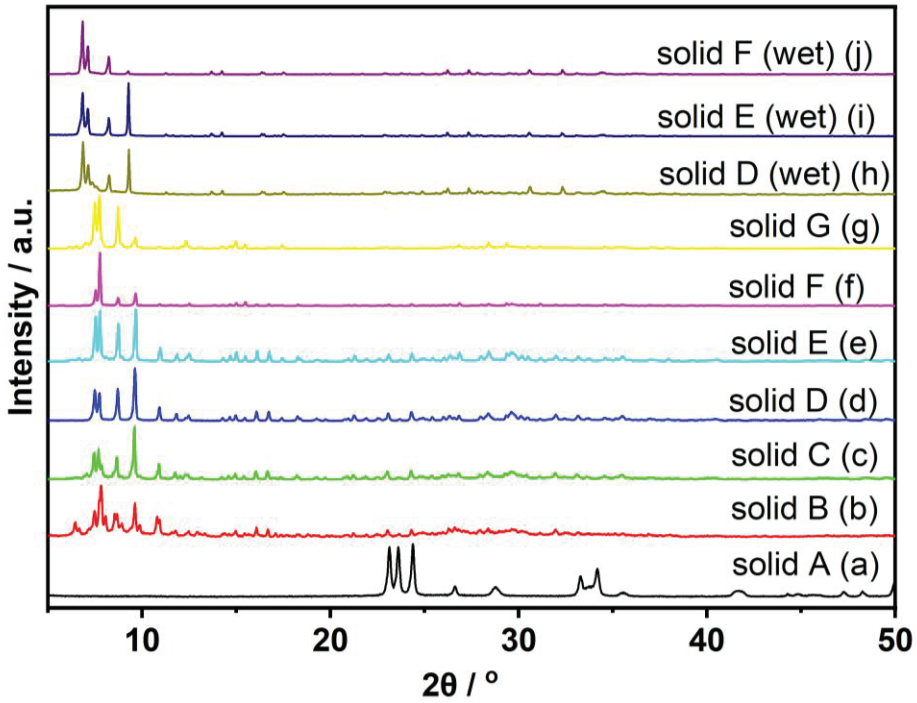

Figure 4.1. XRD pattern of (a) solid A (all peaks were attributed to monoclinic (JCPDS 43-1035) WO_3), (b) solid B, (c) solid C, (d) solid D, (e) solid E, (f) solid F, (g) solid G, (h) solid D (wet), (i) solid E (wet), and (j) solid F (wet).

An alternative procedure involved mixing WO_3 or H_2WO_4 with an aqueous methylamine solution (methylamine/W ratio of 2) for 30 minutes at room temperature in a Teflon beaker. Then the mixture was heated at 70 °C for two hours in a stainless-steel autoclave with a Teflon liner to prevent the evaporation of methylamine and water (closed system). Filtration was used to separate the obtained solid into solids D (wet) and F(wet), which were then dried at 70 °C to create solids D and F. To create a white solid powder, the filtrates were evaporated at 70 °C under air pressure (solids E and G). Additionally, the solid yield that was obtained after the evaporation of filtrate made from H_2WO_4 was higher than WO_3.

The XRD patterns of solids D (wet) (Figure 4.1(h)) and F (wet) (Figure 4.1(j)) differ from those of WO_3 and display peaks at low angles (10°, i.e., d-spacing larger than 8.8), demonstrating the formation of a new crystalline tungstate. The XRD profiles of solids D, E, F, and G (Figure 4.1(d)-(g)), which had been heated at 70

°C, were similar to that of solids B and C, showing that the crystal structures of solids D (wet) and F (wet) had changed as a result of the heating. Additionally, the solid E (wet) powder XRD pattern, which was obtained before the filtrate was completely drying at 70 °C, is comparable to the solids D (wet) and F (wet).

According to these results, the same tungstate species were formed by dissolving H_2WO_4 or WO_3 in an aqueous methylamine solution at room temperature or 70 °C. Solids D (wet) and F (wet) were precipitated by cooling the solution back down to room temperature. Additionally, even if the peak positions in the XRD patterns were similar, the peak intensity ratios were different, probably due to the effects of preferred orientation. The drying process of the wet solid affected the XRD pattern of the powder, indicating that the crystal structures had changed. In order to validate the structural similarities of solids D and E, FT-IR characterization was performed and the results as shown in Figure 4.2.

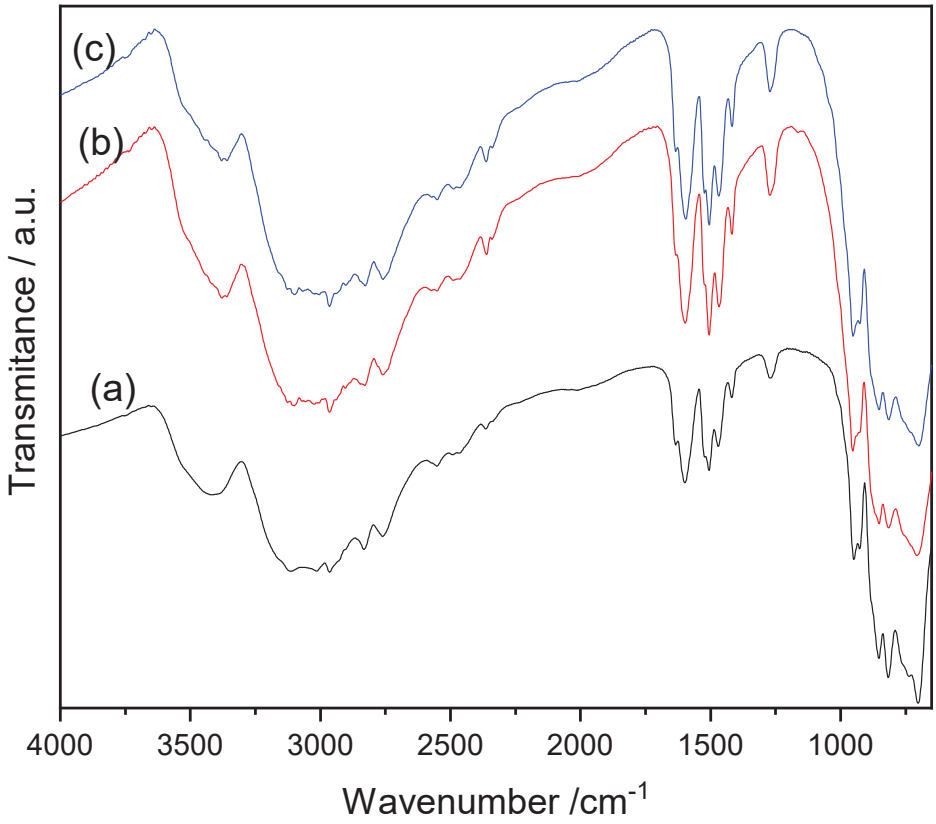

Figure 4.2. FTIR spectra of (a) solid D, (b) solid E, and (c) solid E (wet) (c). Solids D and E were dried at 70 °C. Solid E (wet) was obtained before complete drying.

4.3.2 Crystal structure

Slow ethanol diffusion into an aqueous solution of solid E produced crystals which were suitable for X-ray structure analysis. In accordance with the crystal structure of $(CH_3NH_3)_{10}[H_2W_{12}O_{42}]\cdot 12H_2O$ reported by Morajkar and Srinivasan.[19] $[H_2W_{12}O_{42}]^{10-}$ crystallized in the triclinic space group $P\bar{1}$ with ten methylammonium counter-cations and twelve water molecules (Table 4.2). The paradodecatungstate, $[H_2W_{12}O_{42}]^{10-}$ anion is structurally identical to the anions of $(NH_4)_{10}[H_2W_{12}O_{42}]\cdot 4H_2O$,[27] $(NH_4)_7[Bi(H_2W_{12}O_{42})]\cdot 20H_2O$,[28] and $Na_2(NH_4)_8[H_2W_{12}O_{42}]\cdot 12H_2O$.[29] The $[H_2W_{12}O_{42}]^{10-}$ anion is made up of two HW_3O_{13} groups and two W_3O_{14} groups that are linked together through corner sharing. Three WO_6 octahedral are connected by three edge-sharing in the HW_3O_{13} group (yellow polyhedra in Figure 4.3) and three WO_6 octahedral are connected by two edge-sharing in the W_3O_{14} group (blue polyhedra in Figure 4.3).

Table 4.2 Crystal data for $(CH_3NH_3)_{10}[H_2W_{12}O_{42}]\cdot 12H_2O$.

Empirical formula	$C_{10}H_{86}N_{10}O_{54}W_{12}$
Formula weight (g/mol)	3416.9
Temperature (K)	100(2)
Crystal system	Triclinic
Space group	$P\bar{1}$
a (Å)	9.4933(6)
b (Å)	13.0547(8)
c (Å)	13.5615(5)
α (°)	107.630(1)
β (°)	90.464(1)
γ (°)	93.406(1)
V (Å^3)	1598.34(17)
Z	2
$D_{calcd.}$ (g/cm^{-3})	3.542
μ (mm^{-1})	21.605
Radiation	Mo Kα (λ =0.71073 Å)
F(000)	1528
Crystal size (mm^3)	0.11 × 0.08 × 0.06
2Θ range	3.152 to 55.79°
Index ranges	$-12 \le h \le 12$ $-17 \le k \le 17$ $-17 \le l \le 17$
No. of reflection collected	19091
No. of unique reflections	7496 (R_{int} = 0.027)
Data/restraints/parameters	7496/76/424
G.O.F.	1.052

R indexes [$I > 2\sigma(I)$]	$R_1 = 0.0205$; $wR_2 = 0.0425$
R indexes [all data]	$R_1 = 0.0247$; $wR_2 = 0.0436$
$(\Delta/\sigma)_{max}$	0.003
$(\Delta\rho)_{max/min}$ (e Å^{-3})	0.955/−1.831

$[H_2W_{12}O_{42}]^{10-}$ anion is formed as a cluster with a two-proton in the central cavity. Bond valence sum calculations on the O atom proved that two equivalent oxygens $O5_{c1}$ were one-proton protonated (Figure 4.4 and Tables 4.3). In the W_3O_{14} group, each W atom has two terminal oxygens (O_a), whereas each W in the HW_3O_{13} group only has one. There are two different ways that oxygen can connect two W atoms (O_b): O_{b1} uses corner-sharing to connect two W in the same HW_3O_{13} and W_3O_{14} groups, while O_{b2} uses oxygen to connect two W in different HW_3O_{13} and W_3O_{14} groups. The third oxygen group is the bridging oxygen connecting three W atoms (O_c). There are two types of O_c: O_{c1} bridges three W atoms only in the HW_3O_{13} group, whereas O_{c2} bridges three W atoms between the HW_3O_{13} and W_3O_{14} groups (Figure 4.4). Through bond valence sum calculations, it has been confirmed that W is in the +VI oxidation state (Table 4.4).

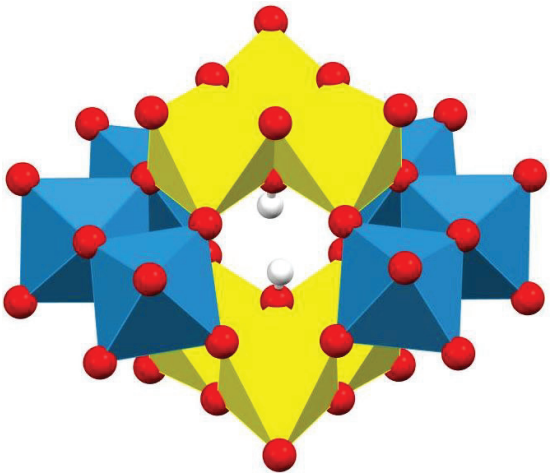

Figure 4.3. Polyhedral representation of the $[H_2W_{12}O_{42}]^{10-}$ anion. (HW_3O_{13} groups, yellow polyhedra; W_3O_{14} groups, blue polyhedra).

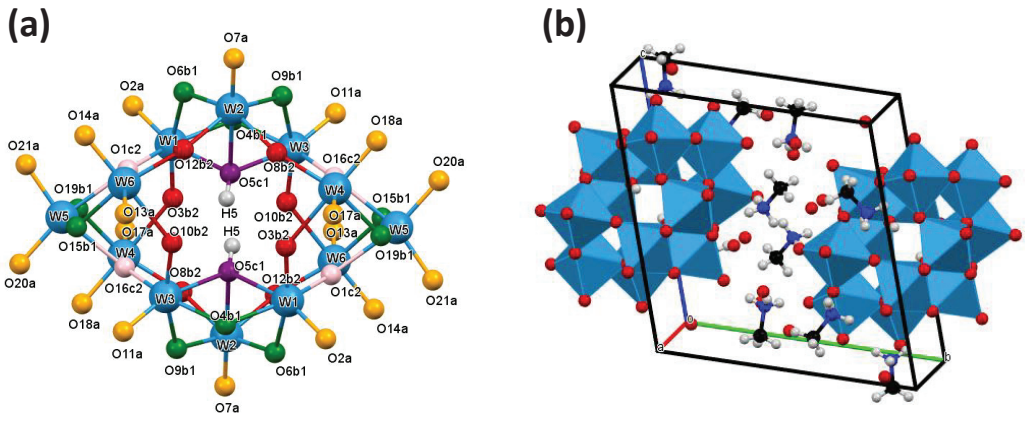

Figure 4.4. Molecular structure of the $[H_2W_{12}O_{42}]^{10-}$ anion (a) and packing of molecules in crystal lattice (b). W, blue; H, grey; O_a, terminal oxygen, orange; O_{b1}, bridges two W atoms in the same group, green; O_{b2}, bridges two W atoms between the different groups, red; O_{c1}, bridges three W atoms in the same group, purple; and O_{c2}, bridges three W atoms between the different groups, pink.

Table 4.3. Bond valance sum (BVS) calculations of O atoms in $(CH_3NH_3)_{10}[H_2W_{12}O_{42}]\cdot 12H_2O$.

Bonds	Bond length (Å)	Bond valence [a]	BVS [b]	Assigned state
$O1_{c2}$-W1	1.917	1.0000	1.8364	O^{2-}
$O1_{c2}$-W5	2.267	0.3883		
$O1_{c2}$-W6	2.214	0.4481		
$O2_a$-W1	1.728	1.6666	1.6666	O^{2-}
$O3_{b2}$-W1	1.798	1.3794	1.8360	O^{2-}
$O3_{b2}$-W4	2.207	0.4567		
$O4_{b1}$-W1	1.945	0.9271	1.8222	O^{2-}
$O4_{b1}$-W3	1.958	0.8951		
$O5_{c1}$-W1	2.233	0.4257	1.2359	OH^-
$O5_{c1}$-W2	2.262	0.3936		
$O5_{c1}$-W3	2.241	0.4166		
$O6_{b1}$-W1	2.121	0.5762	1.7618	O^{2-}
$O6_{b1}$-W2	1.854	1.1856		
$O7_a$-W2	1.737	1.6266	1.6266	O^{2-}
$O8_{b2}$-W2	1.962	0.8855	1.9788	O^{2-}
$O8_{b2}$-W4	1.884	1.0933		
$O9_{b1}$-W2	1.858	1.1729	1.8271	O^{2-}
$O9_{b1}$-W3	2.074	0.6542		

$O10_{b2}$-W3	1.79	1.4095	1.8552	O^{2-}
$O10_{b2}$-W6	2.216	0.4457		
$O11_a$-W3	1.735	1.6354	1.6354	O^{2-}
$O12_{b2}$-W2	1.96	0.8903	2.0014	O^{2-}
$O12_{b2}$-W6	1.878	1.1112		
$O13_a$-W6	1.763	1.5162	1.5162	O^{2-}
$O14_a$-W6	1.735	1.6354	1.6354	O^{2-}
$O15_{b1}$-W5	1.88	1.1052	2.0076	O^{2-}
$O15_{b1}$-W6	1.955	0.9024		
$O16_{c2}$-W3	1.91	1.0191		
$O16_{c2}$-W4	2.235	0.4234	1.8625	O^{2-}
$O16_{c2}$-W5	2.238	0.4200		
$O17_a$-W4	1.736	1.6310	1.6310	O^{2-}
$O18_a$-W4	1.762	1.5203	1.5203	O^{2-}
$O19_{b1}$-W4	1.955	0.9024	1.8890	O^{2-}
$O19_{b1}$-W5	1.922	0.9866		
$O20_a$-W5	1.748	1.5789	1.5789	O^{2-}
$O21_a$-W5	1.757	1.5410	1.5410	O^{2-}

[a] $S_{ij} = \exp\left(\frac{R_0 - R_{ij}}{B}\right)$

[b] $V_i = \sum S_{ij}$

Here,
V_i: oxidation state of atom i, S_{ij}: bond valence, R_0: empirically determined cation-anion distance, R_{ij}: length ofcation–anion bond, and B: universal parameter (0.37).

Table 4.4. BVS calculations of W atoms in $(CH_3NH_3)_{10}[H_2W_{12}O_{42}]\cdot 12H_2O$.

Bonds	**Bond length (Å)**	**Bond valence [a]**	**BVS [b]**	**Assigned state**
W1-$O2_a$	1.728	1.6666	5.9750	W^{6+}
W1-$O3_{b2}$	1.798	1.3794		
W1-$O1_{c2}$	1.917	1.0000		
W1-$O4_{b1}$	1.945	0.9271		
W1-$O6_{b1}$	2.121	0.5762		
W1-$O5_{c1}$	2.233	0.4257		
W2-$O7_a$	1.737	1.6266	6.1545	W^{6+}
W2-$O6_{b1}$	1.854	1.1856		
W2-$O9_{b1}$	1.858	1.1729		
W2-$O12_{b2}$	1.96	0.8903		
W2-$O8_{b2}$	1.962	0.8855		
W2-$O5_{c1}$	2.262	0.3936		
W3-$O11_a$	1.735	1.6354	6.0299	W^{6+}

W3-O10$_{b2}$	1.79	1.4095		
W3-O16$_{c2}$	1.91	1.0191		
W3-O4$_{b1}$	1.958	0.8951		
W3-O9$_{b1}$	2.074	0.6542		
W3-O5$_{c1}$	2.241	0.4166		
W4-O17$_{a}$	1.736	1.6310	6.0271	W^{6+}
W4-O18$_{a}$	1.762	1.5203		
W4-O8$_{b2}$	1.884	1.0933		
W4-O19$_{b1}$	1.955	0.9024		
W4-O3$_{b2}$	2.207	0.4567		
W4-O16$_{c2}$	2.235	0.4234		
W5-O20$_{a}$	1.748	1.5789	6.0200	W^{6+}
W5-O21$_{a}$	1.757	1.5410		
W5-O15$_{b1}$	1.88	1.1052		
W5-O19$_{b1}$	1.922	0.9866		
W5-O16$_{c2}$	2.238	0.4200		
W5-O1$_{c2}$	2.267	0.3883		
W6-O14$_{a}$	1.735	1.6354	6.0590	W^{6+}
W6-O13$_{a}$	1.763	1.5162		
W6-O12$_{b2}$	1.878	1.1112		
W6-O15$_{b1}$	1.955	0.9024		
W6-O1$_{c2}$	2.214	0.4481		
W6-O10$_{b2}$	2.216	0.4457		

[a] $S_{ij} = \exp\left(\frac{R_0 - R_{ij}}{B}\right)$

[b] $V_i = \sum S_{ij}$

Here,
V_i: oxidation state of atom i, S_{ij}: bond valence, R_0: empirically determined cation–anion distance, R_{ij}: length of cation–anion bond, and B: universal parameter (0.37).

The wet solids (solids D (wet), F (wet), and E (wet)) exhibit powder XRD profiles that were similar to the simulated powder XRD obtained from single-crystal X-ray data (Figure 4.5), proving that they have the same crystal structure as that determined through single-crystal structure analysis. The preferred orientation of the powder sample may be the cause of the differences in peak intensities between the simulated and experimental data.

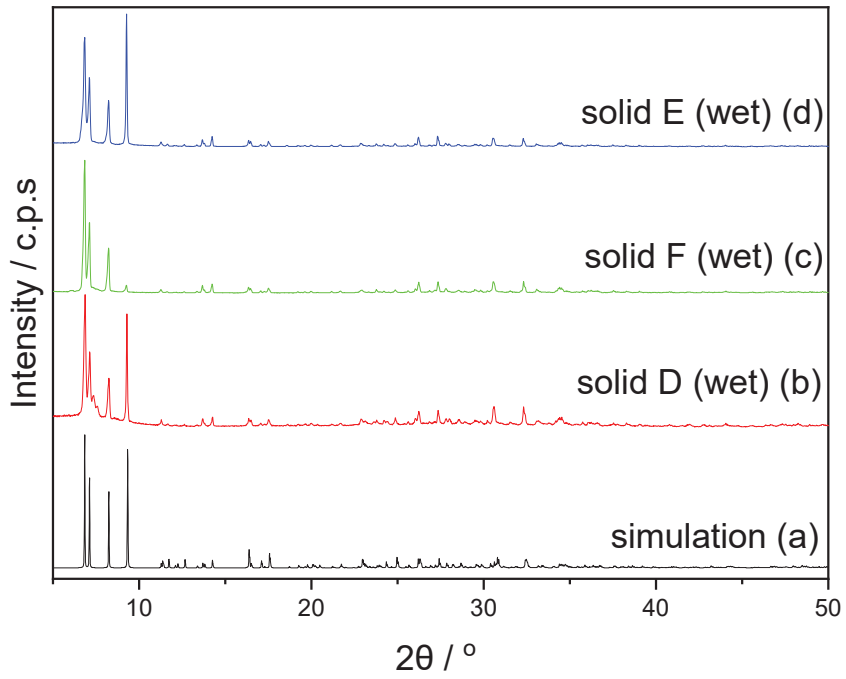

Figure 4.5. Simulated XRD patterns obtained using the single-crystal structure of $(CH_3NH_3)_{10}[H_2W_{12}O_{42}]\cdot 12H_2O$ (a), experimental XRD patterns of solids D (wet) (b), F (wet), and E (wet) (d).

4.3.3 Characterization of dried solids

Figure 4.2(b) and (c) show FT-IR spectra of methylamonium paradodecatungstate in both dry and wet conditions. Based on that figure, the spectra shape of both component were similar, indicating that the drying process at 70 °C does not alter the structure of methylammonium paradodecatungstate.The transmittance bands at 1269, 1416, and 1470 cm^{-1} in the FT-IR spectrum of dry solid E (Figure 4.6) correspond to CH_3-NH_3^+ rocking, CH_3^+ bending, and NH_3^+ bending, respectively. Furthermore, a vibration band at 1505 cm^{-1} that is associated with the NH_3^+ deformation vibration was observed.[30,31] These bands are characteristic of the bonds in the methylammonium counter cation. The bands at 1596 and 3400 cm^{-1} are attributed to O-H bond vibrations of ligated or lattice H_2O. By comparing the IR spectrum of dimethylammonium paradodecatungstate as reported by the Kótai group,[32] it can be determined that the bands at 949 and 928 cm^{-1} correspond to the vibrations of W=O and $W(=O)_2$, respectively, and those at

881, 852, and 817 cm^{-1} to the vibration of edge-sharing W-O-W. The bands below 1000 cm^{-1} are similar to those reported for the paradodecatungstate anion in dimethylammonium paradodecatungstate[32] and ammonium paradodecatungstate,[33] and but different from those of heptatungstate, $[W_7O_{24}]^{6-}$ and metatungstate, $[H_2W_{12}O_{40}]^{6-}$ (Figure 4.6(c)).[34]

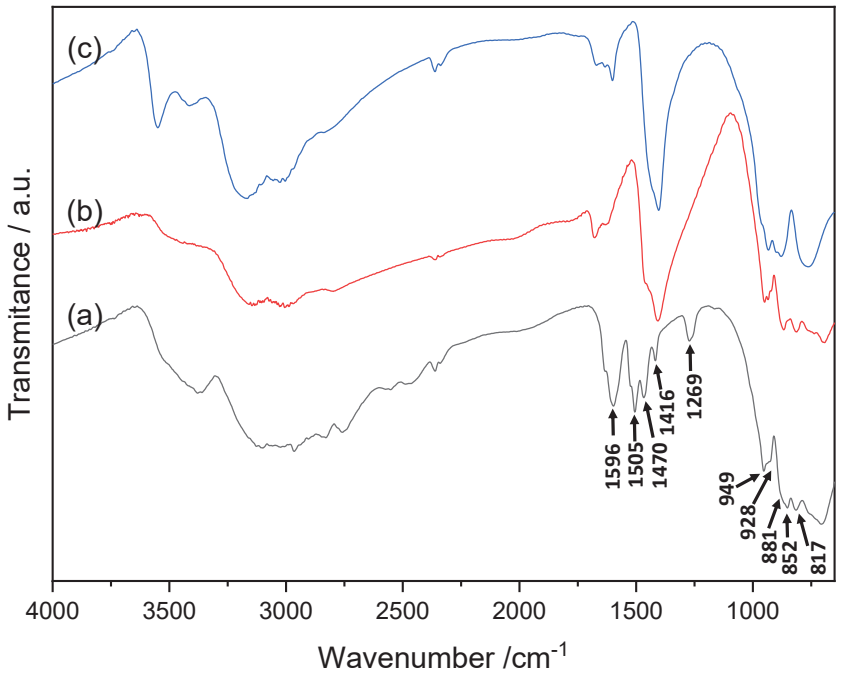

Figure 4.6. FT-IR spectra of solid E (methylammonium paradodecatungstate, $(CH_3NH_3)_{10}[H_2W_{12}O_{42}]$ after heating at 70 °C (a), ammonium paradodecatungstate, $(NH_4)_{10}[H_2W_{12}O_{42}]$ (b), and ammonium metatungstate, $(NH_4)_6[H_2W_{12}O_{40}]$ (c).

Raman spectroscopy was also used to confirm that the dried solids contained the paratungstate structure. Figure 4.7 shows the Raman spectrum of dried solid E together with those of methylamine hydrochloride and ammonium paradodecatungstate. The observed band around 950 and 860 cm^{-1} was attributed to the symmetric stretching of W=O bonds and the asymmetric stretching of W=O bonds.[35] In addition, the band at 694, 645, and 569 cm^{-1} are related to the stretching W-O-W bonds. The bands at 394, 355, and 344 cm^{-1} are seen as the deformation mode of the $W(=O)_2$ group.[32] The spectrum of methylammonium

paradodecatungstate is similar to that of ammonium paradodecatungstate, and the observed differences are related to the methylammonium bands. The Raman bands that indicate the presence of methylammonium as a counter-cation of paradodecatungstate anion were observed at 1578, 1467, and 1004 cm^{-1} assigned to NH_3 asymmetric bending, CH_3 asymmetric bending, and C-N stretching vibrations, respectively.

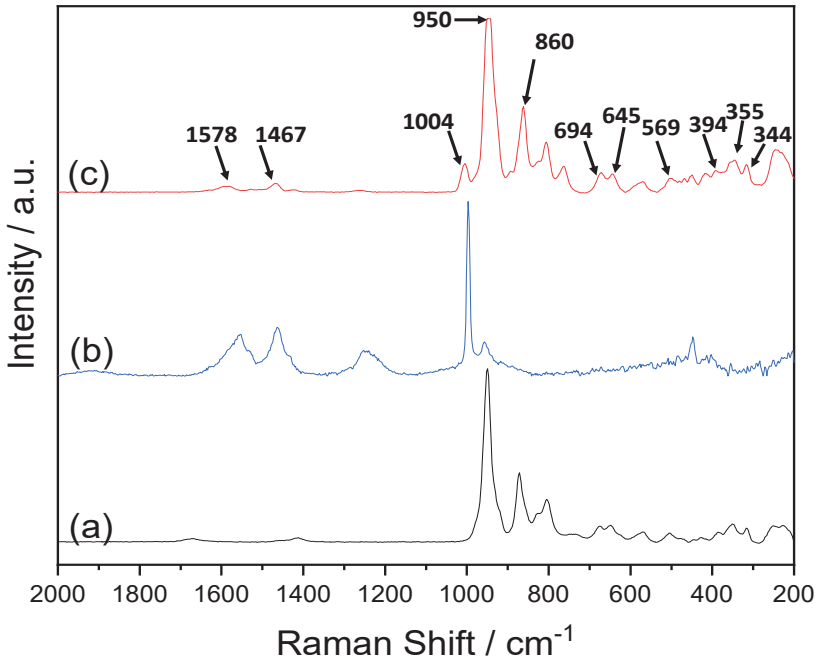

Figure 4.7. Raman spectra of ammonium paradodecatungstate, $(NH_4)_{10}H_2W_{12}O_{42}$ (a), methylamine hydrochloride, $CH_3NH_3^+Cl^-$ (b), and solid E (methylammonium paradodecatungstate), $(CH_3NH_3)_{10}[H_2W_{12}O_{42}]$ (c).

Another crystalline substance comprising $[H_2W_{12}O_{42}]^{10-}$ was formed by drying the wet materials at 70 °C without causing any decomposition. Importantly, the FT-IR spectra of wet and dry materials were comparable. Thus, drying did not affect the molecular structure of methylammonium paradodecatungstate.

The XRD pattern of the dried solid was indexed, and the symmetry and cell dimensions were calculated using Fullprof. Figure 4.8 demonstrates the good agreement between the experimentally obtained pattern and the simulated pattern

of the dried solid. The space group was found to be triclinic $P\bar{1}$ (a = 12.9207, b = 12.2643, c = 9.4324 Å, α= 85.6309°, β= 102.6603°, γ = 110.7095°).

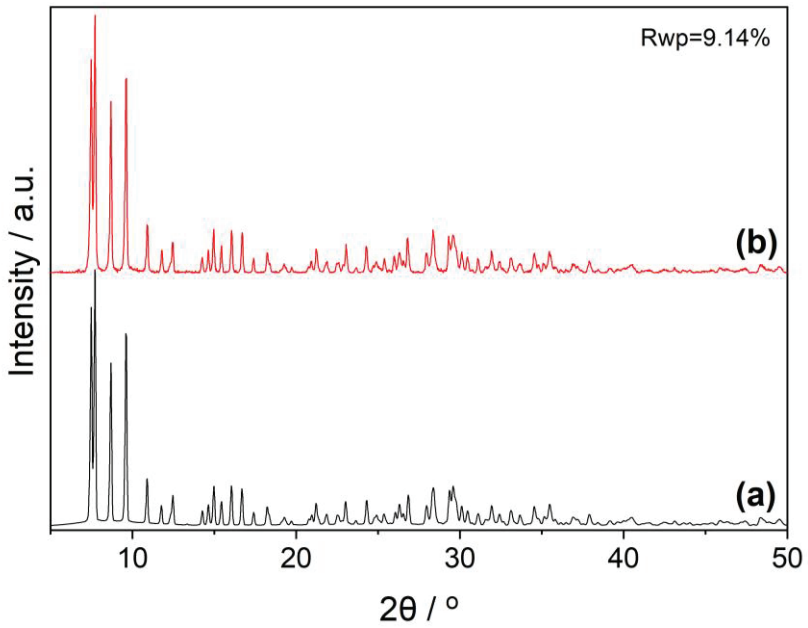

Figure 4.8. Simulated X-ray diffraction (a) obtained by Pawley method and (b) experimental pattern of methylammonium paradodecatungstate (solid E) dried at 150 °C.

The difference between the unit cell volume of the dried solid (1364.11 Å^3) and the wet solid (1598.34 Å^3) indicates that some crystal water molecules were lost during drying. The release of water causes decreasing unit cell volume of dried solid. Recently, dimethylammonium tungstate was found to undergo a similar change in the unit cell parameter with a change in the amount of lattice water molecules.[18] However, we were unable to acquire the precise crystal structure using Rietveld analysis. Additionally, by introducing a small amount of water, the powder XRD pattern of the dried solid was able to return to that of the wet solid (Figure 4.9), indicating the reversibility of the crystal structure change caused by the addition and release of water.

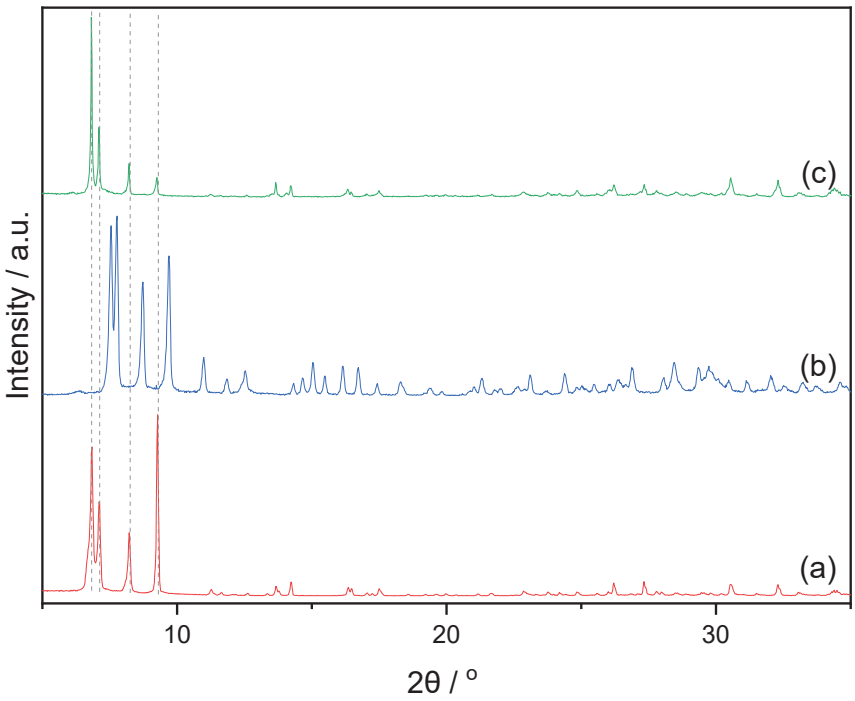

Figure 4.9. XRD patterns of solid E (wet) before drying at 70 °C (a), solid E dried at 70 °C (b), and the wet sample obtained by adding water to dried solid E (c).

In addition, UV-Vis and ^{183}W NMR spectroscopy were used to confirm the structure of $[H_2W_{12}O_{42}]^{10-}$ in water. The UV-vis spectra of methylammonium paradodecatungstate, ammonium paradodeecatungstate, and ammonium metatungstate were measured between 190 and 1100 nm in an aqueous solution (Figure 4.10). The methylammonium paradodecatungstate spectrum shows two characteristic absorptions for the ligand-to-metal charge transfer in the polyanions. The p_π (O_d) → d_{π^*} (W) transitions were given a strong absorption at 194 nm. The absorption of about 250 nm is attributed to p_π ($O_{b,c}$) → d_{π^*} (W) charge transfer transition in the tricentric bonds of POMs.[36,37] These results are in agreement with UV-vis measurements of ammonium paradodecatungstate that have been reported.[36] In addition to the band at 194 nm, only ammonium metatungstate showed absorption at 257 nm associated with metatungstate, $[H_2W_{12}O_{40}]^{6-}$.[43]

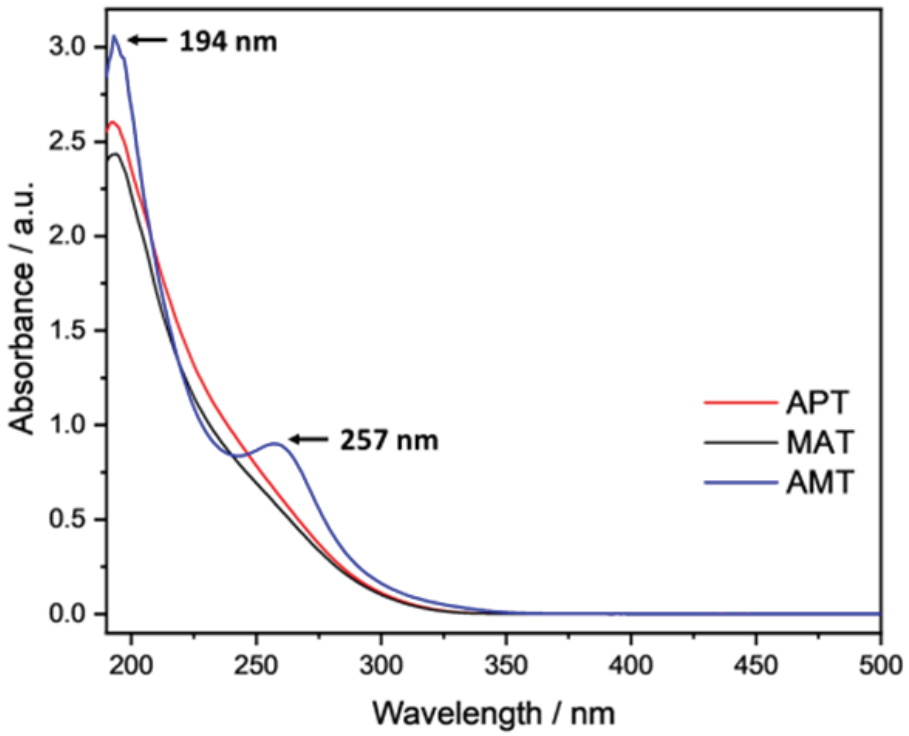

Figure 4.10. UV-vis spectra of solution of solid E (black), ammonium paradodecatungstate (red), and ammonium metatungstate (blue). Solution concentrations: 0.004 wt% (0.002 g/50 mL H_2O).

Figure 4.11 shows the ^{183}W NMR spectrum of methylammonium paradodecatungstate in D_2O. The spectrum shows four singlets with estimated integration ratios of 2:1:1:2 at −94.24, −97.73, −99.20, and −117.55 ppm. These resonances correspond to the structure of the $[H_2W_{12}O_{42}]^{10-}$ anion.[39] In addition, three singlets corresponding to $[W_7O_{24}]^{6-}$ were seen at 271.32, −84.71, and −172.06 ppm with an intensity ratio of 1:4:2. The presence of $[W_7O_{24}]^{6-}$ can be explained by (1) a small amount of $[W_7O_{24}]^{6-}$ being present in the solid and/or (2) the $[W_7O_{24}]^{6-}$ being in equilibrium between $[H_2W_{12}O_{42}]^{10-}$ and $[W_7O_{24}]^{6-}$ in aqueous solution.[40] It has been reported that $[W_7O_{24}]^{6-}$ is stable in solution, but $[H_2W_{12}O_{42}]^{10-}$ crystallizes from solution.[14] However, we are uncertain if $[W_7O_{24}]^{6-}$ is present in the solid. Nevertheless, $[H_2W_{12}O_{42}]^{10-}$ is the main substance in both solid and liquid solutions. These results suggest that the white solids produced by dissolving WO_3 and H_2WO_4 in aqueous methylamine solution and

subsequent drying are both methylammonium paratungstate, $(CH_3NH_3)_{10}[H_2W_{12}O_{42}]$, which was stable after drying at 70 °C.

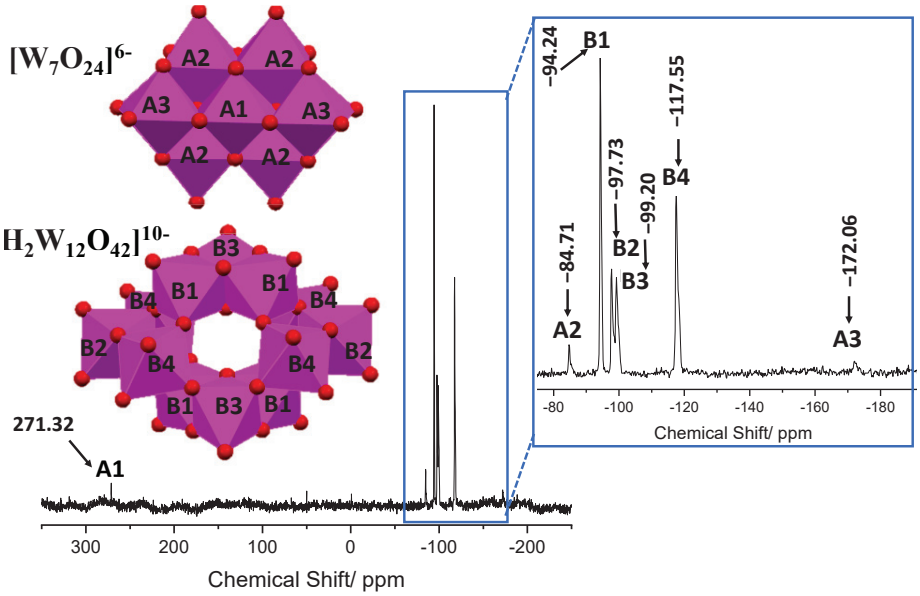

Figure 4.11. ^{183}W NMR spectrum of $(CH_3NH_3)_{10}[H_2W_{12}O_{42}]\cdot 3H_2O$ in D_2O.

4.3.4 Thermal transformation of $(CH_3NH_3)_{10}[H_2W_{12}O_{42}]\cdot 12H_2O$ in air

Four weight loss steps during calcination of solid E (wet) in air flow can be observed in the thermogravimetry (TG) and differential thermal analysis (DTA) curves (Figure 4.12): the first (up to about 100 °C) and second (between about 190 and 250 °C) weight losses were accompanied by endothermic heat flow, whereas the third (about 300 °C) and fourth (about 460 °C) weight losses were accompanied by exothermic heat flow. The multiple decompositions imply that the molecule releases water and methylamine in several stages. The results are in agreement with the TG-DTA of dimethylammonium dihydrogendodecatungstate hydrates that decomposition processes were found to be endothermic below 300 °C and exothermic above 300 °C.[41] The first loss of weight can be attributed to the release of water. This weight loss (16.7%) is higher than the number of lattice water molecules calculated from the single-crystal data and corresponds to 36 mol of crystal water in 1 mol of methylammonium paradodecatungstate. Water in the crystal and on the surface of the powder are both detected by TG analysis, which

cannot be observed by single-crystal XRD measurements. The TG-DTA curves of the sample dried at 70 °C are shown in Figure 4.13. The 1.7% weight loss in the first step corresponds to three lattice water molecules. The difference in these values may be due to the release of lattice water by drying at 70 °C. The effect of the loss of lattice water was discussed earlier (Figure 4.9).

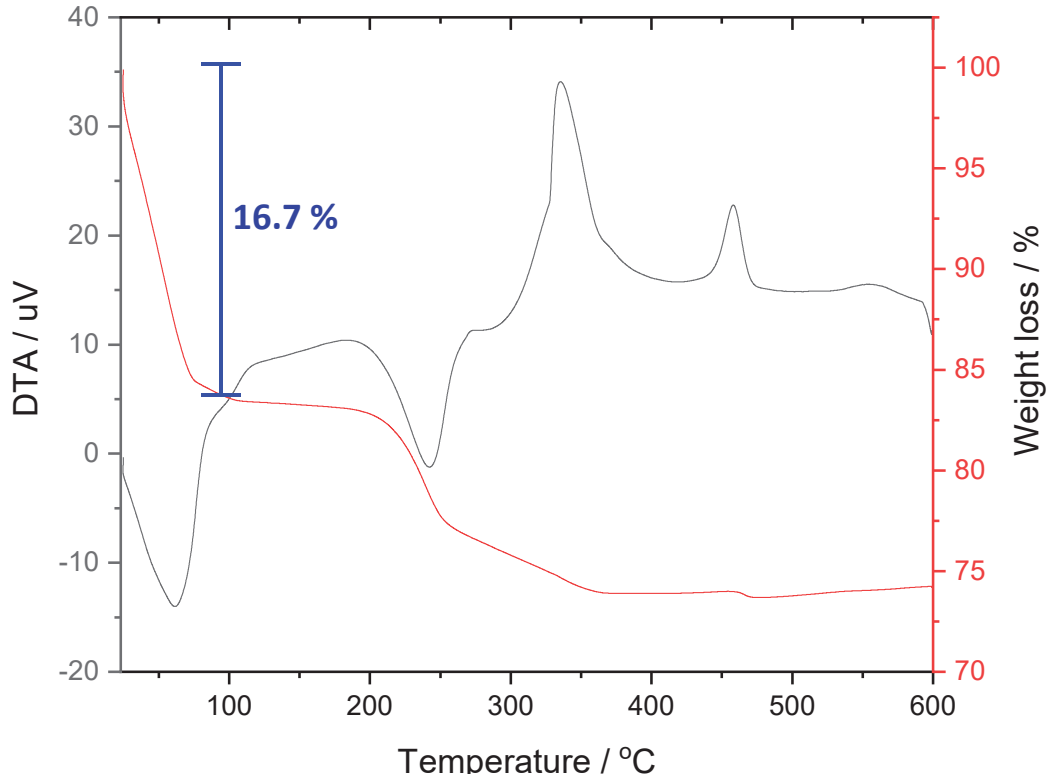

Figure 4.12. TG/DTA curves of solid E (wet) in air flow.

Figure 4.14 shows the TG/DTA under nitrogen flow and temperature programmed desorption-mass spectrometry (TPD-MS) curves of solid E, $(CH_3NH_3)_{10}[H_2W_{12}O_{42}]\cdot 3H_2O$, under helium flow. Several gases with m/z values of 44, 31, 30, 28, 18, 17, and 16 were observed. CH_3NH_2 shows *m/z* of 30, 31, and 28 with an intensity ratio of 100/65/54; H_2O shows *m/z* of 18, 17, and 16 with an intensity ratio of 100/21/1; NH_3 shows *m/z* of 17 and 16 with an intensity ratio of 100/80; CO_2 shows *m/z* of 44, 28, and 16 with an intensity ratio of 100/10/10; CO shows *m/z* of 28 and 16 with an intensity ratio of 100/3; N_2O shows *m/z* of 44, 30, 28, and 16 with an intensity ratio of 100/31/11/5; NO show *m/z* 30 and 16 with an

intensity ratio of 100/3; and N_2 shows *m/z* of 28. TPD-MS spectra revealed that only H_2O desorption was observed at temperatures below 150 °C, indicating that methylammonium as a counter-cation was not desorbed at this temperature. By increasing temperature, along with the desorption of H_2O (*m/z* = 18) and CH_3NH_2 (*m/z* =31), the degradation and oxidized products such as NH_3, CO, CO_2, N_2, NO, NO_2, and/or N_2O may be also observed. A redox reaction between methylammonium and W=O has occurred, as evidenced by the creation of the degradation and oxidized products. The Kótai group found similar oxidation and degradation of dimethylammonium dihydrogendodecatungstate hydrates.[41]

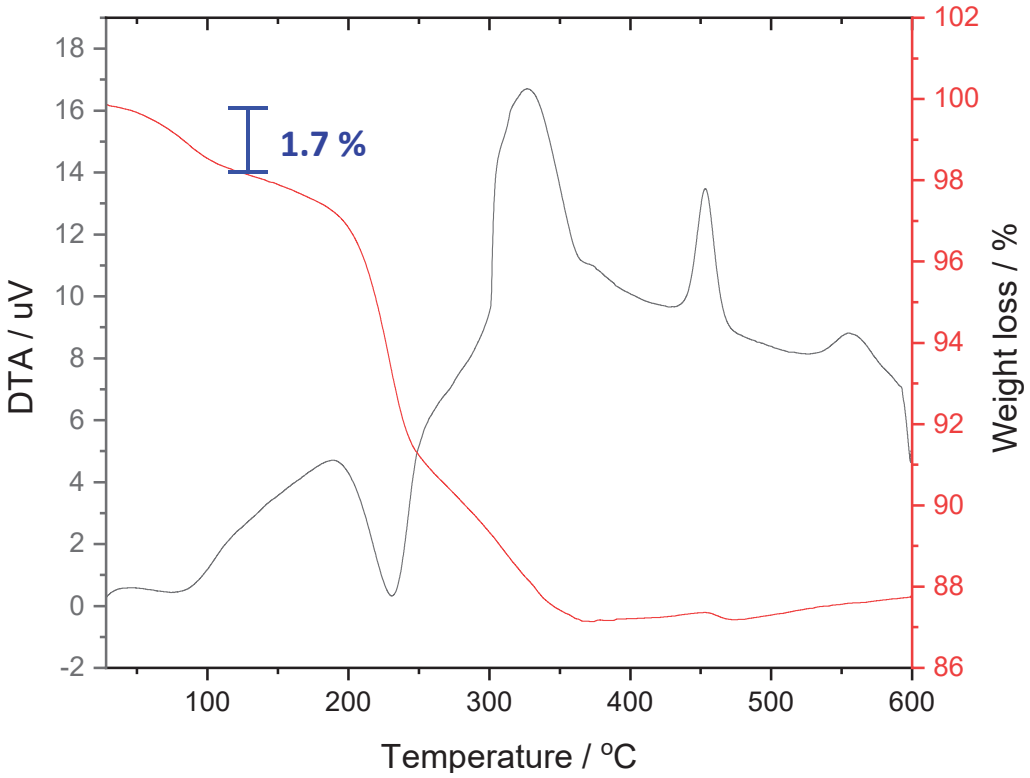

Figure 4.13. TG-DTA curves of solid E dried at 70 °C under air flow.

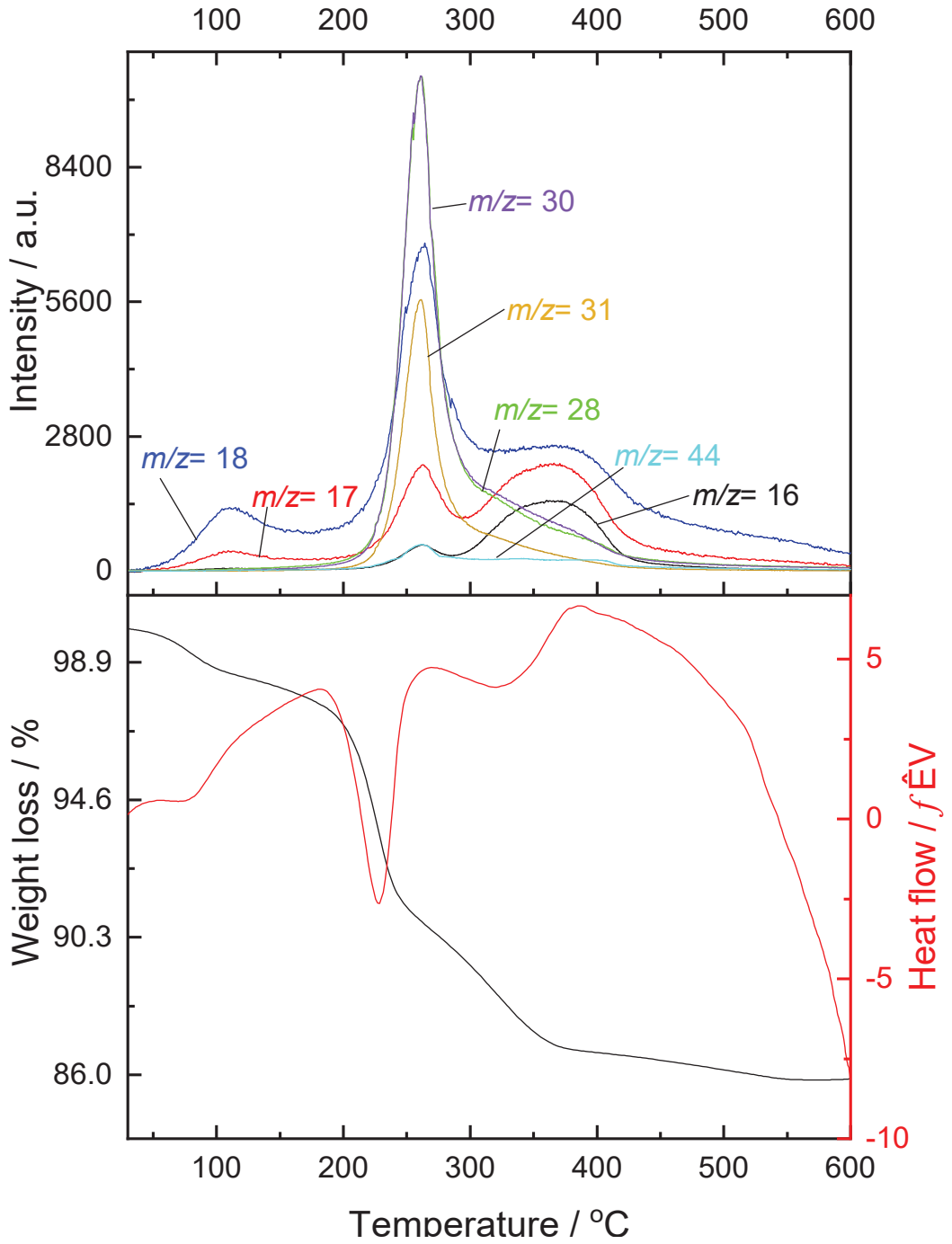

Figure 4.14. TG/DTA curves (bottom) and TPD-MS profile (top) of solid E ($(CH_3NH_3)_{10}[H_2W_{12}O_{42}]\cdot 3H_2O$).

Results of the FTIR measurement for the heated methylammonium paradodecatungstate are shown in Figure 4.15. When the temperature exceeded 200

°C, the intensity of the FTIR bands for H_2O and CH_3NH_2 started to decrease, suggesting that water and methylammonium were released as the heating temperature was increased and were fully removed at 400 °C. These results are consistent with the results of the TG-MS analysis. The FTIR results also suggest that the $[H_2W_{12}O_{42}]^{10-}$ structure is stable at temperatures up to 150 °C.

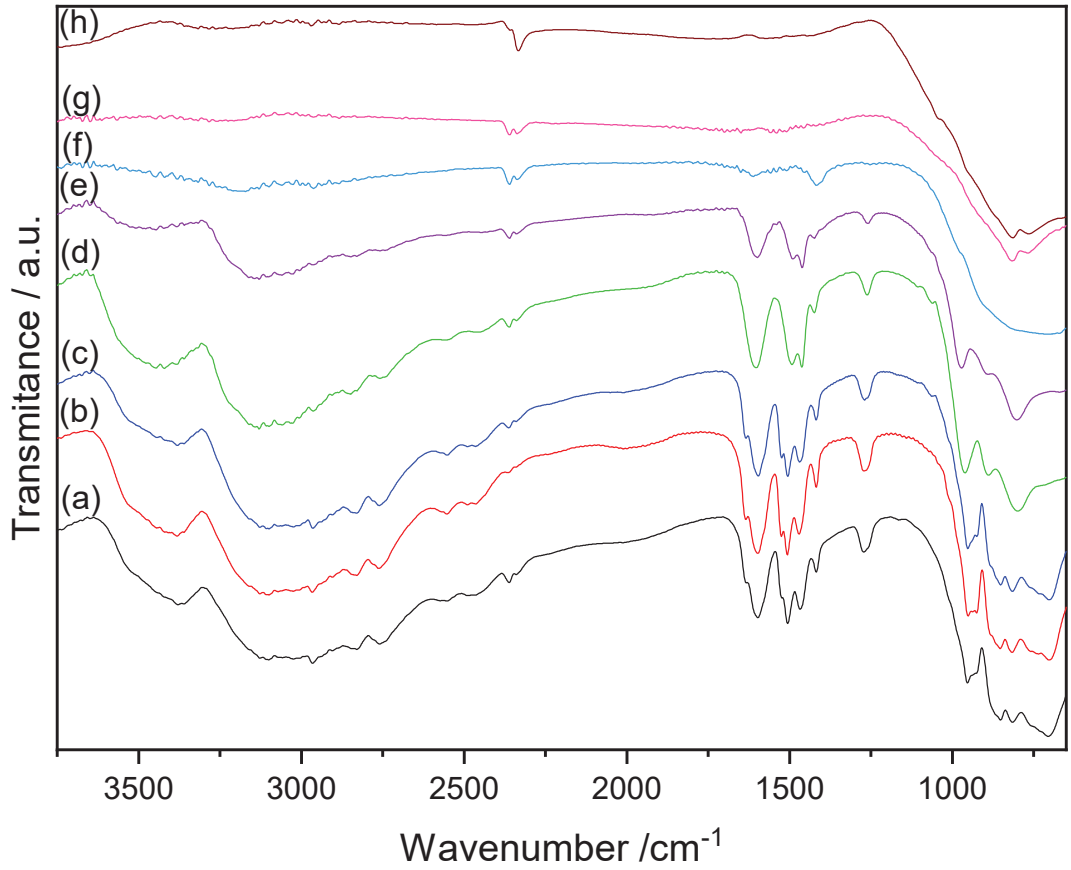

Figure 4.15. FTIR spectra of solid E (a) calcined at 100 (b), 150 (c), 200 (d), 250 (e), 300 (f), 350 (g), and 600 °C (h).

Figure 4.16 shows XRD patterns of heated methylammonium paradodecatungstate. After heating the sample above 200 °C, the primary peaks corresponding to methylammonium paradodecatungstate disappeared, and the release of water and methylamine from the sample resulted in the formation of amorphous species. The monoclinic WO_3 was produced by further heating the amorphous species to 350 °C. As seen in the heat-driven transformation of

ammonium paradodecatungstate at about 400 °C, there was no formation of hexagonal WO_3.[33,42] In Scheme 4.3, the thermal transformation of methylammonium paradodecatungstate is shown. These results indicate that the methylammonium paratungstate $(CH_3NH_3)_{10}[H_2W_{12}O_{42}]$ was stable up to 150 °C but that further heating resulted in the formation of WO_3.

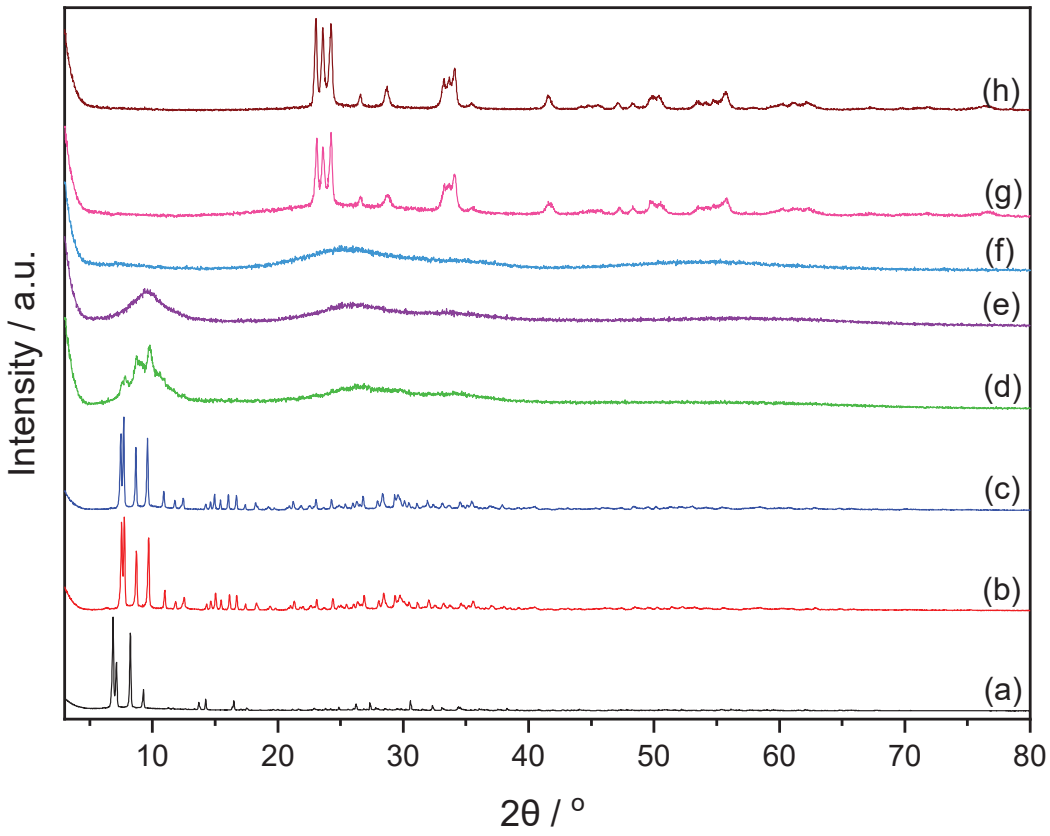

Figure 4.16. XRD patterns of solid E (wet) (a) heated at 100 (b), 150 (c), 200 (d), 250 (e), 300 (f), 350 (g), and 600 °C (h).

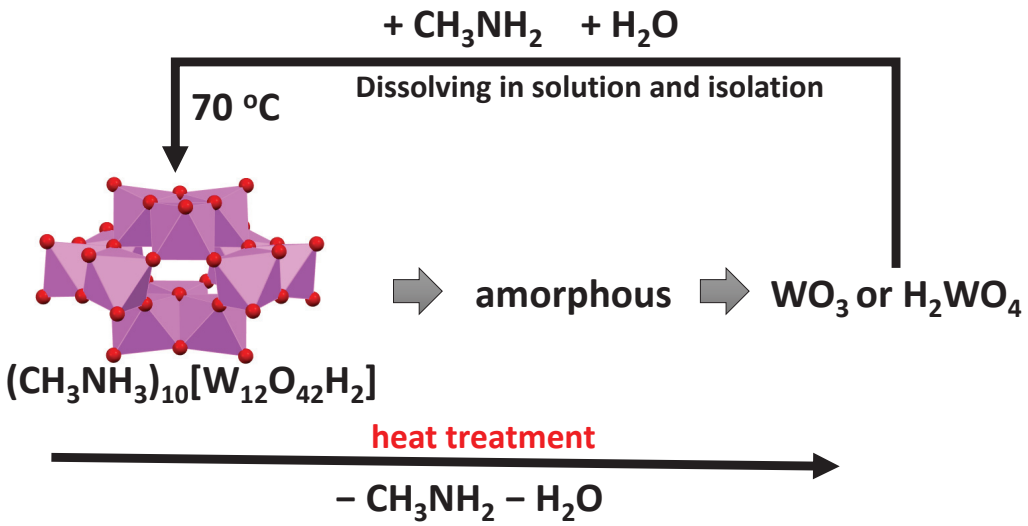

Scheme 4.3. Reaction of WO_3 and H_2WO_4 with methylamine and subsequent heating.

4.4 Conclusions

Methylammonium paradodecatungstate, $(CH_3NH_3)_{10}[H_2W_{12}O_{42}]\cdot 12H_2O$, has been synthesized and its structural characterization as well as heat-induced crystal transformation have been described. Methylammonium paradodecatungstate was produced via the reaction of WO_3 or H_2WO_4 with methylamine and subsequent drying. It was characterized in both the solid state by single-crystal and powder XRD, FT-IR, and Raman spectroscopy and solution by UV-Vis spectrometry and ^{183} W NMR measurements. The release of crystal water during the solid's drying process at 70 °C caused a reduction in the unit cell volume, however, the lattice water could be restored by the application of a small amount of water. The methylammonium paradodecatungstate was stable up to 150 °C, and further heating produced an amorphous phase and then WO_3 by further heating in air. These results indicate that the white solid produced by Ekeley upon heating at 105 °C, one of the most used negative staining reagents, might not be methylammonium heptatungstate but, instead, methylammonium paradodecatungstate.

References

[1] A. K. Jassal, R. K. Mudsainiyan, R. Shankar, *Mater. Chem. Front.* **2021**, *5*, 1090–1125.

[2] L. Cronin (Ed.), *Chem. Soc. Rev.* **2012**, *41*, 7325–7648.

[3] C. L. Hill (Ed.), *Chem. Rev.* **1998**, *98*, 1–390.

[4] M. T. Pope, *Heteropoly and Isopoly Oxometalates*, Springer-Verlag, Berlin, **1983**.

[5] H. N. Miras, L. Vilà-Nadal, L. Cronin, *Chem. Soc. Rev.* **2014**, *43*, 5679–5699.

[6] M. Tzaphlidou, J. A. Chapman, K. M. Meek, *Micron* **1982**, *13*, 119–131.

[7] X. Li, X. Cao, W. Wang, Y. Yang, G. Rao, *Front. Chem. China* **2006**, *1*, 389–392.

[8] H. Yan, X. Zhang, S. Zhou, X. Xie, Y. Luo, Y. Yu, *J. Alloys Compd.* **2011**, *509*, L232–L235.

[9] M. Sadakane, K. Sasaki, H. Kunioku, B. Ohtani, R. Abe, W. Ueda, *J. Mater. Chem.* **2010**, *20*, 1811–1818.

[10] L. Fan, J. Cao, C. Hu, *RSC Adv.* **2015**, *5*, 83377–83382.

[11] H. N. Miras, J. Yan, D. L. Long, L. Cronin, *Angew. Chem., Int. Ed.* **2008**, *47*, 8420–8423.

[12] D. L. Long, P. Kögerler, A. D. C. Parenty, J. Fielden, L. Cronin, *Angew. Chem., Int. Ed.* **2006**, *45*, 4798–4803.

[13] D. L. Long, H. Abbas, P. Kögerler, L. Cronin, *J. Am. Chem. Soc.* **2004**, *126*, 13880–13881.

[14] N. I. Gumerova, A. Rompel, *Chem. Soc. Rev.* **2020**, *49*, 7568–7601.

[15] J. B. Ekeley, *J. Am. Chem. Soc.* **1909**, *31*, 664–666.

[16] J. W. van Put, *Int. J. Refract. Met. Hard Mater.* **1995**, *13*, 61–76.

[17] P. Zavalij, J. Guo, M. S. Whittingham, R. A. Jacobson, V. Pecharsky, C. K. Bucher, S. J. Hwu, *J. Solid State Chem.* **1996**, *123*, 83–92.

[18] G. Lendvay, E. Majzik, L. Bereczki, A. Domján, L. Trif, I. E. Sajó, F. P. Franguelli, A. Farkas, S. Klébert, P. Bombicz, C. Németh, I. M. Szilágyi, L. Kótai, *RSC Adv.* **2021**, *11*, 3713–3724.

[19] S. M. Morajkar, B. R. Srinivasan, *Indian J. Chem., Sect. A* **2021**, *60*, 185–195.

[20] A. Fera, J. E. Farrington, J. Zimmerberg, T. S. Reese, *Microsc. Microanal.*

2012, *18*, 331–335.

[21] R. I. Glass, U. D. Parashar, *N. Engl. J. Med.* **2006**, *354*, 75–77.

[22] C. A. Scarff, M. J. G. Fuller, R. F. Thompson, M. G. Iadaza, *J. Vis. Exp.* **2018**, *132*, e57199.

[23] Bruker, *APEX3, SADAB5, SAINT*, **2016**.

[24] G. M. Sheldrick, *Acta Crystallogr., Sect. A Found. Crystallogr* **2008**, *64*, 112–122.

[25] G. M. Sheldrick, *Acta Crystallogr., Sect. C Struct. Chem.* **2015**, *71*, 3–8.

[26] C. B. Hübschle, G. M. Sheldrick, B. Dittrich, *J. Appl. Crystallogr.* **2011**, *44*, 1281–1284.

[27] M. J. G. Fait, H. J. Lunk, M. Feist, M. Schneider, J. N. Dann, T. A. Frisk, *Thermochim. Acta* **2008**, *469*, 12–22.

[28] Z. H. Xu, X. L. Wang, Y. G. Li, E. B. Wang, C. Qin, Y. L. Si, *Inorg. Chem. Commun.* **2007**, *10*, 276–278.

[29] E. V. Peresypkina, A. V. Virovets, S. A. Adonin, P. A. Abramov, A. V. Rogachev, P. L. Sinkevich, V. S. Korenev, M. N. Sokolov, *J. Struct. Chem.* **2014**, *55*, 295–298.

[30] J. Padchasri, R. Yimnirun, *J. Alloys Compd.* **2017**, *720*, 63–69.

[31] S. Ishikawa, T. Murayama, S. Ohmura, M. Sadakane, W. Ueda, *Chem. Mater.* **2013**, *25*, 2211–2219.

[32] E. Majzik, F. P. Franguelli, G. Lendvay, L. Trif, C. Németh, A. Farkas, S. Klébert, L. Bereczki, I. M. Szilágyi, L. Kótai, *Z. Anorg. Allg. Chem* **2021**, *647*, 593–598.

[33] A. O. Kalpakli, A. Arabaci, C. Kahruman, I. Yusufoglu, *Int. J. Refract. Met. Hard Mater.* **2013**, *37*, 106–116.

[34] S. Ikenoue, M. Mikuriya, O. Miyauchi, R. Nukada, A. Yagasaki, *Bull. Chem. Soc. Jpn.* **1994**, *67*, 2590–2592.

[35] D. Hunyadi, I. M. Szilágyi, A. L. Tóth, E. Drotár, T. Igricz, G. Pokol, *Inorg. Chim. Acta* **2016**, *444*, 29–35.

[36] S. Chaalia, J. C. Daran, A. Haddad, *J. Clust. Sci.* **2013**, *24*, 851–864.

[37] L. Wu, W. Yang, X. Dong, C. Yu, B. Liu, Y. Yan, H. Hu, G. Xue, *J. Coord. Chem.* **2015**, *68*, 2324–2333.

[38] L. R. Pizzio, C. V. Caceres, M. N. Blanco, *Adsorpt. Sci. Technol.* **1992**, *9*, 36–47.

[39] J. J. Hastings, O. W. Howarth, *J. Chem. Soc., Dalton Trans.* **1992**, *2*, 209–

215.

[40] R. I. Maksimovskaya, K. G. Burtseva, *Polyhedron* **1985**, *4*, 1559–1562.

[41] L. Trif, F. P. Franguelli, G. Lendvay, E. Majzik, K. Béres, L. Bereczki, I. M. Szilágyi, R. P. Pawar, L. Kótai, *J. Therm. Anal. Calorim.* **2021**, *144*, 81–90.

[42] J. Madarász, I. M. Szilágyi, F. Hange, G. Pokol, *J. Anal. Appl. Pyrolysis* **2004**, *72*, 197–201.

CHAPTER 5

Application of Methylammonium Polyoxometalates as a Negative Staining Reagent for Transmission Electron Microscopy Observation of Viruses

5.1 Introduction

Viruses are the tiniest of all microbes, they differ from other living things because they can only survive and reproduce inside the cells of other living things. Members of viral families differ most obviously from one another in terms of their morphology, which is highly varied. Viral morphology is the basis of viral identification, which is important in virology. The study of virology is severely constrained by the small size of viruses. Since in most cases viruses are smaller than visible light wavelength, they cannot be viewed with conventional light microscopy. A technique that enables direct imaging of viruses at the nanometer scale is electron microscopy (EM).[1–3]

Cryo-EM is one of the advanced method for detecting protein structure at an atomic level.[4,5] The sample is prepared in vitreous ice by flash-freezing the specimen, and after that the specimen is analyzed in liquid nitrogen or helium temperatures. The main advantages of cryo-EM are the possibility to examine the protein with near-native states images and the absence of artifacts. Regardless of its benefits, the main disadvantages of Cryo-EM are the low signal of the particle images, the necessity for expensive equipment, and requires sufficient training.[5,6] Cryo-specimens are only used once, which limits the possibility for discovering unexpected results.[7]

The most common EM method for viral identification is negative staining, which is a valuable technique for viewing the detailed morphology and size of the intact virus. The contrast between viruses and the background in EM images results from differences in the electron density of the structures being observed.[8] In negative staining, a solution containing heavy metals is dropped onto the samples and staining material concentrates around the virus and inside of components of the viral capsid or envelope. Viral structures that have accumulated stain may appear as various shades of black, while areas lacking stain show white against coated staining reagent (Figure 5.1). Observations will not be clear if the staining reagent is not used, because enough contrast between virions and carbon film is difficult to obtain. This is because the fragments of the virions that spread on the carbon film support are smaller than the thickness of the carbon film. Negative staining allows for the specific identification of viruses by allowing for the clear distinction of the viral particle from the background and the provision of precise morphological information such as the size and shape of viruses, but it obscures surface regularities and conceals internal structures.[9,10]

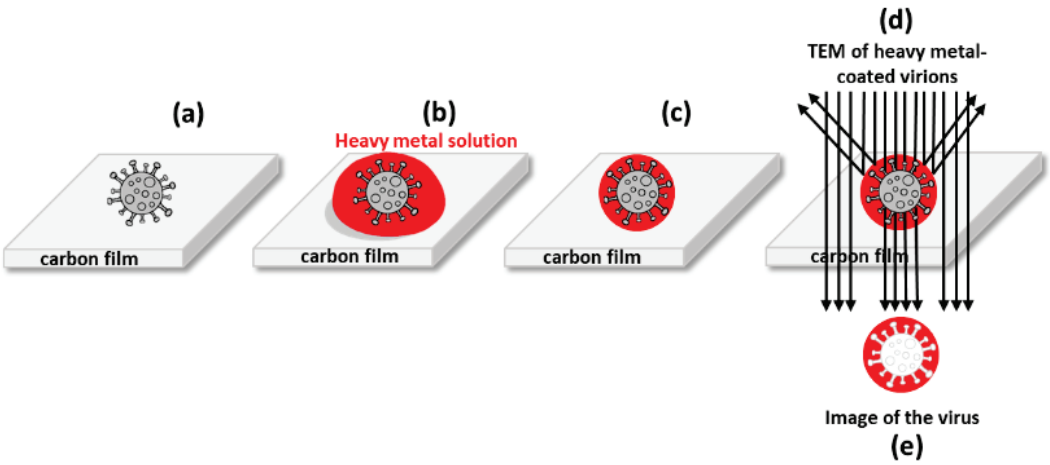

Figure 5.1. Method of negative staining. (a) Attachment virion to the carbon support film, (b) dropping heavy metal solution on the carbon film, (c) removal of excess heavy metal solution, (d) Transmission electron microscopy of heavy metal-coated virions, and (e) image of the virus in reverse contrast.

One of the most used negative staining agents is uranyl acetate and uranyl formate, these stains provide high-resolution images. Despite their effectiveness, the uranyl salts are both toxic and radioactive, which is require special storage, handling, dan disposal requirements. Because of these logistical difficulties, some researchers look for non-radioactive substitutes.[11] The main disadvantage of these stains for high magnification is the granular/microcrystalline nature of the dried stain and sensitivity to the electron beam. Due to these deficiencies, substitutes for uranyl acetate must be developed. Polyoxometalates are alternative staining reagent that has been used in observing viruses.[10–13] In this chapter, we evaluate the performance of synthesized methylammonium molybdate, tungstate, and vanadate as staining reagents for transmission electron microscopy (TEM) observation of viruses.

5.2 Experimental section

Preparation of SARS-CoV-2: VeroE6/TMPRSS2 cells [African green monkey kidney-derived cells expressing human TMPRSS2, purchased from Japanese Collection of Research Bioresources (JCRB) Cell Bank, JCRB1819] were propagated in Dulbecco's modified Eagle's minimum essential medium (DMEM; Invitrogen) supplemented with 10% fetal calf serum (FCS; Biosera, Kansas City, MO, U.S.A.), penicillin G (100 units/mL; Meiji Seika Pharma, Tokyo, Japan), and streptomycin (100 μg/mL; Meiji Seika Pharma). The cells were cultured at 37 °C in 5% CO_2. VeroE6/TMPRSS2 cells were infected with SARS-CoV-2/JP/HiroC77/2021 (Delta B.1.617.2, EPI_ISL_6316561) and hCoV-19/Japan/PG-178634/2022 (Omicron BA.1, EPI_ISL_9217693) at an input multiplicity of infection of 0.01. The infected cell culture medium was collected at 48 h post-infection, clarified using low-speed centrifugation, and filtered through a 0.45-μm filter. SARS-CoV-2 was further concentrated via ultracentrifugation at 22,000 rpm for 90 min using a 20%(w/w) sucrose/PBS cushion on a Beckman SW32 Ti rotor. The virus pellet was resuspended in 0.9% (w/v) NaCl for transmission electron

microscopy (TEM) observation. Virus culture was performed at the P3 facility of Hiroshima University under Biosafety Level 3 regulations.

TEM observations: For transmission electron microscopy (TEM) analysis, the virus solution (3 μL) was adsorbed onto a glow-discharged (PIB-10, VACUUM DEVICE PIB-10, Ibaraki, Japan) formvar and carbon-coated Cu grid (EM Japan, Tokyo, Japan) for 30 s. The excess solution was eliminated using filter paper. Subsequently, a drop (3 μL) of 0.9%(w/v) NaCl was placed in contact with the grid for 30 s for washing, and then, it was blotted with filter paper. Finally, the staining solution (0.5 wt.% in water) was placed on the grid for 30 s, and the excess solution was removed using filter paper. The staining step was performed twice, and the grid was air dried and irradiated with UV light (Care222^{TM}, Ushio Inc., Tokyo, Japan) to completely inactivate the virus.[14] This grid preparation was performed at the P3 facility of Hiroshima University under Biosafety Level 3 regulations. The sample grids were observed using TEM (JEOL, JEM-1400) with a tungsten filament operated at 80 kV at the Natural Science Center for Basic Research and Development, Hiroshima University. The images were recorded on a CCD camera (1024 × 1024 pixels).

5.3 Result and discussion

Methylammonium tungstate and vanadate have been commercialized as a staining reagent for TEM-based virus observation.[12,15] We applied our prepared methylammonium molybdate, tungstate, and vanadate to observe the SARS-CoV-2. It has been reported that image clarity was affected by the concentration of the negative staining solution.[10] The concentration effect of methylammonium heptamolybdate (0.5 and 2 wt.%) was investigated as a staining reagent. The TEM images reveal that both concentrations of methylammonium heptamolybdate are suitable staining reagents for observing coronaviruses. Characteristic crown-shaped viral surface spike protein was observed. When the concentration of methylammonium heptamolybdate was high (2 wt.%), the surface spike was unclear, some spikes were not observed on the surface (red arrow at Figure 5.2(b)).

At 0.5 wt.% concentranion (Figure 5.2(a)), crown-shaped viral surface spike proteins were clearly observable along the surface. Therefore, we selected 0.5 wt.% concentration of methylammonium polyoxometalates as a staining reagent for virus observation.

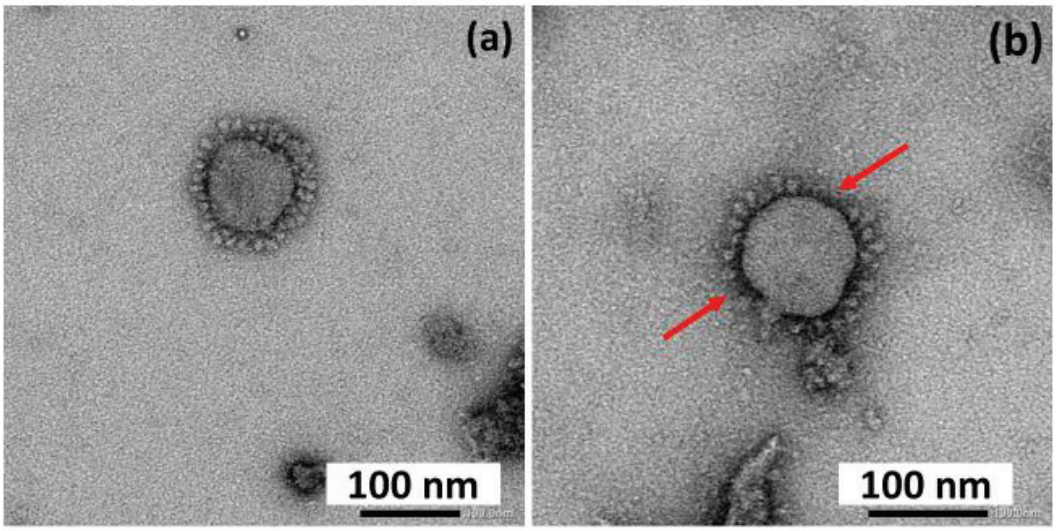

Figure 5.2. Transmission electron microscopy (TEM) images with different concentrations of methylammonium heptamolybdate. (a) 0.5 wt.% and (b) 2 wt.%.

The structure of polyoxometalates was confirmed by Raman spectroscopy. The Raman spectrum of the staining solution of methylammonium monomolybdate (0.5 wt.%) shows a strong Raman band at 898 cm^{-1}, which can be attributed to the symmetric stretching of $[MoO_4]^{2-}$(Figure 5.3(a)). This result indicates that monomolybdate, $[MoO_4]^{2-}$ is the predominant species in the 0.5 wt.% $(CH_3NH_3)_2[MoO_4]$. The Raman spectrum of the staining solution of methylammonium heptamolybdate-monomolybdate (0.5 wt.%) shows a strong Raman band at 898 and 936 cm^{-1}, which can be attributed to the symmetric stretching of $[MoO_4]^{2-}$ and asymmetric stretching of Mo=O bond in $[Mo_7O_{24}]^{6-}$, respectively (Figure 5.3(b)). This result indicates that heptamolybdate, $[Mo_7O_{24}]^{6-}$ and monomolybdate, $[MoO_4]^{2-}$ are the predominant species in the 0.5 wt.% $(CH_3NH_3)_8[Mo_7O_{24}\text{-}MoO_4]$. The Raman spectrum of the staining solution of

methylammonium heptamolybdate (0.5 wt.%) shows a strong Raman band at 936 cm^{-1}, which can be attributed to the asymmetric stretching of Mo=O bond in $[Mo_7O_{24}]^{6-}$ (Figure 5.3(c)). This result indicates that heptamolybdate, $[Mo_7O_{24}]^{6-}$ is the predominant species in the 0.5 wt.% $(CH_3NH_3)_6[Mo_7O_{24}]$.

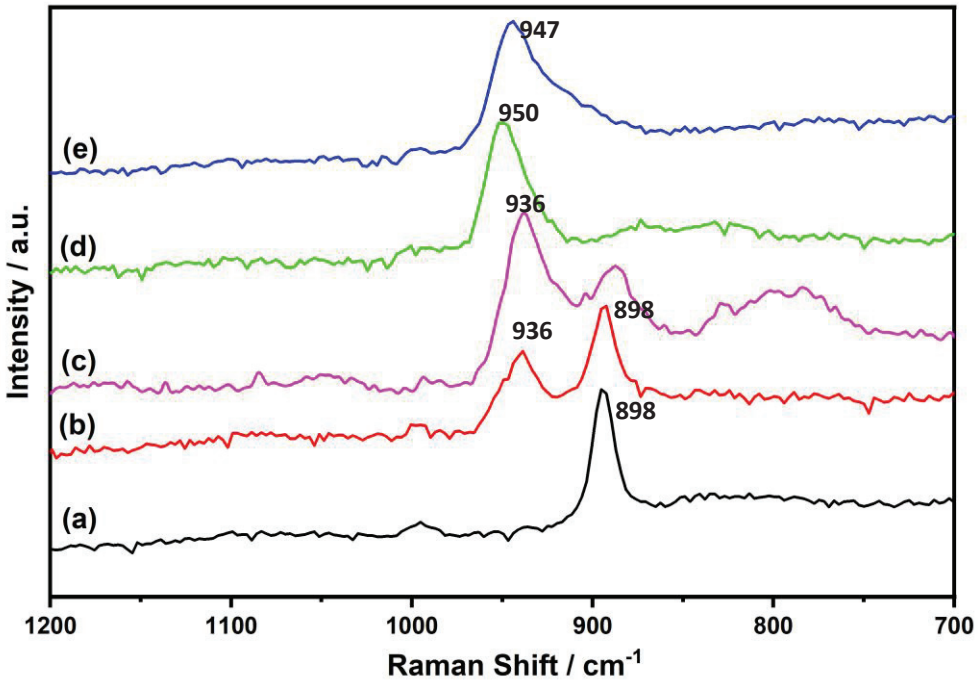

Figure 5.3. Raman spectra obtained for staining solution from (a) methylammonium monomolybdate, (b) methylammonium heptamolybdate-monomolybdate, (c) methylammonium heptamolybdate, (d) methylammonium paradodecatungstate, and (e) methylammonium vanadate. Solution concentration: 0.05 wt.%.

The Raman spectrum of the staining solution of methylammonium tungstate (0.5 wt.%) shows a strong Raman band at 950 cm^{-1}, which can be attributed to the symmetric stretching of W=O bond in $[H_2W_{12}O_{42}]^{10-}$ (Figure 5.3(d)). This result indicates that paradodecatungstate, $[H_2W_{12}O_{42}]^{10-}$ is the predominant species in the 0.5 wt.% $(CH_3NH_3)_{10}[H_2W_{12}O_{42}]$. The Raman spectrum of the staining solution of methylammonium vanadate (0.5 wt.%) shows a strong Raman band at 947 cm^{-1},

which can be attributed to the symmetric stretching of di-oxo $V(=O)_2$ unit (Figure 5.3(e)). However, it was not easy to identify the present species in the solution. Since ^{51}V NMR is a powerful tool for studying the structure of vanadate, we confirmed the structure of methylammonium vanadate in solution by this tool. The ^{51}V NMR spectrum of the 0.5 wt.% $(CH_3NH_3)[VO_3]$ shows that tetravanadate $[V_4O_{12}]^{4-}$ is the predominant species together with other V species (Figure 5.4).

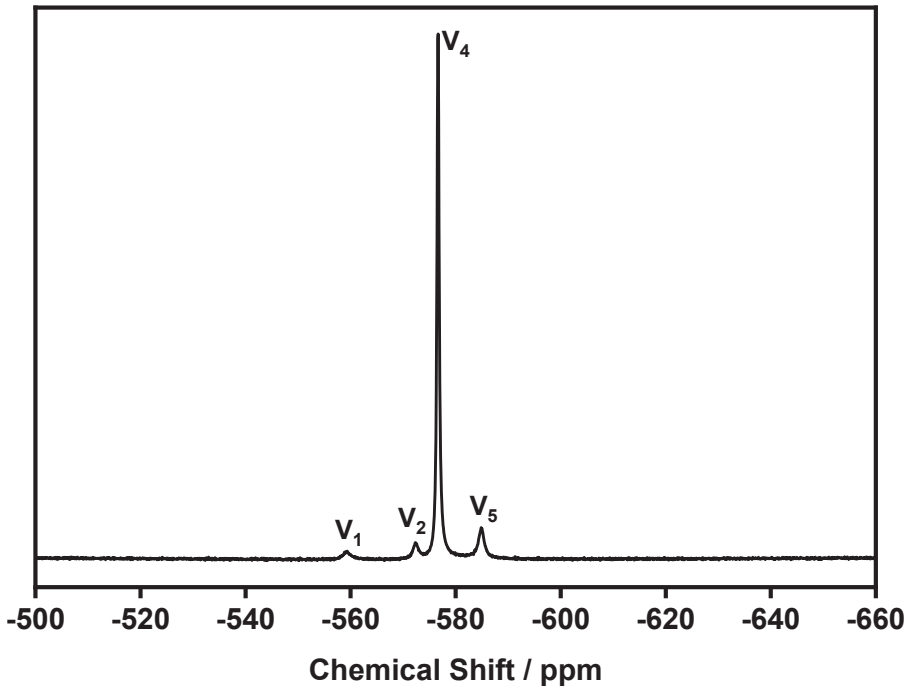

Figure 5.4. ^{51}V NMR spectrum of methylammonium vanadate in H_2O at concentration 38 mM (0.5 wt.%).

Methylammonium polyoxometalates were prepared as the staining solution at a concentration of 0.5 wt.% in water. Notably, methylammonium decamolybdate, $(CH_3NH_3)_8[Mo_{10}O_{34}]$, and methylammonium octamolybdate, $(CH_3NH_3)_4[Mo_8O_{26}]$ could not be dissolved at 0.5 wt.% in water at room temperature. In order to prepare the carbon film for TEM observation, staining solutions were placed in the area where the viruses had been adsorbed. The excess staining solution was removed using filter paper (Figure 5.1). The TEM images reveal that methylammonium

monomolybdate, heptamolybdate-monomolybdate, heptamolybdate, vanadate, and tungstate are suitable staining reagents for observing surface spike proteins and the resulted images consistent with those that had previously been reported for coronaviruses.[16] Based on the contrast and sharpness of the stained particles, methylammonium heptamolybdate was found to be an excellent staining agent for observing the SARS-CoV-2 delta variant. Virus particles were observed to have diameters of about 85-100 nm and spike lengths of 15-20 nm, which were comparable with previously reported values.[16] The polyoxometalate species on the staining solutions might interact with proteins of the virus and carbon films. The concentration of metal was increased by drying the staining solution thus resulting in more condensed species. Polyoxometalate solids coated around viruses under vacuum condition in TEM experiment, which might be a reason why virus images obtained using $(CH_3NH_3)_2[MoO_4]$ and $(CH_3NH_3)_{10}[Mo_7O_{24}\text{-}MoO_4]$ have less spikes.

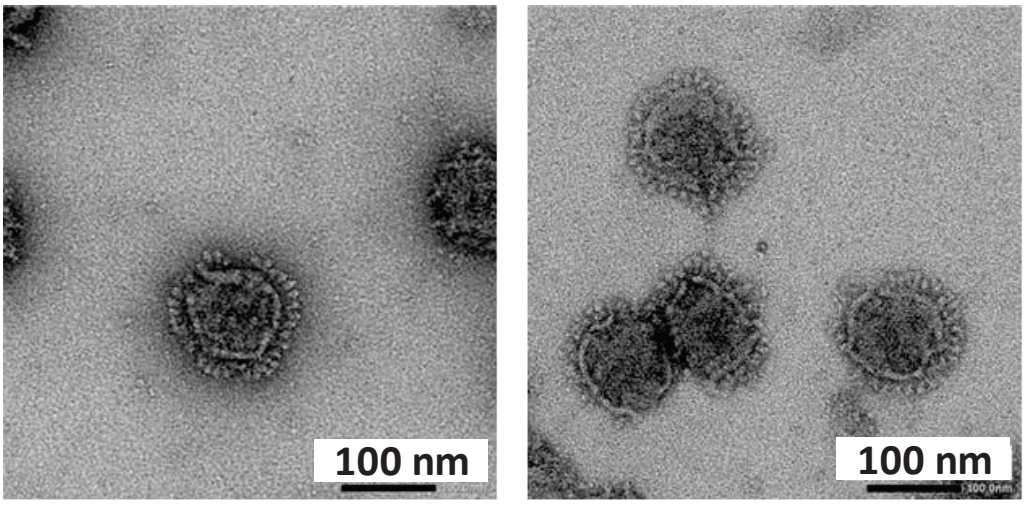

Figure 5.5 SARS-CoV-2 virions stained with 0.5 wt. % solution of methylammonium vanadate.

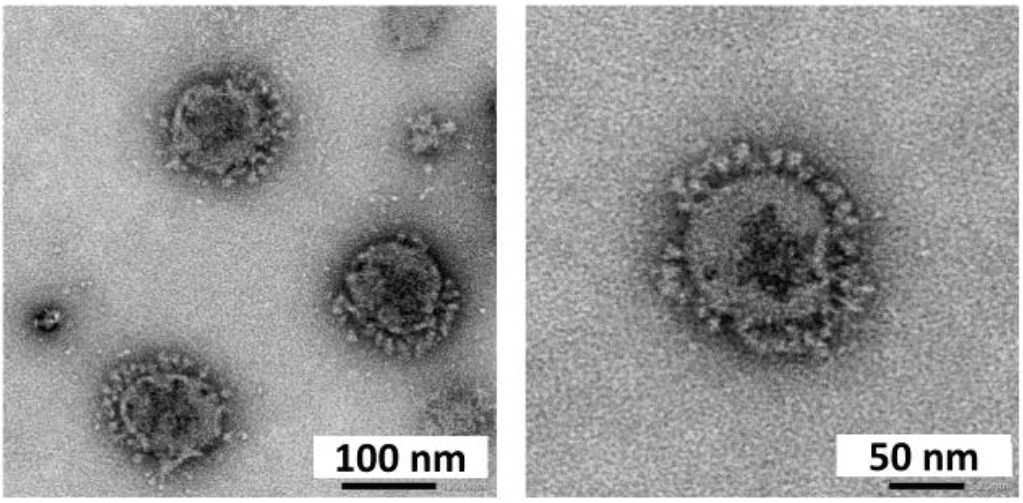

Figure 5.6. SARS-CoV-2 virions stained with 0.5 wt. % solution of methylammonium paradodecatungstate.

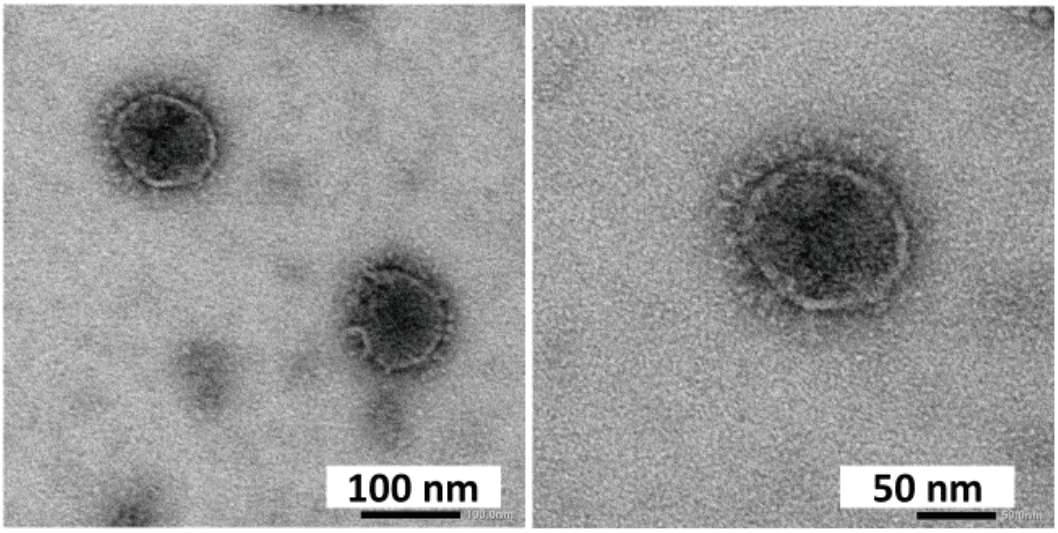

Figure 5.7. SARS-CoV-2 virions stained with 0.5 wt. % solution of methylammonium monomolybdate.

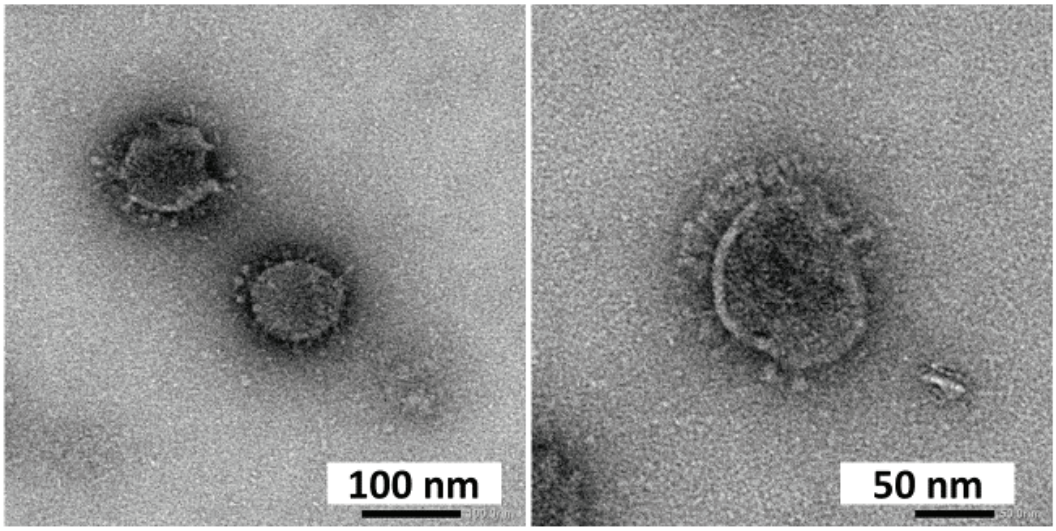

Figure 5.9. SARS-CoV-2 virions stained with 0.5 wt. % solution of methylammonium heptamolybdate-monomolybdate.

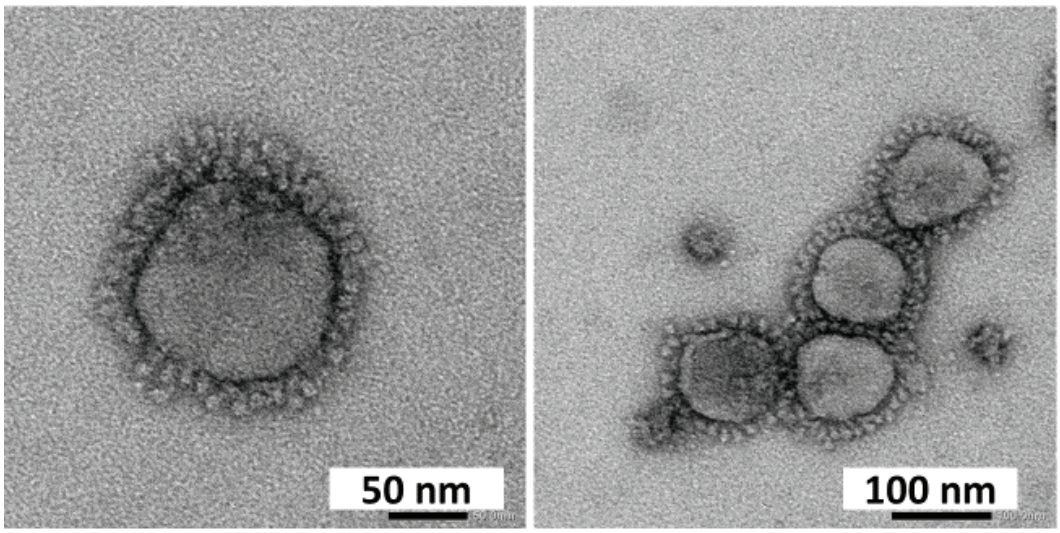

Figure 5.10. SARS-CoV-2 virions stained with 0.5 wt. % solution of methylammonium heptamolybdate.

5.4 Conclusions

We evaluated the staining ability of methylammonium monomolybdate, heptamolybdate-monomolybdate, heptamolybdate, paradodecatungstate, and

vanadate. Our results indicate that methylammonium polyoxometalates are promising negative staining reagent fo for observing SARS-CoV-2. The contrast and sharpness of the stained particles were clearly observed by staining with methylammonium heptamolybdate.

References

[1] P. Roingeard, P.-I. Raynal, S. Eymieux, *Rev. Med. Virol.* **2019**, *29*, e2019.

[2] R. Fernandez-leiro, S. H. W. Scheres, *Nature* **2016**, *537*, 339–346.

[3] D. Vanhecke, S. Asano, Z. Kochovski, *J. Microsc.* **2011**, *242*, 221–227.

[4] H. Liu, L. Jin, S. B. S. Koh, I. Atanasov, S. Schein, L. Wu, Z. H. Zhou, *Science,* **2010**, *329*, 1038–1044.

[5] J. Dubochet, *Angew. Chem. Int. Ed* **2018**, *57*, 10842–10846.

[6] B. Sander, M. M. Golas, *Microsc. Res. Tech.* **2011**, *74*, 642–663.

[7] A. Bremer, C. Henn, A. Engel, W. Baumeister, U. Aebi, *Ultramicroscopy* **1992**, *46*, 85–111.

[8] W. Baschong, U. Aebi, *Negative Staining. Cell Biology: A Laboratory Handbook, 3rd Ed, Vol. 3*, Academic Press, Cambridge, Massachusetts, **2006**.

[9] S. Brenner, R. W. Horne, *Biochim. Biophys. Acta* **1959**, *34*, 103–110.

[10] K. Sahiro, Y. Kawato, K. Koike, T. Sano, T. Nakai, *Sci. Rep.* **2022**, *12*, 7554.

[11] C. A. Scarff, M. J. G. Fuller, R. F. Thompson, M. G. Iadaza, *J. Vis. Exp.* **2018**, *132*, e57199.

[12] B. Franzetti, G. Schoehn, J.-F. Hernandez, M. Jaquinod, R. W. H. Ruigrok, G. Zaccai, *EMBO J.* **2002**, *21*, 2132–2138.

[13] N. C. Sukmana, J. Shinogi, A. Yamamoto, A. Higashiura, T. Sakaguchi, M. Sadakane, *Eur. J. Inorg. Chem.* **2022**, e202200322.

[14] H. Kitagawa, T. Nomura, T. Nazmul, K. Omori, N. Shigemoto, T. Sakaguchi, H. Ohge, *Am. J. Infect. Control* **2021**, *49*, 299–301.

[15] D. M. Shayakhmetov, T. Papayannopoulou, G. Stamatoyannopoulos, A. Lieber, *J. Virol.* **2000**, *74*, 2567–2583.

[16] H. Yao, Y. Song, Y. Chen, N. Wu, J. Xu, C. Sun, J. Zhang, T. Weng, Z. Zhang, Z. Wu, L. Cheng, D. Shi, X. Lu, J. Lei, M. Crispin, Y. Shi, L. Li, S. Li, *Cell* **2020**, *183*, 730–738.

CHAPTER 6

SUMMARY

6.1 Summary

This dissertation is dedicated to the development of alkylammonium isopolyoxometalates and their crystal transformation by heat treatment. I successfully reported methylammonium monomolybdate, methylammonium vanadate, and methylammonium paradodecatungstate which formed via the reaction of methylamine solution with MoO_3, V_2O_5, and WO_3 or H_2WO_4, respectively. We were so lucky that we could obtain monomolybdate compound by adding DMF into the reaction mixture of MoO_3 and methylamine solution. We try to isolate methylammonium vanadate and methylammonium tungstate by adding several organic solvents into reaction mixtures and it failed. Methylammonium vanadate $(CH_3NH_3)[VO_3]$ and methylammonium paradodecatungstate, $(CH_3NH_3)_{10}[H_2W_{12}O_{42}]$ solids were obtained by drying the reaction mixture at 70 °C under atmospheric pressure.

By heating methylammonium isopolyoxometalates, the volatile CH_3NH_2 and water formed from $CH_3NH_3^+$ and oxygen atoms in metalates are diminished. Based on the result of TPD-MS, the first decomposition temperatures of water and/or methylammonium were different (methylammonium paradodecatungstate: 50 °C, methylammonium vanadate: 120 °C, and methylammonium monomolybdate: 100 °C). This may be due to the difference in the strength of the hydrogen bonding formed in each crystal, which causes the energy required to break the hydrogen bonding to be different. The powder XRD patterns of methylammonium isopolyoxometalates were changed by heating in air, indicating that solid-state condensation was encouraged. The formation of several isopolyoxometalates during heat treatment might be caused by condensation reaction as the effect of releasing CH_3NH_2 and H_2O which has a similar effect to acidification. Further heating, they are fully transformed into metal oxide (MoO_3, V_2O_5, and WO_3) (Figure

6.1). We also evaluated the staining ability of obtained methylammonium monomolybdate, heptamolybdate-monomolybdate, heptamolybdate, paradodecatungstate, and vanadate because they fulfill the conditions that are thought to make ideal virus staining agents, notably neutral, stable, and water-soluble since viruses are frequently observed in neutral conditions.

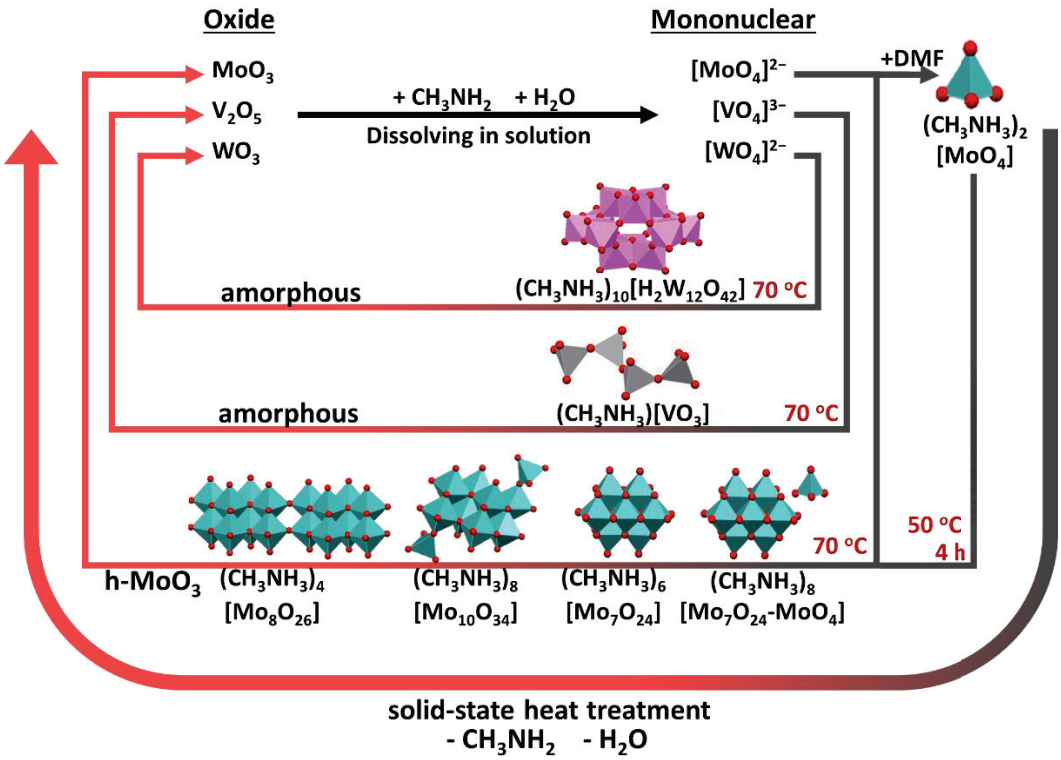

Figure 6.1. Formation of methylammonium isopolyoxometalates via reaction of metal oxides (MoO_3, V_2O_5, and WO_3), H_2O, and CH_3NH_2, and their solid-state thermal transformation.

The main conclusions in this thesis were summarized according to each chapter as follows:

[1]. Methylammonium monomolybdate, $(CH_3NH_3)_2[MoO_4]$, was synthesized by dissolving MoO_3 in an aqueous methylamine solution with a CH_3NH_2/Mo ratio of 4 and then adding N,N-dimethylformamide. The compound was made up of two methylammonium counter-cations and one monomeric $[MoO_4]^{2-}$. It crystallized in the *Pnma* space group. Solid-state heating of $(CH_3NH_3)_2[MoO_4]$

in air released water and methylammonium, which led to the formation of several methylammonium isopolymolybdates, such as $(CH_3NH_3)_8[Mo_7O_{24}\text{-}MoO_4]$, $(CH_3NH_3)_6[Mo_7O_{24}]$, $(CH_3NH_3)_8[Mo_{10}O_{34}]$, and $(CH_3NH_3)_4[Mo_8O_{26}]$, and molybdenum oxides such as hexagonal MoO_3 and orthorhombic MoO_3 (Figure 6.2) which were confirmed by single crystal XRD, powder XRD, IR, Raman, and elemental analysis. Some of the structures of formed polyoxomolybdates were different from those of the molybdates made from ammonium.

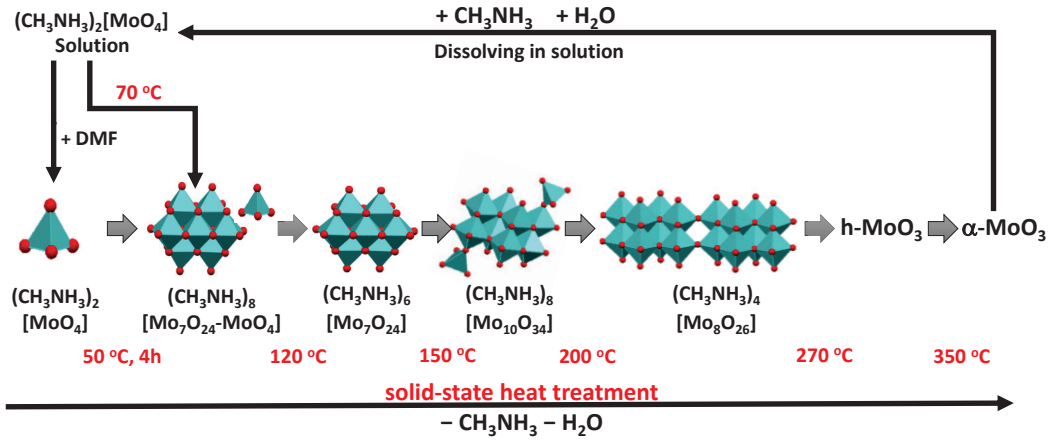

Figure 6.2. Formation of methylammonium monomolybdate via reaction of MoO_3, H_2O, and CH_3NH_2, and its solid-state thermal transformation.

[2]. Methylammonium vanadate, $(CH_3NH_3)[VO_3]$, was prepared by dissolving V_2O_5 in methylamine solution (40%) with a methylamine/vanadium ratio of 2.8 at room temperature and subsequent drying at 70 °C. The compound was made up of methylammonium counter-cations and "snake-like" $([VO_3]^-)_n$ anion chains propagating along the *c*-direction in the *Pna*2$_1$ space group. The solid-state reversible thermal structural transformation of methylammonium vanadate, $(CH_3NH_3)[VO_3]$, at ca. –110 °C has been observed (Figure 6.3). Single-crystal X-ray structural analysis at different temperatures indicated that the structural transformation was due to a change in the direction of the

methylammonium cation. However, heating causes decomposition to form V_2O_5.

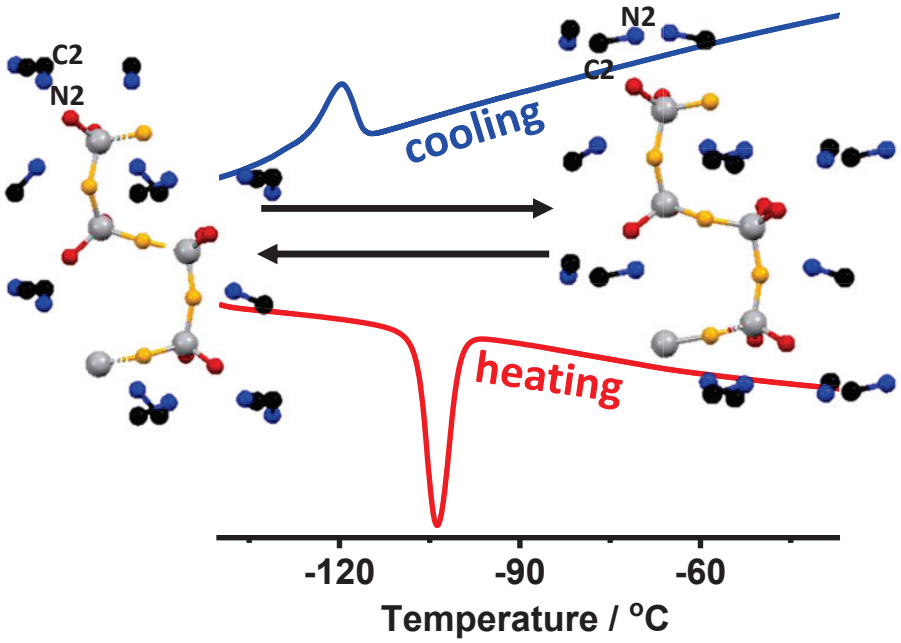

Figure 6.3. Reversible structural transformation due to the re-orientation of the methylammonium cations.

[3]. Methylammonium paradodecatungstate, $(CH_3NH_3)_{10}[H_2W_{12}O_{42}]\cdot 12H_2O$, has been synthesized and its structural characterization as well as heat-induced crystal transformation have been described. Methylammonium paradodecatungstate was produced via the reaction of WO_3 or H_2WO_4 with methylamine and subsequent drying. It was characterized in both the solid state by single-crystal and powder XRD, FT-IR, and Raman spectroscopy and solution by UV-Vis spectrometry and ^{183}W NMR measurements. The release of crystal water during the solid's drying process at 70 °C caused a reduction in the unit cell volume, however, the lattice water could be restored by the application of a small amount of water (Figure 6.4). The methylammonium paradodecatungstate was stable up to 150 °C, and further heating produced an amorphous phase and then WO_3 by further heating in air. These results indicate that the white solid produced by Ekeley upon heating at 105 °C, one of the

most used negative staining reagents, might not be methylammonium heptatungstate but, instead, methylammonium paradodecatungstate.

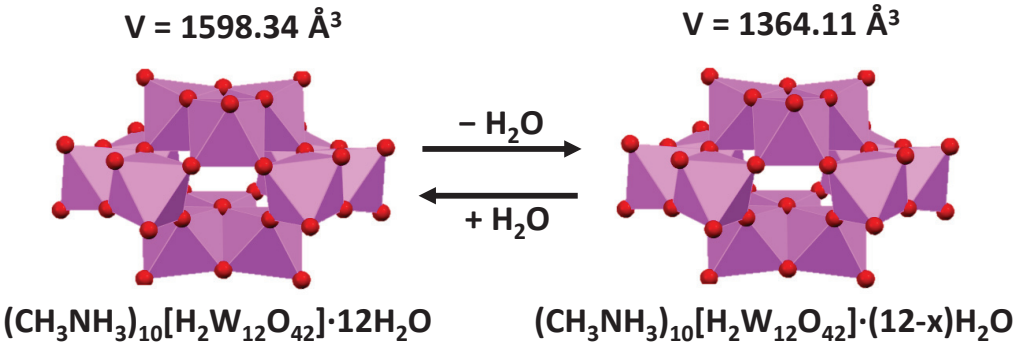

Figure 6.4. Reversible volume reduction of methylammonium paradodecatungstate on drying at 70 °C and adding water.

[4]. We evaluated the staining ability of methylammonium monomolybdate, heptamolybdate-monomolybdate, heptamolybdate, paradodecatungstate, and vanadate. Our results indicate that methylammonium polyoxometalates are promising negative staining reagent fo for observing SARS-CoV-2. The contrast and sharpness of the stained particles were clearly observed by staining with methylammonium heptamolybdate.

6.2 Recommendations

Based on the results and the conclusions of this dissertation, there are several parts that need to investigate in future works such as :

[1]. Synthesis and structural characterization of methylammonium polyoxoniobate. It has been reported that polyoxoniobates have distinctive electrical structures, tunable energy bands, and great stability, which can be candidates for environmentally friendly catalysts.

[2]. Staining abilities of synthesized methylammonium polyoxometalates as a negative staining reagent for transmission electron microscopy observation of viruses other than SARS-CoV-2, because viral morphology is the basis of viral identification. The primary distinction between members of viral families is

their morphology, so viral morphology is crucial to the study of virology. Studying the structure of viral protein targets can inform the design of novel antivirals.

[3]. Application of synthesized methylammonium polyoxometalates for transferable building blocks that can be used for the development of new material such as orthorhombic MoV oxide. Consecutive and parallel oxidation reactions require the use of highly selective catalysts with designed properties in order to control the reaction without resulting in complete oxidation. MoV oxides are potential catalysts for the selective oxidation of light alkanes, which have high thermal stability and exhibit attractive productivity, activity, and selectivity.

List of Publications

Peer-reviewed journal articles:

1. **Ndaru Candra Sukmana**, Sugiarto, Zhenxin Zhang, Masahiro Sadakane*, Structure and Thermal Transformations of Methylammonium Tungstate. *Z. Anorg. Allg. Chem.* 2021, *647*, 1930–1937.
2. **Ndaru Candra Sukmana**, Sugiarto, Jun Shinogi, Akima Yamamoto, Akifumi Higashiura, Takemasa Sakaguchi, and Masahiro Sadakane*, Thermal Structure Transformation of Methylammonium Vanadate and it's Application as a Negative Staining Reagent for Observing SARS-CoV-2. *Eur. J. Inorg. Chem.* 2022, e202200322.
3. **Ndaru Candra Sukmana ,** Sugiarto, Jun Shinogi, Tatsuhiro Kojima, Akifumi Higashiura, Akima Yamamoto, Takemasa Sakaguchi, Masahiro Sadakane*, Solid-State Thermal Transformation of Methylammonium Monomolybdate to Methylammonium Polyoxomolybbdates and their Applications as Staining Reagents for Transmission Electron Microscopy Observations of Viruses, *Chem. Lett*. 2023, Accepted.

Conferences:

1. **Ndaru Candra Sukmana**, Tatsuhiro Kojima, Masaru Fujibayashi, Sadafumi Nishihara, Masahiro Sadakane, Synthesis of Methylammonium Hepta-Monomolybdate and Its Transformation by Heat-Treatment, The 101st Annual

Meeting-The Chemical Society of Japan, March 19-22, 2021, online meeting (poster presentation).

2. **Ndaru Candra Sukmana**, Tatsuhiro Kojima, Masaru Fujibayashi, Sadafumi Nishihara, Masahiro Sadakane, Structure and Thermal Transformations of Methylammonium Molybdate, International Network on Polyoxometalate Science for Advanced Functional Energy Materials Conference, July 19-22, 2021, online meeting (poster presentation).
3. **Ndaru Candra Sukmana**, Tatsuhiro Kojima, Masaru Fujibayashi, Sadafumi Nishihara, Sugiarto, Zhenxin Zhang, Masahiro Sadakane, Structure and Thermal Transformations of Methylammonium Molybdate and Tungstate, The 71st Japan Society of Coordination Chemistry, September 16-19, 2021, online meeting (oral presentation).
4. **Ndaru Candra Sukmana**, Sugiarto, Masahiro Sadakane, Structure and Thermal Transformations of Methylammonium Molybdate and Vanadate, The 72nd Conference of Japan Society of Coordination Chemistry, September 26-28, 2022, Kyushu University, Ito Campus (oral presentation).
5. **Ndaru Candra Sukmana**, Sugiarto, Masaru Fujibayashi, Sadafumi Nishihara, Nao Tsunoji, Takuo Minato, Masahiro Sadakane, Stepwise Condensation of Methylammonium Isopolymolybdates, Chemical Society of Japan Chugoku-Shikoku Chapter Conference, November 12-13, 2022, Hiroshima University, Higashihiroshima Campus (oral presentation).

Acknowledgments

I would like to express my sincere gratitude to my advisor Professor Masahiro Sadakane for his continue patient guidance, inspiration, great support, and enthusiastic encouragement during my research and preparation doctoral dissertation. I learned a lot from his profound knowledge and perseverance in research which will provide me with lifetime benefits for my future career.

I am grateful to Prof. Nao Tsunoji and Prof. Takuo Minato for their kind assistance in my experiment and insightful discussion of my research work. I would like to thank my college in Catalytic Materials Chemistry Laboratory and the staff of Applied Chemistry Department for their sustained help and friendship. I also would like to appreciate the help from Mr. Jun Shinogi and Dr. Sugiarto who supports my research work.

I would like to thank Prof. Zhenxin Zhang in School of Materials Science and Chemical Engineering, Ningbo University, Dr. Akima Yamamoto, Dr. Akifumi Higashihiura, and Prof. Takemasa Sakaguchi in Departement of Virology, Graduate School of Biomedical and Health Sciences, Hiroshima University, Prof. Tatsuhiro Kojima in Department of Chemistry, Graduate School of Science, Osaka University, Prof. Masaru Fujibayashi and Prof. Sadafumi Nishihara in Department of Chemistry, Graduate School of Advanced Science and Engineering, Hiroshima University, and Prof. Cédric Tassel in Department of Energy and Hydrocarbon Chemistry, Graduate School of Engineering, Kyoto University for collaboration work in my doctoral research.

I would like to thank Ms. Megumi Kosaka and Mr. Motonari Kobayashi in Division of Instrumental Analysis, Okayama University for the measurements of CHN elemental analyses, Ms. Kanae Koike at Natural Science Center for Basic Research and Development, Hiroshima University for support to use TEM, and Mr. Hitoshi Fujitaka at the Natural Science Center for Basic Research and Development, Hiroshima for the ^{183}W and ^{51}V NMR measurements.

I would like to thank the financial support from the Osimo Scholarship and Program for Developing and Supporting the Next Generation of Innovative

Researchers at Hiroshima University that enabled this work to be successfully completed

Lastly, I would like to thank my family member, especially my parents (Subandi and Sri Suhartini), my wife (Ufafa Anggarini), and my kids (Athala Dzaky Sukmana and Zyana Mirai Sukmana) for their endless support, understanding, and encouragement, which motivated me to insist on my study. I cannot acknowledge them enough and I love them for the sake of Allah.

Ndaru Candra Sukmana